

American University in Cairo

## AUC Knowledge Fountain

---

Theses and Dissertations

Student Research

---

Winter 1-31-2024

# The Effect of Mechanical Strain On the Electronic Conductivity of A- Fe2O3: A Density Functional Theory Study

Sheriff Naziru Abdulmutalib  
abdulmutalib@aucegypt.edu

Follow this and additional works at: <https://fount.aucegypt.edu/etds>



Part of the [Nanoscience and Nanotechnology Commons](#), [Physical Sciences and Mathematics Commons](#), and the [Semiconductor and Optical Materials Commons](#)

---

## Recommended Citation

### APA Citation

Abdulmutalib, S. (2024). *The Effect of Mechanical Strain On the Electronic Conductivity of A- Fe2O3: A Density Functional Theory Study* [Master's Thesis, the American University in Cairo]. AUC Knowledge Fountain.

<https://fount.aucegypt.edu/etds/2198>

### MLA Citation

Abdulmutalib, Sheriff Naziru. *The Effect of Mechanical Strain On the Electronic Conductivity of A- Fe2O3: A Density Functional Theory Study*. 2024. American University in Cairo, Master's Thesis. *AUC Knowledge Fountain*.

<https://fount.aucegypt.edu/etds/2198>

This Master's Thesis is brought to you for free and open access by the Student Research at AUC Knowledge Fountain. It has been accepted for inclusion in Theses and Dissertations by an authorized administrator of AUC Knowledge Fountain. For more information, please contact [thesisadmin@aucegypt.edu](mailto:thesisadmin@aucegypt.edu).



***The effect of mechanical strain on the electronic conductivity of  $\alpha$ - $Fe_2O_3$ : A density functional theory study***

A THESIS SUBMITTED BY

Sheriff Naziru Abdulmutalib

TO THE

*Nanotechnology Graduate Program*

31/08/2023

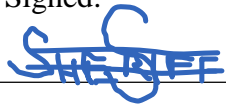
*in partial fulfillment of the requirements for the degree of  
Master of Science in Nanotechnology*

# Declaration of Authorship

I, Sheriff Naziru Abdulmutalib, declare that this thesis titled, "*The effect of mechanical strain on the electronic conductivity of  $\alpha$ -Fe<sub>2</sub>O<sub>3</sub>: A density functional theory study*" and the work presented in it are my own. I confirm that:

- This work was done wholly or mainly while in candidature for a research degree at this University.
- Where any part of this thesis has previously been submitted for a degree or any other qualification at this University or any other institution, this has been clearly stated.
- Where I have consulted the published work of others, this is always clearly attributed.
- Where I have quoted from the work of others, the source is always given. With the exception of such quotations, this thesis is entirely my own work.
- I have acknowledged all main sources of help.
- Where the thesis is based on work done by myself jointly with others, I have made clear exactly what was done by others and what I have contributed myself.

Signed:



Sheriff Naziru Abdulmutalib

---

Date:

31/08/2023

---

# Acknowledgement

I am humbled and grateful to have had the opportunity to work under the guidance of Dr. Mostafa Youssef, whose unwavering support and mentorship have been invaluable throughout this research project. Dr. Mostafa's expertise, dedication, and passion for research have inspired me to strive for excellence in all my endeavors.

I would also like to extend my gratitude to the members of my thesis committee, Dr. Ehab El Sawy and Dr. Sarah Khalil for their valuable feedback, constructive criticism, and guidance. Their insights have contributed greatly to the success of this work and will undoubtedly benefit my future career.

I would like to acknowledge the Material Theory Group for providing a stimulating and collaborative work environment, where I have had the opportunity to engage in fruitful discussions and learn from my colleagues' diverse perspectives. Special thanks are due to Hoda El Gibally for her support during the early stages of this project.

I am deeply grateful to my friends, Abdulbaqi Ubandawaki, Mohammed Mahrous and Fahad Dankabo, for their unwavering support and encouragement throughout my graduate studies. Their friendship has been a source of strength and inspiration, and I am fortunate to have them in my life.

I would like to express my appreciation to The American University in Cairo for the Graduate Research Support Grant and the African Graduate Fellowship that supported my Master's studies in the Nanotechnology Program. These funding opportunities have been instrumental in enabling me to pursue my academic goals and realize my full potential.

Finally, I am indebted to my parents for their unconditional love, support, and encouragement. Their unwavering belief in me has been a constant source of motivation, and I am grateful for all that they have done to help me achieve my dreams.

# Abstract

Hydrogen has emerged as a promising future energy carrier due to its ability to produce zero carbon dioxide ( $\text{CO}_2$ ) emissions when burned. However, the limited natural abundance of hydrogen necessitates the development of cost-effective and environmentally friendly methods for large-scale hydrogen production. Among the different hydrogen production approaches, photoelectrochemical water splitting, which employs a photoanode material in a cell using solar energy to split water into hydrogen and oxygen, is the focus of this work.  $\alpha\text{-Fe}_2\text{O}_3$  (hematite) is a photoanode material that shows a promising future for hydrogen generation in a photoelectrochemical cells due to its cheapness, availability, and its capacity to absorb light within the range of visible spectrum. Nevertheless, when compared to other photoanode its main drawback is its overall low electronic conductivity, adversely affecting its activity as a photoanode material. Meanwhile, mechanical strain is known to modulate transport processes in materials including electronic conductivity. Herein, we aim to understand the effect of biaxial strain both compressive and tensile on changing the electronic conductivity of hematite. Prior work showed that in strain-free hematite slow small polarons predominates over fast large polarons (or free carriers) but they both co-exist. We explore the effect of biaxial mechanical strain on the electronic conductivity of hematite using density functional theory calculations with on-site Hubbard U terms on oxygen p-states and iron d-states. We apply biaxial strain in increments of 0.5% from  $-5\%$  to  $+5\%$  and find that the bandgap reduction occurs under both tensile and compressive strain, with a more significant reduction observed in the compressive strain state. We also observe an increase in free electron effective mass and a decrease in free hole effective mass as we move from the tensile to the compressive strain state. Moreover, we investigate the effect of mechanical strain on polarons of hematite and find out that it cannot change the energy landscape in favor of large polaron electrons (or free electrons). However, mechanical strain can alter the energy landscape in favor of large polaron holes (or free holes). This implies that applying slight compressive strain can enhance the overall electronic conductivity in hematite via reducing the band gap, increasing the concentration and the mobility of holes especially via large hole polarons while not significantly affecting the mobility of electrons. These findings provide insights into modulating the electronic conductivity of hematite, which can promote its use as a photocatalyst for hydrogen production, addressing the increasing energy demand and mitigating the impact of climate change.

# Table of Contents

Declaration of Authorship .....	ii
Acknowledgement .....	iii
Abstract .....	iv
List of Figures .....	vii
List of Tables .....	x
List of Abbreviation .....	xi
List of Symbols .....	xii
Chapter 1 .....	1
Introduction .....	1
1.1 Motivation for the study .....	1
1.2 Aims and Objectives .....	4
1.3 Thesis Outline .....	5
Chapter 2 .....	6
Literature review .....	6
2.1 Hematite as a photoanode material .....	6
2.2 Electronic bandgap and electronic structure of hematite .....	7
2.3 Defect Chemistry of Hematite .....	8
2.4 Polarons in hematite .....	10
2.5 Polarons Mobility in Hematite .....	11
2.6 Conductivity in hematite .....	12
2.7 Can mechanical strain improve the electronic conductivity of hematite? .....	13
Chapter 3 .....	16
Computational Methods .....	16
3.1 First Principle Parameters .....	16
3.2 Density Functional Theory Calculations and Biaxial Strain .....	17
3.3 Band Effective mass .....	17
3.3 Self-trapping energy .....	19
Chapter 4 .....	21
Results and Discussion .....	21
4.1 Prefect crystal of hematite .....	21
4.2 Effective mass of free charge carriers .....	26

4.3 Polarons in hematite.....	31
4.4 Implications to photoelectrochemical water splitting .....	37
Chapter 5 .....	39
Conclusion and Future Work .....	39
5.1 Conclusion .....	39
5.2 Future Work .....	40
References .....	41
Appendix.....	49
1. Quantum Espresso Sample Input files .....	49
A. small polaron calculations .....	49
2. DFT Energies .....	53
A. Hubbard U values of $U(\text{Fe}) = 3.0 \text{ eV}$ and $U(\text{O}) = 7.0 \text{ eV}$ .....	53
B. Hubbard U values of $U(\text{Fe}) = 4.0 \text{ eV}$ and $U(\text{O}) = 6.5 \text{ eV}$ .....	54
3. Projected density of states (PDOS) plots .....	56
A. Biaxial tensile strain .....	56
B. Biaxial compressive strain.....	59
4. Band structures.....	61
A. Biaxial tensile strain .....	61
B. Biaxial compressive strain.....	63
5. Total Density of states (TDOS) .....	64
A. Hubbard U values of $U(\text{Fe}) = 3.0 \text{ eV}$ and $U(\text{O}) = 7.0 \text{ eV}$ .....	64
I. Biaxial tensile strain .....	65
II. Biaxial compressive strain.....	67
B. Hubbard U values of $U(\text{Fe}) = 4.0 \text{ eV}$ and $U(\text{O}) = 6.5 \text{ eV}$ .....	69
I. Biaxial tensile strain .....	69
II. Biaxial compressive strain.....	71

# List of Figures

Figure 1. Schematic representation of a photoelectrochemical cell showing the anode (semiconductor material) and the cathode (metal cathode) <sup>4</sup> .....	3
Figure 2. Schematic diagram of the unit cells of hematite. (a) The primitive cell of hematite has a rhombohedral crystal structure with ten atoms and lattice parameters of $a = b = c = 5.474 \text{ \AA}$ . (b) The conventional cell has a hexagonal corundum crystal structure with 30 atoms and lattice parameters of $a = b = 5.069 \text{ \AA}$ , $c = 13.805 \text{ \AA}$ . The diagram was generated using the VESTA visualization software package <sup>40</sup> .....	7
Figure 3. The Projected Density of State (PDOS) of hematite showing the contribution of Fe-3d orbital and O-2p orbital to the density of states <sup>24</sup> . ....	8
Figure 4. Visualization of Charge density isosurfaces in $\alpha\text{-Fe}_2\text{O}_3$ shown in yellow for the cases; (a) small polaron electron localizing on an Fe ion, (b) large polaron electron (free electron) delocalized on in the d-states of Fe ions at the bottom of the conduction band, and . The isosurface level for the small polarons was maintained at $0.019 \text{ e/\AA}^3$ while for the free carriers the isosurface is maintained at $0.02 \text{ e/\AA}^3$ . Gold (large) and red (small) represents Fe and O ions respectively. These images are generated using VESTA visualization software package <sup>40</sup> in this work.....	11
Figure 5. The electronic bandgap of hematite at zero strain for the rhombohedral crystal structure. (a) The Projected density of states (PDOS) of showing the contributions of O-2p orbitals and Fe-3d orbitals to the electronic bandgap of hematite. (b) The band structure along the high-symmetry points ( $\Gamma - T - H_2 H_0 - L - \Gamma - S_0 S_2 - F - \Gamma$ ). It is important to note that hematite has an indirect bandgap. ....	22
Figure 6. Effect of strain on the bandgap of hematite. The blue-filled points represent the initial study with $U(\text{Fe}) = 3.0 \text{ eV}$ and $U(\text{O}) = 7.0 \text{ eV}$ . The white-filled points represent the second study with $U(\text{Fe}) = 4.0 \text{ eV}$ and $U(\text{O}) = 6.5 \text{ eV}$ . In both cases, the reduction of bandgap occurs at both tensile and compressive strain but is more prominent in the compressive strain state.....	23
Figure 7. Effect of biaxial strain on volume. (a) represents the study using $U(\text{Fe}) = 3.0 \text{ eV}$ on Fe and $U(\text{O}) = 7.0 \text{ eV}$ on O, while (b) illustrates the study using $U(\text{Fe}) = 4.0 \text{ eV}$ and $U(\text{O}) = 6.5 \text{ eV}$ . The left vertical axis represents the volume as a function of biaxial strain, and the right vertical axis represents the plot of the volumetric strain per biaxial strain as a function of biaxial strain, which slope gives the volumetric strain per biaxial strain of 1.2.....	25



Figure 8. Effect of biaxial strain on the z-axis. (a) represents the first study using  $U(\text{Fe}) = 3.0$  eV on Fe and  $U(\text{O}) = 7.0$  eV on O, while (b) represents the second study using  $U(\text{Fe}) = 4.0$  eV and  $U(\text{O}) = 6.5$  eV. The left vertical axis represents the z-axis as a function of biaxial strain, and the right vertical axis represents the plot of the lateral strain as a function of biaxial strain, which slope gives the Poisson's ratio of 0.80..... 26

Figure 9. The high symmetry path in the reciprocal space used for the calculation of electron effective mass at the conduction band (CBM) minima and hole effective mass at the valence band maxima (VBM)..... 27

Figure 10. Effect of mechanical strain on the effective mass of charge carriers in hematite. (a) shows the effective mass of free electrons and holes using  $U(\text{Fe}) = 3.0$  eV and  $U(\text{O}) = 7.0$  eV. (b) represents the effective masses employing  $U(\text{Fe}) = 4.0$  eV and  $U(\text{O}) = 6.5$  eV. In both plots, the left vertical axis (in blue) represents the effective mass of electrons while the right vertical axis (in red) represents the hole effective masses as a function of strain. It is important to note that the effective masses are normalized to the mass of an electron,  $9.11 \times 10^{-31}$  kg..... 31

Figure 11. Visualization of Charge density isosurface shown in yellow (a) small polaron electron localizing on Fe atom, (b) small polaron hole localizing on O atoms, (c) large polaron electron (free electron) delocalized on Fe atoms, and (d) large polaron hole (free hole) delocalize on O atoms. The isosurface level for the small polarons was maintained at  $0.019 \text{ e}/\text{\AA}^3$ , while for the free carriers, the isosurface is maintained at  $0.02 \text{ e}/\text{\AA}^3$ . Gold (large) and red (small) represents Fe and O atoms, respectively. These images are generated using VESTA visualization software package 40 ..... 34

Figure 12. Small polarons energy level in the bandgap of hematite as a function of biaxial strain. It is worth noting that  $\Delta E$  in eV is the energy difference between the center of the polaron energy peak to the edge of either the valence band maximum (polaron hole) or conduction band minimum (polaron electron). (a) small polaron electron energy level in eV as a function of biaxial strain (b) small polaron hole energy level in eV as a function of biaxial strain. In both plots, the energy levels increase in the tensile strain state favoring small polaron formation in the material. .... 34

Figure 13. The predominance charge defect in hematite based on ***Eself – trapping*** as a function of the mechanical strain using (a) the ***Eself – trapping*** in eV indicating the predominant defects to be small polaron electrons for all strain conditions. The filled circles (in red) represent the case with  $U(\text{Fe})= 3.0$  eV and  $U(\text{O}) = 7.0$  eV, while the unfilled circles (white

color) represent the case of  $U(\text{Fe}) = 4.0 \text{ eV}$  and  $U(\text{O}) = 6.5 \text{ eV}$  (b) the ***Eself – trapping*** indicating the predominant defects to be free holes at strains above -3.5% compressive strain. The filled circles (green color) represent the case with  $U(\text{Fe}) = 3.0 \text{ eV}$  and  $U(\text{O}) = 7.0 \text{ eV}$ , while the unfilled circles (white color) represent the case of  $U(\text{Fe}) = 4.0 \text{ eV}$  and  $U(\text{O}) = 6.5 \text{ eV}$ ..... 37

# List of Tables

**Table 1.** Effective mass of charge carriers in pure hematite available in the literature.

---

27

# List of Abbreviation

<b>IEA</b>	International Energy Agency
<b>HCP</b>	Hexagonal closed-packed
<b>DFT</b>	Density Functional Theory
<b>DFT + U</b>	Density Functional Theory with Hubbard U value
<b>VBM</b>	Valence Band Maxima
<b>CBM</b>	Conduction Band Minima
<b>GGA</b>	Generalized Gradient Approximation
<b>PBE</b>	Perdew-Burke-Ernzerhof
<b>vc-relax</b>	Variable-cell relaxation
<b>VESTA</b>	Visualization for Electronic Structural Analysis
<b>DOS</b>	Density of states
<b>PDOS</b>	Projected density of states
<b>TDOS</b>	Total density of states
<b>NEB</b>	Nudged elastic band
<b>PEC</b>	Photoelectrochemical Cell

# List of Symbols

$O_i$	Oxygen interstitial
$Fe_i$	Iron interstitial
$V_{Fe}$	Iron Vacancy
$V_o$	Oxygen vacancy
$pO_2$	Partial pressure of oxygen
$\mu$	Mobility of charge carriers
$A$	Pre-factor term
$E_{ac}$	Activation energy
$k_B$	Boltzmann constant
$T$	Temperature condition
$\omega$	Phonon frequency
$t$	Small polaron hopping amplitude
$\sigma$	Electronic conductivity
$n$	Charge carrier concentration
$a,b,c$	Lattice constants
$U$	Hubbard U value
$\nu$	Poisson's ratio
$\epsilon_x$	Strain in x-direction
$\epsilon_y$	Strain in y-direction
$\epsilon_z$	Strain in z-direction
$\epsilon_{  }$	In-plane strain
$\epsilon_{\perp}$	Perpendicular strain
$E_{VB/CB}(\vec{k})$	Valence or conduction band Eigen values
$E_{max}$	Energy at the edge of the band
$\vec{k}_{max}$	K-points in the reciprocal space
$m_x^*, m_y^*, m_z^*$	Principal masses in x, y and z-directions

$E_{self-trapping}$	self-trapping energy
$E_{small\ polaron}$	energy of small polarons
$E_{large\ polaron}$	energy of large polarons (or free carriers)
$m_0$	Mass of an electron

# Chapter 1

## Introduction

In this section, we first present the study's motivation in subsection 1.1. Then, we discuss the aims and objectives of the study in subsection 1.2. Finally, we closed the chapter by stating the thesis outline in subsection 1.3.

### 1.1 Motivation for the study

According to the International Energy Agency (IEA), there is projected increase in global energy demand by a significant amount of 4.6% in 2021 and 3.1% in 2022, surpassing pre-pandemic levels. The report notes that the growth is driven by emerging economies, particularly in Asia, and the increasing electricity demand, which is expected to rise by 4.5% in 2021 and 3.5% in 2022<sup>1</sup>. The IEA assumes that the vaccination rollout will facilitate a sustained economic recovery, increasing energy demand. However, the report cautions that the pandemic's uncertainty and potential impact on short-term energy demand cannot be disregarded. The IEA report does not provide a specific projection for 2023, but the demand is expected to continue to rise as the global economy rebounds from the pandemic<sup>1</sup>. This surging global energy demand drives the heavy reliance on energy sources like fossil fuels, leading to the emission of CO<sub>2</sub> and the subsequent onset of climate change. Climate change, a consequence of both natural processes and human activities, disrupts weather patterns and amplifies greenhouse gas emissions. For instance, in 2018, the world witnessed a staggering 315 climate-induced disasters, impacting over 69 million individuals.<sup>2</sup> These disasters, encompassing wildfires, floods, droughts, and storms, accounted for approximately 93 percent of the financial damages, tallying up to \$131.7 billion.<sup>2</sup> The repercussions of climate change extend to vulnerable domains such as public health, food security, ecological balance, infrastructure integrity, water resources, and human habitats.<sup>2</sup> Therefore, to combat the perils of climate change, it becomes imperative to rely on dependable and sustainable energy sources.

The pursuit of renewable energy has led us to harness the power of wind, solar, biomass, geothermal, and wave tidal sources<sup>3</sup> to fulfill our energy needs. Nevertheless, these sources have their limitations, mainly due to their intermittent nature. Additionally, one of the key components

in solar cells, silicon, is predominantly derived from a fossil fuel-based manufacturing process that emits a significant amount of CO<sub>2</sub> into the environment. Compensating for the CO<sub>2</sub> emissions produced during silicon manufacturing can take up to three years<sup>4</sup>. However, we remain optimistic as technological advancements are poised to revolutionize silicon production, reducing its environmental impact and ushering in a greener future<sup>4</sup>. In light of the environmental considerations, how can we effectively address the energy demand while maintaining a sustainable approach?

Hydrogen has emerged as a promising energy carrier, primarily attributed to its unique attribute of generating no carbon dioxide (CO<sub>2</sub>) emissions upon combustion. However, it is essential to note that hydrogen is recognized as an energy carrier rather than an energy source. Hydrogen is an energy carrier for several reasons. Firstly, it can be produced from water through electrolysis or fossil fuels through natural gas reforming. Secondly, hydrogen can be converted into electricity at higher efficiencies than other fuels, making it a highly efficient energy carrier. Thirdly, hydrogen can be transported over long distances through pipelines or in liquid form. Finally, hydrogen can be stored in gaseous forms, liquids or solid forms, making it a flexible and versatile energy carrier<sup>4</sup>. Regardless of having the finest fuel properties, it is scarce in nature. As a result, how can we create a huge amount of hydrogen at a low environmental cost to fulfil the energy demand?

Currently, a variety of processes are being employed for hydrogen generation. Among these processes, the most prevalent techniques are steam reforming<sup>5</sup>, water electrolysis<sup>6</sup>, and photoelectrochemical water splitting, with the latter being the prime focus of this dissertation. As depicted in [Figure 1](#), a photoelectrochemical cell (PEC) utilizes solar energy to cleave water into hydrogen and oxygen in the presence of a photoanode material serving as a catalyst. In this cell, when a photon impinges on the semiconductor/electrolyte interface, it gives rise to an electron-hole (e<sup>-</sup>/h<sup>+</sup>) pair. While the hole (h<sup>+</sup>) triggers the production of oxygen by reacting with water at the interface, the electron follows a path through the external circuit to the cathode, where hydrogen is generated.<sup>4</sup>

The photoanode materials commonly used include TiO<sub>2</sub><sup>7</sup>, BiVO<sub>4</sub><sup>8-10</sup>, WO<sub>3</sub><sup>11</sup>, and  $\alpha$ -Fe<sub>2</sub>O<sub>3</sub><sup>12</sup> (or hematite). Among the class of semiconductor materials for photoanode, hematite, as depicted in [Figure 2](#), exhibits an array of advantageous properties including abundance in the



earth's crust, non-toxicity, favorable stability, low cost, and sensitivity to the visible light spectrum<sup>13</sup>. Nevertheless, in contrast to other photoanode materials, its primary drawback stems from a shorter hole diffusion length, approximately ranging from 2-4 nm, and subsequently low electronic conductivity. Consequently, the photogenerated charge carriers tend to recombine<sup>14</sup>, leading to a low conductivity on the scale of  $10^{-2} \text{ cm}^2 \text{ V}^{-1} \text{ s}^{-1}$ <sup>14</sup> and sluggish kinetics of the surface reactions<sup>14,15</sup>, impeding its application as a photoanode. Despite these limitations, hematite has gained significant interest as a photoanode material for PEC hydrogen generation, and various techniques such as nanostructuring, doping, modification of surface/interface interactions, and heterojunctions have been implemented to tackle these challenges<sup>13</sup>.

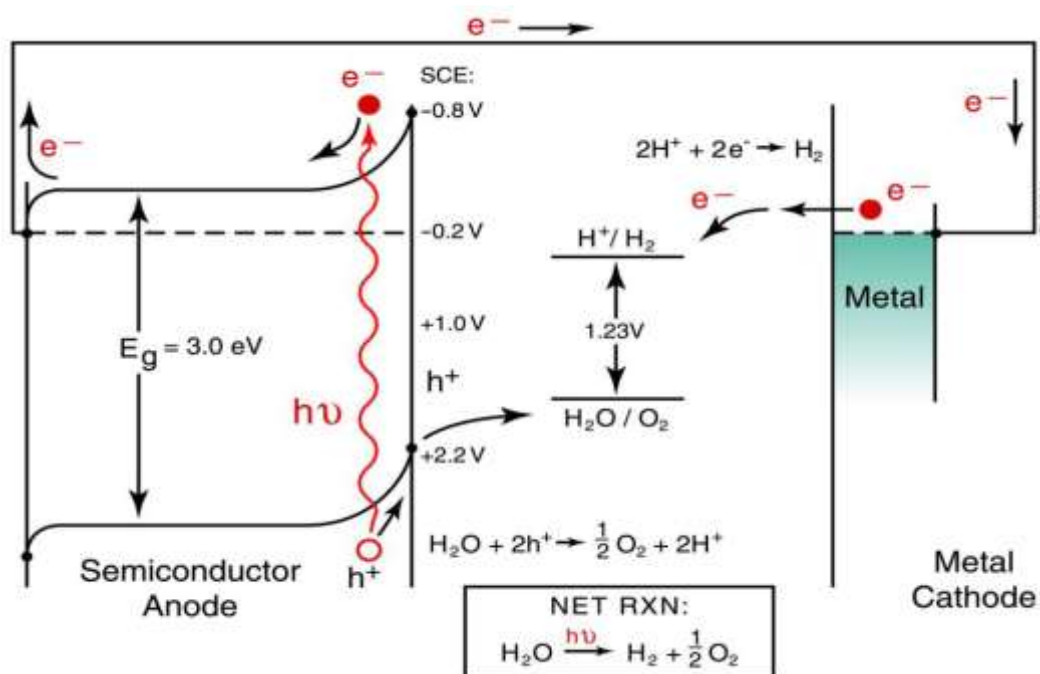


*Figure 1. Schematic representation of a photoelectrochemical cell showing the anode (semiconductor material) and the cathode (metal cathode)<sup>4</sup>.*

The approach of nanostructuring enables a significant increase in interfacial area, which in turn enhances light absorption. This phenomenon leads to more effective generation and separation of charge carriers<sup>17,18</sup>. To increase the density of charge carriers and improve the conductivity of hematite, elemental doping has been employed, with the use of elements such as Si<sup>19</sup>, Sn<sup>20</sup>, and Ti<sup>21</sup>. Another approach is the heterojunction method, which involves the use of different materials interfacing with each other to increase the separation of photogenerated charge carriers<sup>13</sup>.

Additionally, surface/interface modification can be achieved through the coating of the hematite surface with elements such as cobalt, iridium, and ruthenium. This process leads to an increase in the kinetics of the water oxidation reaction on the surface of hematite<sup>13,14,22</sup>.

In addition to the issue of the short diffusion length of holes in hematite, recombination between holes and electrons assisted by intrinsic point defects in hematite is yet another issue. As stated by Shousha et al.,<sup>23</sup> the predominant ionic defect in hematite under high partial pressure of oxygen is the iron vacancy. Notably, certain photogenerated holes possess a proclivity for entrapment within these defects in close proximity to the surface of the hematite. These defects are rendered effective high oxygen partial pressure when submerged in water. This trapping is assisted by the slow diffusion of these holes. Subsequently, this trapping facilitates the undesirable process of recombination between the trapped hole and a mobile electron. As such, if holes were originally fast diffusion species, their trapping probability becomes small, and their eventual recombination rate becomes low. As the literature mentions, the small polaron and free electrons co-exist in hematite<sup>24</sup>. This finding opens the possibility of improving the conductivity in hematite through mechanical strain. The idea is that mechanical strain can turn both small polaron electrons and small polaron holes into large polarons, which would increase their mobility, making it difficult to trap holes or recombine them.

## **1.2 Aims and Objectives**

It is postulated that the application of mechanical strain is capable of inducing a fundamental modification in the electronic and ionic characteristics of a given material.<sup>25</sup> In addition, it can also change the magnetic properties<sup>26–28</sup>, transport properties, reaction energy landscape, and defect concentration in a material<sup>29,30</sup>. Herein, we aimed to understand the effect of biaxial mechanical strain on changing the electronic conductivity of hematite. Prior work showed that small slow polarons predominate in strain-free hematite over large fast polarons, but they co-exist<sup>24</sup>. Our analysis of strained hematite examines three factors. First, the ability of the strain to flip the predominance in favor of large polarons. Second, tuning the effective mass of large polarons by strain. Third, the change of the electronic bandgap via strain. The analysis is performed using density functional theory calculations employing on-site Hubbard U terms on oxygen p-states and iron d-states. The biaxial strain was applied in increments of 0.5% from -5% to +5%. Our study provides guidelines on modulating the electronic conductivity of hematite, which can

encourage its use as a photocatalyst for hydrogen production to meet the increasing energy demand and curb the effect of climate change.

### **1.3 Thesis Outline**

The present thesis is structured in the following manner. Chapter 2 provides an in-depth discussion of the research that has been conducted on hematite as a photoanode material in the past, along with its defects. Additionally, Chapter 3 expounds upon the computational approach that has been adopted for this research. Furthermore, Chapter 4 presents the results and delves into the impact of biaxial strain on the electronic conductivity of hematite. Finally, Chapter 5 concludes the research with a comprehensive summary and highlights areas for future exploration.

# Chapter 2

## Literature review

In this section, first, we present the background information on hematite as a photoanode material in subsection 2.1. Then, we explain its optical and electronic bandgaps in subsection 2.2. After that, we present the defect chemistry of hematite in subsection 2.3. In subsection 2.4, we discuss polaron formation in hematite, followed by polaron mobility in subsection 2.5. We then went ahead to discuss the electronic conductivity in subsection 2.6. Finally, we closed the chapter by examining the role of mechanical strain in improving the electronic conductivity of materials in subsection 2.7.

### 2.1 Hematite as a photoanode material

$\alpha$ -Fe<sub>2</sub>O<sub>3</sub> (hematite) belongs to the  $R\bar{3}c$  space group. It has a corundum-type structure in which oxygen (O) atoms are in a hexagonal closed-packed (HCP) arrangement, and iron (Fe) atoms are in  $2/3$  of the octahedral site. Six O atoms surround each Fe atom. Hematite primitive cell, rhombohedral structure, has two formula units, while the conventional cell, hexagonal structure, has six formula units, as shown in [Figure 2](#)<sup>31,32</sup>. In addition, hematite has an antiferromagnetic ordering below the Neel temperature (953K) and shows ferromagnetic behavior in the basal plane, that is, (111) in primitive and (0001) in HCP, above the Morin temperature (260K)<sup>33,34</sup>.

Hematite, possessing an experimental bandgap of 1.8 to 2.2 eV<sup>35–37</sup>, is a photoanode material of great significance due to its ability to absorb the visible region of the solar spectrum. It also exhibits a theoretical solar-to-hydrogen conversion efficiency of 13%<sup>38,39</sup>. Moreover, hematite is characterized by its abundance in the earth, non-toxicity, stability, low cost, and its responsiveness to the visible light spectrum<sup>13</sup>. Nevertheless, compared to other photoanode materials, its primary drawback is the shorter diffusion length of holes, which measures approximately 2-4 nm, as well as its overall low electronic conductivity. This leads to the recombination of the photogenerated

charge carriers<sup>14</sup>, sluggish kinetics of the surface reactions<sup>14,15</sup>, and low conductivity on the order of  $10^{-2} \text{ cm}^2 \text{ V}^{-1} \text{ s}^{-1}$ <sup>14</sup>, all of which adversely affect its application as a photoanode.

Henceforth, the present chapter will concentrate on the intricate electronic configuration, defect chemistry, the formation of polarons, and the aftermath of polaron formation in hematite.

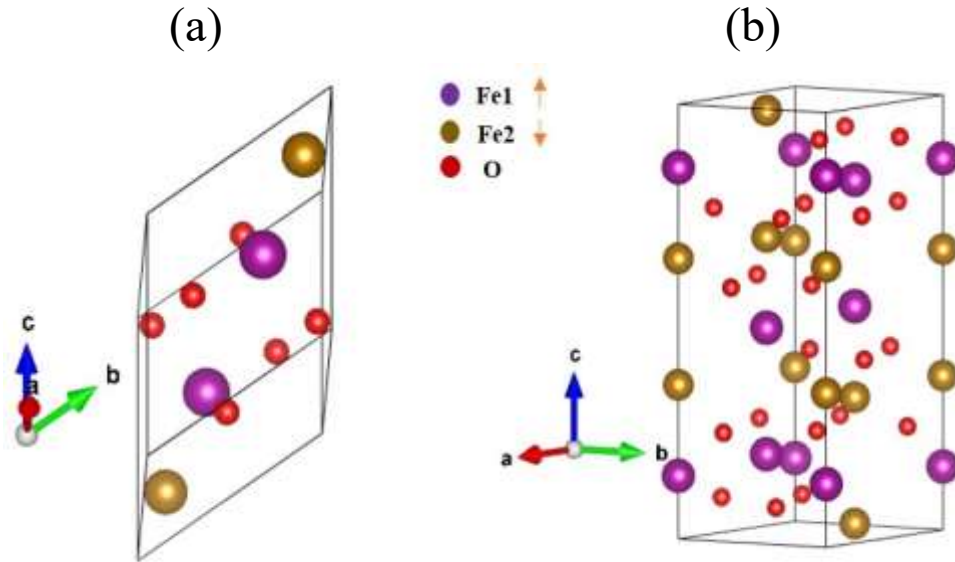


*Figure 2. Schematic diagram of the unit cells of hematite. (a) The primitive cell of hematite has a rhombohedral crystal structure with ten atoms and lattice parameters of  $a = b = c = 5.474 \text{ \AA}$ . (b) The conventional cell has a hexagonal corundum crystal structure with 30 atoms and lattice parameters of  $a = b = 5.069 \text{ \AA}$ ,  $c = 13.805 \text{ \AA}$ . The diagram was generated using the VESTA visualization software package<sup>40</sup>.*

## 2.2 Electronic bandgap and electronic structure of hematite

The ionic bonding between the oxygen atom and metal atom, the nature of the crystal symmetry, and the hybridization between the atoms dictate the electronic bandgap and electronic structure of metal oxides<sup>40,41</sup>. For instance, materials like  $\text{Al}_2\text{O}_3$ ,  $\text{ZnO}$ , and  $\text{Ga}_2\text{O}_3$  tend to have large band gaps because of the significant energy difference between the metal and oxygen ligands and the electronic band structure composed of the oxygen-2p orbitals and the metal s-orbitals. However, metal oxide like hematite sustained a bonding between the cation 3d orbital and anions s-orbitals, lowering the bandgap and making it a prime material for photocatalysis.

Traditionally, the categorization of electronic bandgaps is based on their energy levels and subsequently represented as density of states, as illustrated in Figure 3. The Valence Band Maxima (VBM) and the Conduction Band Maxima (CBM) constitute the primary frontier orbitals in several metal oxides, including hematite. The O-2p and Fe-3d orbitals comprise the VBM of hematite, while the CBM predominantly comprises Fe-3d orbitals, as showcased in Figure 3<sup>24</sup>. The electronic structure of metal oxides can be explicated by the crystal field theory<sup>43</sup>, which postulates that oxygen anions can have various geometrical arrangements around the metal cation. In the case of hematite, the oxygen atom has an octahedral arrangement around the Fe atoms. This type of arrangement leads to the crystal field splitting of Fe-3d orbitals into  $t_{2g}$  symmetry and  $e_g$  symmetry<sup>44</sup>. In a perfect crystal, the  $t_{2g}$  orbital symmetry is stabilized while the  $e_g$  is destabilized. However, the formation of point defects, for instance, iron interstitials, changes the stabilization and splitting of the  $e_g$  and  $t_{2g}$  orbitals<sup>45,46</sup>.

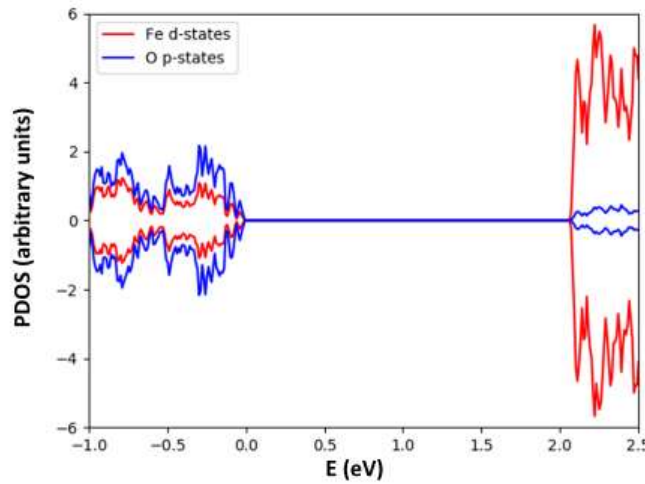


Figure 3. The Partial Density of State (PDOS) of hematite showing the contribution of iron 3d orbital and oxygen 2p orbital to the density of states<sup>24</sup>.

### 2.3 Defect Chemistry of Hematite

Hematite is an n-type semiconductor material. Although, there is a debate on the intrinsic source of the electronic conductivity in an undoped hematite. Intrinsic defects are defects that are thermodynamically stable in a material. In other words, they are always present in a crystal and cannot be removed by heat treatment such as annealing. The intrinsic defects in an undoped

hematite include interstitials  $X_i$ , both oxygen ( $O_i$ ) and iron interstitials ( $Fe_i$ ), vacancies  $V_x$ , both iron vacancy ( $V_{Fe}$ ) and oxygen ( $V_o$ ) vacancies, antisites and free electron-hole pairs<sup>24</sup>. Also, these intrinsic defects occur at different charge states and have different formation energy<sup>24,47</sup>. Thus, this implies that defects with the lowest formation energy are more likely to occur. Nonetheless, it is noteworthy that the distribution of said anomalies undergoes modification in correspondence with alterations in temperature, as evidenced by the research conducted by Smart et al.<sup>48</sup> and Shousha et al.<sup>24</sup> For example, Smart et al.<sup>48</sup> did a theoretical study to understand the concentrations of the various intrinsic defects at different synthesis temperatures and partial pressure conditions. The analysis ignores antisite defects because they are thermodynamically unfavorable. It was found that the n-type defects, that is, oxygen vacancies ( $V_o$ ) and iron interstitials ( $Fe_i$ ), are the primary source of conductivity in an undoped hematite due to their low formation energies as compared to the p-type defects, oxygen ( $O_i$ ) and iron vacancy ( $V_{Fe}$ ). Since  $V_o$  and  $Fe_i$  are the n-type defects in hematite, they are the primary suspects for the small electron polaron formation in the material<sup>24</sup>. Furthermore, the study also confirms that the concentration of free delocalized charge carriers was negligible, implying that the material's conductivity is dictated by the small polarons with lower mobility<sup>24</sup>.

In another instance, Shousha et al.<sup>24</sup> studied the concentration of the point defects at 700 K and 1100 K synthesis temperatures. At both temperatures, the defect concentrations showed similar trends. For instance, at an extremely low and low partial pressure of oxygen ( $pO_2$ ),  $Fe_i$  with (+1) and (+2) and the majority of defects, respectively. While at an intermediate and high partial pressure of oxygen ( $pO_2$ ), delocalized charge carriers (electrons and holes) and oxygen vacancies with (+3) charged states are the dominant defects, respectively. Also, the study confirmed the co-existence of both small polarons and delocalized charged carriers in hematite with small polarons in higher concentrations. Overall, the above studies have confirmed the presence of small polarons in hematite. Both investigations indicate that polarons constitute the predominant portion of charge carriers in hematite, thereby accounting for the material's generally subdued conductivity.

It is worth mentioning that, hematite typically crystallizes in a polycrystalline form, which means it comprises multiple crystal domains or grains. Polycrystalline hematite consists of numerous small crystalline regions or grains, separated by grain boundaries. These boundaries in addition to other structural imperfections, including dislocations and vacancies, can impact the

material's electronic properties<sup>49</sup>. In a recent experimental investigation conducted by Husek et al.,<sup>50</sup> they examined the effects of crystallinity on charge trapping at the surface of hematite using static extreme ultraviolet (XUV) resonant Auger (RA) spectroscopy. Surprisingly, their findings demonstrated that the crystallinity of the material had a negligible impact on charge trapping<sup>50</sup>. This implies that whether hematite is in a polycrystalline form or a single crystal, the surface charge trapping behavior remains relatively insensitive to the material's crystalline structure.

## **2.4 Polarons in hematite**

The electrons present in a perfect crystal can be effectively characterized in relation to the periodic wave function. However, the aforementioned crystal is not naturally occurring owing to the presence of defects. The presence of defects in a crystal results in the disruption of the periodicity and hence, culminates in the formation of localized states<sup>51</sup>. The formation of these localized states is called polarons. Holstein (1959) states, "A polaron is a quasiparticle originating from the interaction between charge carriers, that is, electrons or holes, and lattice ion vibration<sup>52,53</sup>." Furthermore, due to their electrostatic forces, these quasiparticles alter the material's crystal structure to attract ions with opposite charges. For example, if the charge carrier trapped is an electron, it will attract ions with a net positive charge, altering the atoms' atomic arrangement in the crystal and vice versa. The formation of the localized states is specifically favored in polar semiconductors and transition metal oxide, for instance, hematite<sup>44</sup>. The coupling of the excess charge carriers with the ions is described as either weak or strong interactions. In the case of weak coupling, the polaron formed is called large polarons. Besides, when the coupling is strong, they are called small polaron<sup>54</sup>. Furthermore, as shown in [Figure 4\(b\)](#), large polarons are described with a delocalized wave function spread over many atoms. While small polarons, as shown in [Figure 4 \(a\)](#), have wavefunctions localized to one atom. Both experimental and theoretical studies have confirmed the existence of small and large polarons in hematite.<sup>24,48,55</sup>



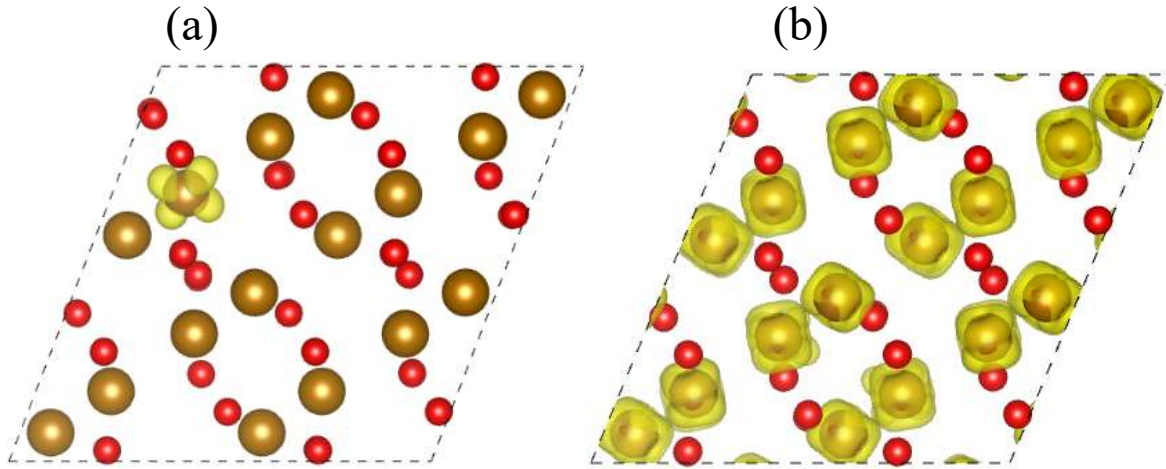


Figure 4. Visualization of Charge density isosurfaces in  $\alpha\text{-Fe}_2\text{O}_3$  shown in yellow for the cases; (a) small polaron electron localizing on an Fe ion, (b) large polaron electron (free electron) delocalized on the d-states of Fe ions. The isosurface level for the small polarons was maintained at  $0.019 \text{ e}/\text{\AA}^3$  while for the free carriers the isosurface is maintained at  $0.02 \text{ e}/\text{\AA}^3$ . Gold (large) and red (small) represents Fe and O ions respectively. These images are generated using VESTA visualization software package<sup>40</sup> in this work.

## 2.5 Polarons Mobility in Hematite

Polaron mobility plays an essential role in the conductivity of oxide materials. To improve the electronic conductivity of metal oxides, understanding the mobility of polarons in these materials is crucial<sup>34</sup>. Understanding polaron mobility could enhance the performance of many technologies like photovoltaics<sup>56,57</sup>, batteries<sup>58,59</sup>, photocatalyst for water splitting<sup>60–62</sup>, thermoelectric<sup>63</sup>, and solid-oxide fuel cells<sup>64</sup>. Different diffusion mechanism has been established for both small and large polaron, which depends on temperature, the strength of the electron-phonon coupling, the bandwidth of the electrons, and the phonon frequency<sup>54</sup>.

In many functional oxide materials, conductivity occurs through the hopping of small polaron<sup>33,65</sup>, described as phonon-assisted. The hopping mechanism of small polaron is modeled within the DFT framework by Marcus theory<sup>66</sup>. Since the small polaron hopping is phonon-assisted, the mobility is usually less than  $1 \text{ cm}^2\text{V}^{-1}\text{S}^{-1}$  but increases with temperature<sup>34,54</sup>. The mobility ( $\mu$ ), as expressed in [equation 1](#)<sup>34</sup>, depends on temperature (T), activation energy ( $E_{ac}$ ),

and the Boltzmann constant ( $k_B$ ). The activation energy ( $E_{ac}$ ) can assume a different form; it can be either adiabatic or non-adiabatic (diabatic). It is adiabatic when the hopping amplitude ( $t$ ) between the neighboring sites is much greater than the phonon frequency ( $\omega$ ), that is, ( $t \gg \omega$ ). However, it is diabatic when the hopping amplitude ( $t$ ) between the neighboring sites is much less than the phonon frequency ( $\omega$ ), that is, ( $t \ll \omega$ ). The activation energy ( $E_{ac}$ ) and the prefactor ( $A$ ) can be determined directly from first principle calculation by the linear interpolation calculations or nudged elastic band (NEB).<sup>54</sup>

$$\mu = A \exp\left(-\frac{E_{ac}}{k_B T}\right)$$

1

In the case of large polarons, they are characterized by a delocalized wavefunction that spreads over a significant number of atoms, presented in [Figure 4 \(b\)](#). . The coherent transport of large polarons can sometimes be related to free carriers, although with some distinctive differences<sup>54</sup>. For instance, large polarons have a large effective mass compared to free electrons; hence, they move slower than free charge carriers. In addition, large polarons decrease their mobility with increased temperature and are scattered at times by phonons. Therefore, the mobility of large polarons can be modeled by the Boltzmann equation<sup>67,68</sup>.

## 2.6 Conductivity in hematite

The underlying principle of defect engineering is to enhance the abundance of charge carriers in oxide photocatalysts<sup>4</sup>. The conductivity ( $\sigma$ ) of an n-type semiconductor material is contingent upon both the mobility ( $\mu$ ) and concentration ( $n$ ) of charge carriers, as given in [equation 2](#)<sup>69</sup>.

$$\sigma = qn\mu$$

2

This implies that doping n-type materials with high-valence dopants can increase the concentration of the majority charge carriers by creating more shallow defects and hence increasing the conductivity of the materials. In this regard, various n-dopant like Sn<sup>70,71</sup>, Si<sup>72</sup>, Ti<sup>24,32,73</sup>, and Ge<sup>74</sup> have been used as dopants in hematite. However, the main drawback is that the doping mechanism is not fully understood, especially when excess charge carriers create more small polarons in the materials. For example, doping hematite with Si has been reported to increase the conductivity by increasing concentration of small electron polarons and their mobility<sup>75</sup>. However, this is not the case for all dopants. For instance, doping hematite with Sn has been reported to increase the activation barrier for hopping the small polarons, which is disadvantage<sup>70</sup>. Since both experimental and theoretical studies<sup>24,48,55</sup> have confirmed the co-existence of small electron polarons and free electrons in hematite with the concentration of the small polarons in higher magnitude, <sup>24</sup> this calls for an approach that will flip energy landscape in favor of large polarons in hematite probably through crystal engineering.

## **2.7 Can mechanical strain improve the electronic conductivity of hematite?**

Strain engineering is viewed as the novel approach for tuning the properties of materials in a way that does not require a change in the chemical composition via intentional doping. In addition, mechanical strain can make an essential alteration in the electronic and ionic properties of a material<sup>25</sup>. For instance, in semiconducting elements like silicon, uniaxial and biaxial strain is applied to enhance the electron mobility in transistors, reducing power consumption and improving performance<sup>76</sup>.

Furthermore, it can change the magnetic properties<sup>26–28</sup>, transport properties, reaction energy landscape, and defect concentration in a material<sup>29,30</sup>. For example, in a study published by Chi et al., using first principle calculations, the biaxial strain was applied to understand the alteration of defect concentration in SrTiO<sub>3</sub>, an essential functional oxide material for nonvolatile memories and thin film electronic devices <sup>25</sup>. In this study, they understood that the prevalence of electronic defects under the biaxial compressive strain were free electrons, while small polarons were under the biaxial tensile strain. Moreover, in another study reported by Jannotti et al.<sup>77</sup>, the biaxial strain was applied on SrTiO<sub>3</sub> by DFT methods to understand the effect of strain on the electron mobility in the material. It was concluded that due to the tensile strain applied to the

materials, the effective mass of the electrons was lowered, resulting in higher mobility of electrons in the material.

The studies above have shown that biaxial strain can alter the electronic defects and increase the electrons' mobility in  $\text{SrTiO}_3$ . Besides, biaxial strain can also reduce the bandgap of a material. For instance, Kelaidis and co-workers<sup>78</sup> studied the impact of strain on the bandgap of undoped and doped anatase  $\text{TiO}_2$ . This study applied both uniaxial and biaxial strain using a first principles approach to the material. For the case of the undoped anatase  $\text{TiO}_2$ , the biaxial strain was applied, which resulted in bandgap reduction from 3.2 eV to 2.9 eV. Likewise, the biaxial strain on the doped anatase resulted in a decrease in the bandgap and the introduction of a deep state in the bandgap.

Moreover, Wang et al.<sup>79</sup> studied the sensitivity of the bandgap of perovskite  $\text{BaSnO}_3$  to strain. Here, hydrostatic and biaxial strains from -3% to +3% were studied using DFT calculations. For the hydrostatic strain, a change from 3.7 eV to 2.51 eV in the bandgap was observed, while for the biaxial strain, a change in the crystal structure combined with a change in the bandgap from 4.46 eV to 1.89 eV was collectively observed.

Furthermore, experimental studies using epitaxial film growth mechanism have shown the impact of biaxial strain on bandgap tuning in materials. In particular, a research conducted by Choi and Lee<sup>80</sup> have shown that  $\text{Bi}_4\text{Ti}_3\text{O}_{12}\text{-LaCoO}_3$  (BiT-LCO) epitaxial film grown on (110) surface of mono-crystal orthorhombic  $\text{NdGaO}_3$  (NGO) and (001) surface of cubic  $\text{SrTiO}_3$  (STO), reduce the bandgap of the thin film by epitaxial strain. This results in the bandgap reduction of the thin film from a magnitude of 3.55 eV to a magnitude of 2.55 eV.<sup>80</sup>

With regards to hematite, prior studies on hematite by ref<sup>81</sup> have reported a reduction in the bandgap of the material by the application of mechanical strain based on density functional theory calculations. Therefore, different studies, as discussed above, have illustrated an alteration in the properties of functional oxide materials due to mechanical strain. The use of strain engineering has been found to enhance various properties such as electronic structure, crystal structure, electron mobility, and electron effective mass according to density functional theory calculations. However, there are limited studies on the effect of strain on the large and small polarons of hematite. Therefore, this study aims to comprehend the conductivity of hematite by

applying mechanical strain through density functional theory methods, based on evidence of the impact of strain on the electronic conductivity of functional oxides.

# Chapter 3

## Computational Methods

In this section, first, we present the first principle parameters employed in this work in subsection 3.1. Then, we explained how we apply biaxial strain to the material in subsection 3.2. After that, we give a detailed explanation for calculating the effective masses of charge carriers in hematite in subsection 3.3. Finally, we describe the methodology for calculating the self-trapping energy in subsection 3.4.

### 3.1 First Principle Parameters

The primitive cell of hematite has a rhombohedral crystal structure with ten atoms and lattice parameters of  $a = b = c = 5.474 \text{ \AA}$ , and the conventional cell has a hexagonal corundum crystal structure with 30 atoms and lattice parameters of  $a = b = 5.069 \text{ \AA}$ ,  $c = 13.805 \text{ \AA}$ . Density functional theory (DFT) simulations based on generalized gradient approximation (GGA) using the Perdew–Burke–Ernzerhof (PBE)<sup>82</sup> functional is used. Ultra-soft pseudo potentials<sup>83–86</sup> adopted from the PSLIBRARY<sup>83</sup> is used for both Fe and O. The Fe pseudopotential has 16 valence electrons, while the O pseudopotential has 6 valence electrons. The plane wave cut-off energy is set at 90 Ry, whereas the charge density cut-off was 1080 Ry. These were the recommended values for the pseudopotentials in Ref<sup>85</sup>. An open-source plane-wave Quantum Espresso software package<sup>87,88</sup> is utilized for all DFT calculations. For all the calculations, initially, the study is conducted using a Hubbard U correction value of 3.0 eV and 7.0 eV on both the Fe-3d state and O-2p state, respectively. Then, we perform another study where we change the magnitude of the Hubbard U value on Fe and O to 4.0 eV and 6.5 eV, respectively. These values were tested and recommended by Ref<sup>24</sup>. In addition, these U values achieved the expected behavior of the total energy of the DFT calculation, which should be a linear dependence on the electronic occupation, as suggested by Koopman theorem<sup>89</sup>. Also, the U values allowed for localizing small polaron electrons and small polaron holes.

### 3.2 Density Functional Theory Calculations and Biaxial Strain

Regarding density functional theory calculations, a variable-cell relaxation (vc-relax) in Quantum Espresso was performed on the conventional unit cell, as shown in [Figure 2 \(b\)](#), with 30 atoms to obtain the optimized lattice constants and relaxed atomic positions. Then, we apply biaxial strain ( $\epsilon_x = \epsilon_y \neq \epsilon_z$ ) from -5 % to +5 % on an interval of 0.5 % to the conventional cell with the hexagonal crystal structure of hematite resulting in an in-plane strain ( $\epsilon_{||}$ ), and allowing the structure to relax along the z-direction leading to a perpendicular strain ( $\epsilon_{\perp}$ ). After relaxation, we then convert the conventional strained structure to the primitive cell of 10 atoms using the VESTA software package<sup>40</sup> to maintain the strained volume. This reduces the computational expenses of working with 120 atoms supercell of the conventional hexagonal corundum crystal structure. A  $2 \times 2 \times 2$  k-point is used for the small polarons simulation. The k-point was sampled using the gamma-centered Monkhorst–Pack scheme, and a convergence test was done. For large polarons, the k-point is increased to  $3 \times 3 \times 3$ . Furthermore, we applied Gaussian smearing of 0.004 Ry to facilitate the electronic convergence of the small polarons defect state, whereas 0.01 Ry Marzari-Vanderbilt smearing is added to the large polarons. It is worth noting that magnetization is also enabled in our calculations, where the magnetic moment is set to provide the antiferromagnetic state in hematite.

### 3.3 Band Effective mass

The determination of the effective mass of charge carriers in semiconductors can be achieved by utilizing either the density of states (DOS)<sup>90–92</sup> method or the band structure approach<sup>91–93</sup>. However, the former technique tends to overestimate the masses due to its exclusive focus on heavy masses<sup>92</sup> and its inability to accommodate materials with anisotropic band structures, such as hematite<sup>92</sup>. Consequently, we resort to the band structure approach for accurately calculating the effective masses of charge in hematite. The band curvature effective mass method involves calculating masses based on the curvature of the bands at the valence band maximum (VBM) and the conduction band minimum (CBM). This approach relates the effective masses to the inverse of the band structures curvatures at the extrema points using [equation 3](#);<sup>90,94</sup>

$$E_{VB/CB}(\vec{k}) \approx E_{max/min} + \frac{\hbar^2}{2m_x^*}(k_x - k_{x-max})^2 + \frac{\hbar^2}{2m_y^*}(k_y - k_{y-max})^2 + \frac{\hbar^2}{2m_z^*}(k_z - k_{z-max})^2$$

3

where  $E_{VB/CB}(\vec{k})$  is the valence band or conduction band energy eigenvalues as a function of  $k$ -points in the reciprocal space,  $E_{max/min}$  is the energy at the edge of the band,  $k_{i=x,y,z}$  are the reciprocal lattice points in the  $k$ -space,  $\vec{k}_{max} = (k_x - k_{x-max}, k_y - k_{y-max}, k_z - k_{z-max})$  is the position of the band edges in the reciprocal space, and  $m_x^*, m_y^*, m_z^*$  are the principal masses in the 3-dimensional space. The determination of band curvature can be carried out through the application of a parabolic model to the three-dimensional band structure, with the subsequent acquisition of the second derivatives. This is done independently along three orthogonal lattice directions in the reciprocal space using [equation 3](#)<sup>91,95,96</sup>. However, in our case, the band is somehow anisotropic, which means there can be contributions from the off-diagonal components of the effective mass tensor. This implies that going along the high-symmetry directions alone may not be enough to define the effective masses. Therefore, we used a full three-dimensional paraboloid model suggested by Neufeld and Caspary<sup>92</sup> in [equation 4](#) to account for this.

$$E_{VB/CB}(\vec{k}) \approx E_{max} + \frac{\hbar^2}{2} (m_{xx}^{-1}k_x^2 + m_{yy}^{-1}k_y^2 + m_{zz}^{-1}k_z^2 + 2m_{xy}^{-1}k_xk_y + 2m_{xz}^{-1}k_xk_z + 2m_{yz}^{-1}k_yk_z) + C_xk_x + C_yk_y + C_zk_z$$

4

The method of least squares is employed in order to establish a model that accurately represents all points in proximity to the boundaries of the band. This approach yields the inverse of the effective mass tensor in the form;



$$m^{-1} = \begin{bmatrix} m_{xx}^{-1} & m_{xy}^{-1} & m_{xz}^{-1} \\ m_{yx}^{-1} & m_{yy}^{-1} & m_{yz}^{-1} \\ m_{zx}^{-1} & m_{zy}^{-1} & m_{zz}^{-1} \end{bmatrix}$$

5

The effective mass tensor is then inversed and diagonalized to obtain the principal masses' eigenvalues. Since conductivity at the macroscale is described by the Drude model<sup>93,94</sup>, we then use the Drude model to determine the average effective mass by taking the harmonic mean of the principal masses as shown in [equation 6](#);

$$\langle m^* \rangle = 3 \left( \frac{1}{m_x^*} + \frac{1}{m_y^*} + \frac{1}{m_z^*} \right)^{-1}$$

6

It should be noted that two main points are kept in mind before we calculate the effective masses. First, to describe the anisotropy of the band structure of hematite, the k-points in the reciprocal space must be sufficiently dense enough around the valence band maxima and conduction band minima. This is quite expensive and could be one reason this method is not commonly used. The second point is that the k-points should also converge around the band extrema. It is known that the least square method accuracy depends on the number of points to be fitted. However, we used a convergence criterion since far-away points do not contribute to the effective masses. Studies conducted by ref<sup>92</sup> have found that the sphere's radius converges at 0.15 to 0.3  $2\pi/\text{\AA}$  for most corundum systems, hematite inclusive. Based on this convergence threshold, we can keep only the k-points in the spherical region around the band extrema.

### 3.3 Self-trapping energy

The self-trapping energy depends on the total energy of the localized structure with small polarons and the total energy of the delocalized structure with large polarons. A 2 x 2 x 2 supercell with 80 atoms was created using VESTA visualization software<sup>40</sup> from the strained volumes for the small polarons calculations. To model a hematite crystal with a small or large polaron, we followed the approach outlined in references 23,<sup>32</sup>, and<sup>97</sup>. For the small electron polaron, we took

three steps. First, we replaced one of the Fe ions with an ion having a larger ionic radius, such as Zn, to create the necessary local deformation for localizing the small polaron. Next, we allowed the ions and electrons to relax. Second, we replaced the Zn ion with an Fe ion and increased the Hubbard U value of this ion to 6.0 eV to ensure the localization of the small electron polaron. Finally, we decreased the Hubbard U value of the ion with the electron polaron to 3.0 or 4.0 eV, consistent with the rest of the Fe ions in the crystal, and then allowed the ions and electrons to relax again. The total energy of the final stage was used to calculate the self-trapping energy. For the small hole polaron, we replaced one of the O ions with a Cl ion to create the necessary local deformation for localizing the small polaron. However, since the initial U value of O was 7.0 eV for the initial study and 6.5 eV for the second study, we increased the U value to 10.0 eV in the second stage to ensure small polaron localization. We then allowed the ions and electrons to relax again to obtain the final self-trapping energy. In some cases, particularly with electron localization, complete localization of small polarons was not possible. To resolve this issue, we added a fourth step in which we displaced neighboring O ions and then re-relaxed the ions and electrons, which successfully resolved the localization issue. For large polarons, the hole or electron is delocalized over the O or Fe sites of the supercell. We allowed the ions and electrons to relax to obtain the final self-trapping energy.

One should note that, in practical applications, biaxial strain is typically introduced in a material through epitaxial film growth, where the thermodynamic boundary conditions are fixed temperature and fixed lengths along the epitaxy plane. Under these conditions, the relevant thermodynamic potential to determine favorable structures is a Helmholtz-like potential, which only includes an energy term and an entropy term, but no stress/strain term. Since our study is conducted at 0 K, the Helmholtz-like potential reduces to an energy potential, and we refer to self-trapping as an energy term rather than a free energy term as in [equation 7](#)<sup>25</sup>. A positive self-trapping energy indicates a preference for large polarons, while a negative self-trapping energy indicates a preference for small polarons.

$$E_{self-trapping} = E_{small\ polaron} - E_{large\ polaron}$$

# Chapter 4

## Results and Discussion

In this section, first, we will present and discuss the results on the effect of biaxial mechanical strain on the perfect crystal of hematite. The bandgap, z-axis, and volume as a function of mechanical strain will be discussed in subsection 4.1. After that, we will discuss the effect of the mechanical strain on the effective mass of charge carriers in hematite in subsection 4.2. Next, we examine the role of mechanical strain on the energy landscape of polarons in hematite in subsection 4.3, where the self-trapping energy will be analyzed. Finally, in subsection 4.4 we discuss the implications our results on hematite as a photoanode for photoelectrochemical water splitting.

### 4.1 Prefect crystal of hematite

First, we will start with the effect of biaxial strain on the electronic bandgap of hematite. It is known that the ionic bonding between the oxygen atom and metal atom, the nature of the crystal symmetry, and the hybridization between the atoms dictates the electronic bandgap and electronic structure of metal oxides<sup>40,41</sup>. For instance, materials like  $\text{Al}_2\text{O}_3$ ,  $\text{ZnO}$ , and  $\text{Ga}_2\text{O}_3$  tend to have large bandgaps because of the significant energy difference between the metal and oxygen ligands, and electronic band structure composed of the oxygen 2p (O-2p) orbitals and the metal s orbitals. However, transition metal oxide like hematite sustained a bonding between the iron 3d (Fe-3d) orbitals and oxygen s (O-s) orbitals, lowering their electronic bandgap and making it a prime material for photocatalysis. For our initial study using Hubbard U values of  $U(\text{Fe}) = 3.0$  eV and  $U(\text{O}) = 6.5$  eV, we got an electronic bandgap of approximately 2.4 eV for zero-strained hematite, consistent with literature<sup>24,32</sup>. However, when we change the magnitude of the Hubbard U values to 4.0 eV on Fe and 6.5 eV on O, the electronic bandgap increased to around 2.8 eV.

Traditionally, electronic bandgaps are grouped as an energy function and represented as the density of states, as shown in [Figure 5](#). The Valence Band Maxima (VBM) and the Conduction Band Maxima (CBM) comprised the frontier orbitals of most metal oxides, including hematite. In [Figure 5 \(a\)](#), the VBM of hematite comprises O-2p orbitals and Fe-3d orbitals, while the CBM primarily comprises Fe-3d orbitals. This hybridization has an important consequence on forming point defects, polarons localization, and low photocatalytic performance in hematite<sup>44</sup>. We then

start to compress and stretch the material in a biaxial manner. To our surprise, we observed a reduction in the electronic bandgap of the material under both biaxial tensile and compressive strain, as shown in Figure 6. This is also true for both two studies conducted with different Hubbard  $U$  values. A theoretical study in ref <sup>98</sup> also made this observation. Also, it is essential to note that the reduction in the bandgap was more significant in the compressive state conditions. In addition, we also observe that hematite has an indirect bandgap ordering, shown in Figure 5 (b). This finding is consistent with literature<sup>99,100</sup>.

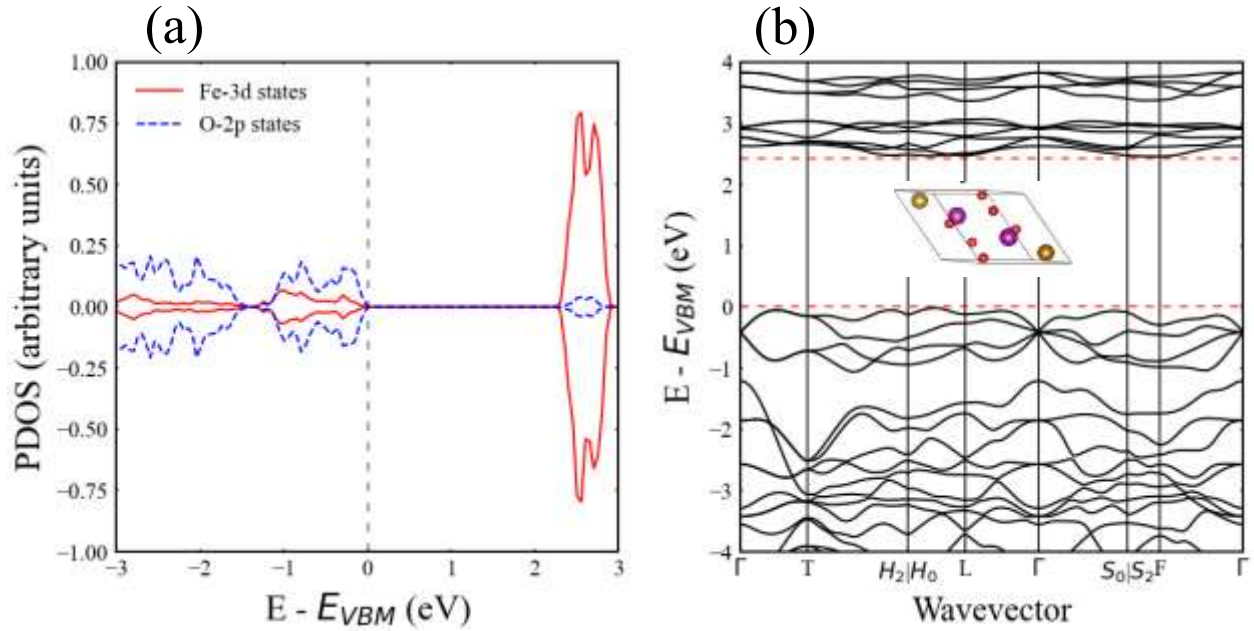


Figure 5. The electronic bandgap of hematite at zero strain for the rhombohedral crystal structure. (a) The Projected density of states (PDOS) of showing the contributions of O-2p orbitals and Fe-3d orbitals to the electronic bandgap of hematite. (b) The band structure along the high-symmetry points ( $\Gamma - T - H_2/H_0 - L - \Gamma - S_0/S_2 - F - \Gamma$ ). It is important to note that hematite has an indirect bandgap.

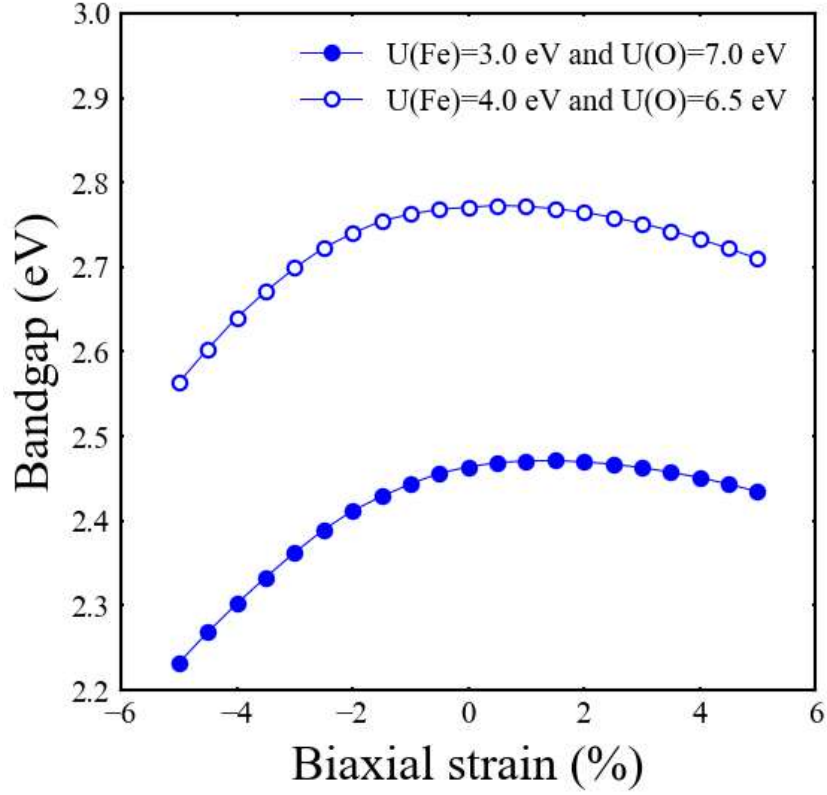


Figure 6. Effect of strain on the bandgap of hematite. The blue-filled points represent the initial study with  $U(\text{Fe}) = 3.0 \text{ eV}$  and  $U(\text{O}) = 7.0 \text{ eV}$ . The white-filled points represent the second study with  $U(\text{Fe}) = 4.0 \text{ eV}$  and  $U(\text{O}) = 6.5 \text{ eV}$ . In both cases, the reduction of bandgap occurs at both tensile and compressive strain but is more prominent in the compressive strain state.

We now focus on the effect of mechanical strain on the volume and the z-axis of the defect-free hematite. Hematite has a rhombohedral crystal structure [Figure 2\(a\)](#). This means it has equal length,  $a = b = c = 5.474 \text{ \AA}^{24,32}$ , where a, b, and c are the lattice constants with unequal angles. The crystal structure of hematite is usually described by the hexagonal crystal structure shown in [Figure 2 \(b\)](#). Here, we based our calculations on the conventional cell of hematite. Changes in physical properties, for instance, volume and z-axis, can occur when a material is subjected to biaxial strain<sup>101</sup>. We start with the volume; in the case of hematite, applying biaxial strain on the (0001) plane perpendicular to the z-axis can cause its volume to decrease. As expected, when we strained the material, we noticed a decrease in volume under the biaxial compressive strain and an increase in volume under the biaxial tensile strain, as shown in [Figure 7](#). The observed behavior can be elucidated by considering the hexagonal structure of hematite, [Figure 2 \(b\)](#), which is composed of

layers alternating between iron (Fe) and oxygen (O). These layers are subjected to compression or stretching under biaxial strain, which causes the material to change. In particular, when the O-Fe layers are compressed along two orthogonal directions, the volume of the material decreases.

In contrast, stretching the O-Fe layers along two perpendicular directions causes the volume of hematite to increase. It is important to note that the increase in volume under the tensile and compressive strain occurred at a slower pace. To better understand this behavior, we calculate the volumetric strain per biaxial of the polaron-free hematite, which is 1.2 for both studies conducted with Hubbard U values, shown in [Figure 7 \(a\)](#) and [Figure 7 \(b\)](#). The resulting value of 1.2 indicates that the material's volume changes slowly because it is attempting to maintain its volume with the polaronic structure. This finding also explains why a higher magnitude of strain is required to alter the energy landscape in favor of large polarons, as discussed in section 4.3.

Furthermore, it is observed that biaxial strain induces changes not only in the volume but also in the z-axis of hematite, in agreement with previous reports<sup>98</sup>. Our computational analysis in [Figure 8 \(a\)](#) and [Figure 8 \(b\)](#) reveals a poisson's ratio ( $\nu$ ) of 0.80 for hematite under biaxial strain. Poisson's ratio is a measure of the ratio of negative perpendicular strain to the transverse strain, with a value of 0.5 for isotropic materials that have the same properties in all directions<sup>102</sup>. However, this value is only applicable to axial strain, and the typical range of poisson's ratio for hematite under axial strain in ambient conditions is between 0.25 to 0.35<sup>103,104</sup>. Since our DFT calculations involve biaxial mechanical strain, we expect a higher poisson's ratio than this range. Our calculated large value of 0.8 for  $\nu$  under biaxial strain explains the small value of 1.2 of the volumetric strain per biaxial strain. For example, under compressive biaxial strain, the large 0.8 Poisson's ratio results in a relatively large expansion in the z-axis of hematite. This collectively results in a tiny reduction in the overall volume of hematite.

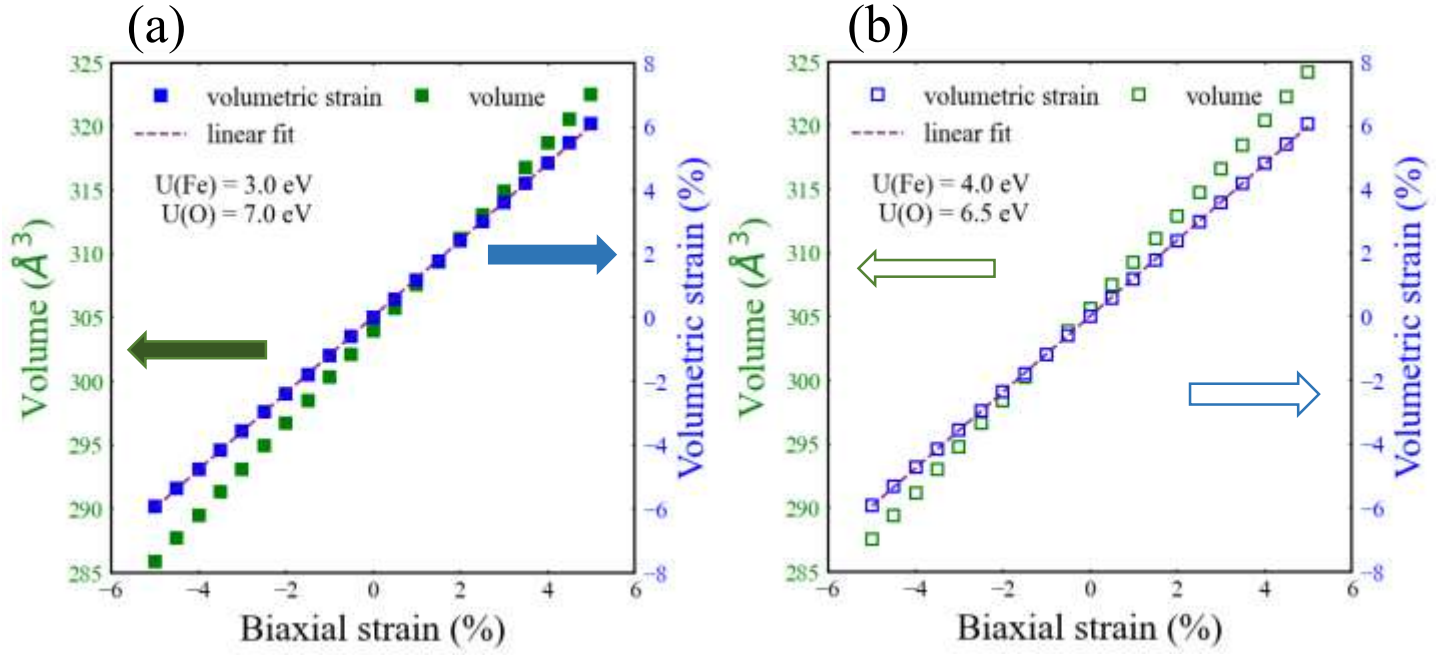


Figure 7. Effect of biaxial strain on volume. (a) represents the study using  $U(\text{Fe}) = 3.0 \text{ eV}$  on Fe and  $U(\text{O}) = 7.0 \text{ eV}$  on O, while (b) illustrates the study using  $U(\text{Fe}) = 4.0 \text{ eV}$  and  $U(\text{O}) = 6.5 \text{ eV}$ . The left vertical axis represents the volume as a function of biaxial strain, and the right vertical axis represents the plot of the volumetric strain per biaxial strain as a function of biaxial strain, which slope gives the volumetric strain per biaxial strain of 1.2.

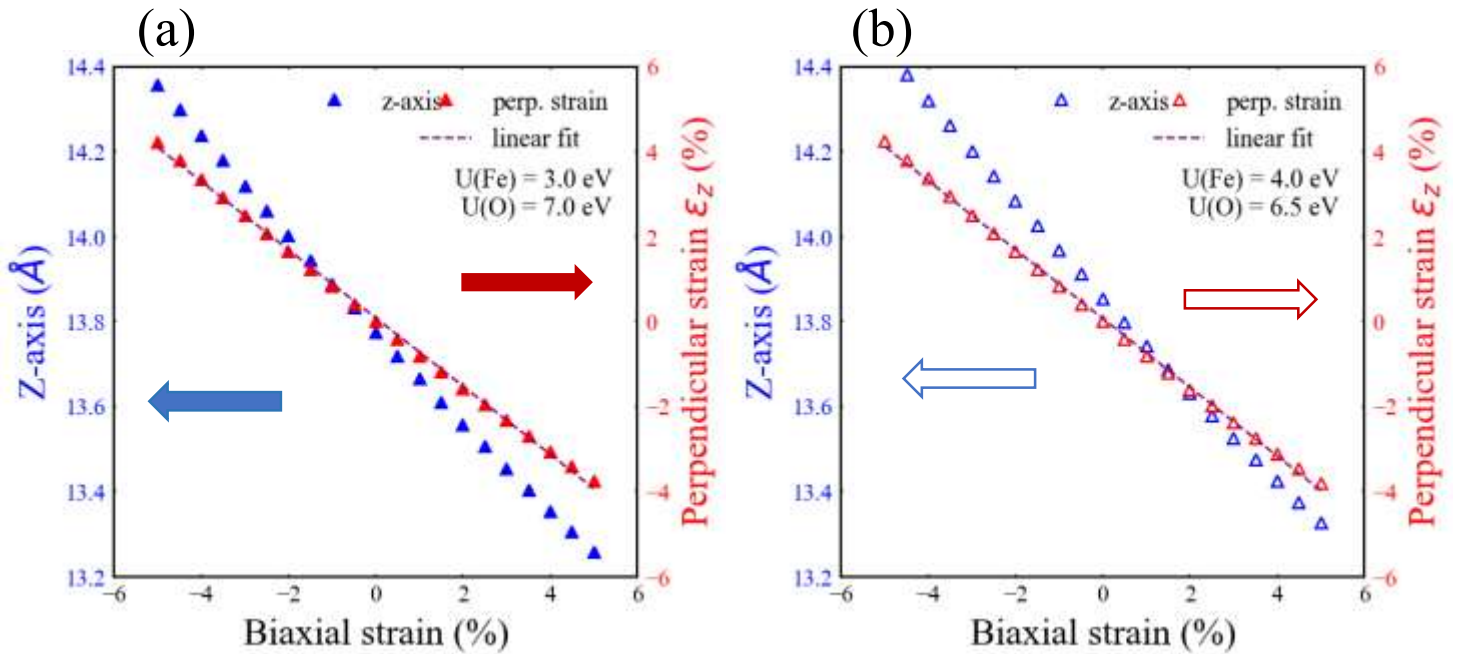




Figure 8. Effect of biaxial strain on the  $z$ -axis. (a) represents the first study using  $U(\text{Fe}) = 3.0 \text{ eV}$  on Fe and  $U(\text{O}) = 7.0 \text{ eV}$  on O, while (b) represents the second study using  $U(\text{Fe}) = 4.0 \text{ eV}$  and  $U(\text{O}) = 6.5 \text{ eV}$ . The left vertical axis represents the  $z$ -axis as a function of biaxial strain, and the right vertical axis represents the plot of the lateral strain as a function of biaxial strain, which slope gives the Poisson's ratio of 0.80.

#### 4.2 Effective mass of free charge carriers

We calculate the effective mass of charge carriers for the strained and unstrained of the perfect crystal of hematite using the primitive cell with the rhombohedral crystal structure in Figure 2 (a). In this case, the electrons at the conduction band minima (CBM) and holes at the valence band maxima (VBM) are considered. To begin the analysis, we examined the band structure of hematite along high-symmetry  $k$ -points in Figure 5 (b), as suggested by the Seek-path program<sup>105</sup> and ref<sup>106</sup> in the reciprocal space. Our findings reveal that hematite has an indirect bandgap<sup>99,100</sup>. Additionally, we observed that the curvature around the CBM is almost flat, while the curvature around the VBM is curved, consistent with previous theoretical and experimental studies<sup>99,107,108</sup>. This curvature difference indicates that the electron's effective mass is larger than that of the hole<sup>109</sup>.

We start with strain-free hematite. In Figure 9, we investigate the electronic properties of strain-free hematite using first-principles calculations. Specifically, we examine the effective masses of electrons and holes along the  $S_0|S_2 - F$  and  $H_2|H_0 - L$  high-symmetry directions, respectively. In the first study using Hubbard  $U$  value of  $U(\text{Fe}) = 3.0 \text{ eV}$  and  $U(\text{O}) = 7.0 \text{ eV}$ , our results reveal that the CBM has an effective electron mass of approximately  $4.41 m_0$  (where  $m_0$  represents the rest mass of an electron), while the VBM has an effective hole mass of around  $1.60 m_0$ . These findings support the prevailing notion that electrons are heavier than holes in pure hematite<sup>99,109</sup>. For the second study along the same high symmetry points, we obtained an electron effective mass of  $2.93 m_0$  and the hole effective mass of  $1.55 m_0$ , which is also consistent with the notion that electrons are heavier than holes in pure hematite<sup>99,109</sup>. Notably, our calculated effective masses fall within the typical range of  $0.01 m_0 - 10.0 m_0$ ,<sup>110</sup> for charge carriers in materials, lending confidence to our results.



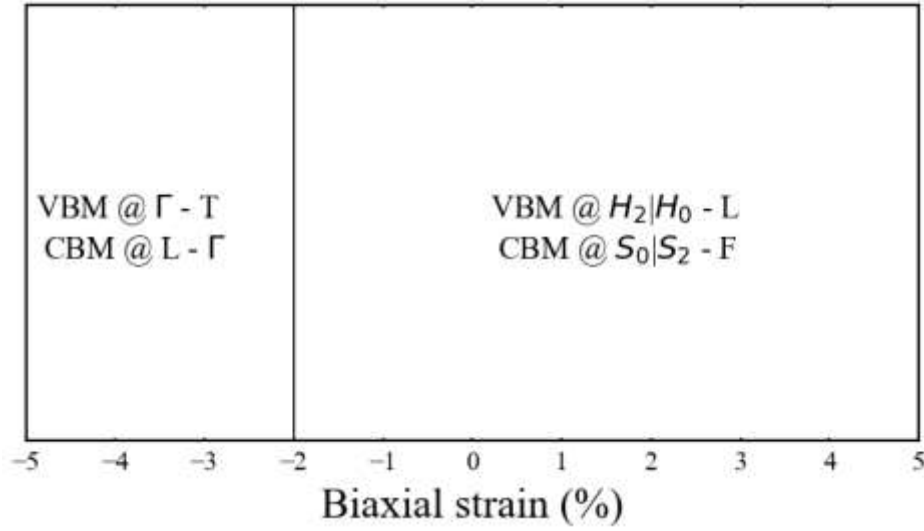


Figure 9. The high symmetry path in the reciprocal space used for the calculation of electron effective mass at the conduction band (CBM) minima and hole effective mass at the valence band maxima (VBM).

Numerous studies have investigated the effective mass of charge carriers in hematite through density functional theory (DFT) calculations. However, only one experimental work has reported the effective mass of charge carriers in hematite. Unfortunately, there is a wide range of reported values in the literature, as summarized in Table 1. Some studies have employed the density of states approach<sup>100,110</sup>, which tends to generally overestimate effective masses (reference 62). On the other hand, other studies have used the band structure approach<sup>111,112</sup>, but in most cases, they assumed parabolicity around the band extrema. As a result, effective mass values for electrons have been reported to range from  $1.5 m_0$ <sup>112</sup> to  $131.0 m_0$ <sup>113</sup>, while for holes, the effective mass was reported to be around  $2.1 m_0$ <sup>112</sup>. We believe that the wide scatter in the results is primarily due to simplifications introduced in computing the effective mass, rather than the choice of the DFT functional. This belief is supported by the fact that our values are in good agreement with the computational results obtained by Neufeld and Caspary<sup>109</sup>, despite our use of different DFT functionals. This agreement stems from our use of the band structure approach without assuming isotropic effective mass or a parabolic band structure near the extrema. In contrast, the only experimental effective mass of electrons reported by Bosman and Van Daal in 1970 was  $9.5 m_0$ <sup>114</sup>, which is higher than our estimations. However, we believe that this discrepancy is mainly due to temperature effects (experiments at 1000 K and DFT at 0 K), and partly due to the slight

doping level in the experiments ( $< 1\%$ ). It is worth noting that in two previous reports in the literature, holes were predicted to be heavier than electrons, contrary to our findings. Again, we believe that these prior conclusions are influenced by the use of the simple density of states approach to estimate the effective masses. Our detailed computation of these effective masses from the band structure with minimal assumptions is more robust. Therefore, we assert that free electrons in hematite are heavier than free holes. This conclusion aligns with the work of Neufeld and Caspary<sup>109</sup>, who employed similar detailed calculations, albeit with different DFT functionals.

This part will examine how mechanical strain impacts the effective masses of free electrons and holes. In [Figure 9](#), we observe that the direction along the high-symmetry k-points is the same as in the strain-free state, ranging from -2% compressive strain to +5% tensile strain for both free electrons and free holes. However, when the biaxial compressive strain state exceeds -2.0% strain, the electron effective mass and hole effective mass are calculated along the L –  $\Gamma$  and  $\Gamma$  – T high-symmetry directions, respectively. To further explore this phenomenon, we present the band structures of the material as a function of biaxial strain in Appendix 4.

In [Figure 10 \(a\)](#) using  $U(\text{Fe}) = 3.0$  eV and  $U(\text{O}) = 7.0$  eV, the free electron effective mass increases with compressive strain but decreases with tensile strain. In comparison, the free hole effective mass decreases in compression and increases in tension. This is also true when we change the Hubbard U values to  $U(\text{Fe}) = 4.0$  eV and  $U(\text{O}) = 6.5$  eV, presented in [Figure 10 \(b\)](#). This phenomenon was observed on a classical semiconductor, silicon, when strained bi-axially<sup>115</sup> and some other functional oxide material<sup>116</sup>. The explanation for this behavior lies in the curvature around the conduction band minimum (CBM) and the valence band maximum (VBM). When the material is compressed, the curvature around the CBM becomes flatter, resulting in an increased effective mass for free electrons. This is because the density of states for electrons near the energy level increases, causing the electrons to repel one another and increase their effective mass.

Conversely, the curvature around the CBM becomes more curved under tensile strain, leading to a decreased effective mass for free electrons. This behavior is consistent with the fact that compressing a material reduces inter-atomic distances, which in turn changes the energy level and electronic orbitals of the material<sup>117</sup>. This change in electronic structure is also responsible for the significant reduction in bandgap that occurs under compressive strain, as reported by ref <sup>118</sup>.

For free holes, the effective mass behaves oppositely, increasing in tension and decreasing in compression. As the material is compressed, the curvature around the VBM becomes more curved, leading to a decreased effective mass for holes. This is because the density of states for holes near the energy level becomes more dispersed, causing the effective mass to decrease. The opposite happens when the material is subjected to tensile strain. It is worth noting that mechanical strain can also change the ordering of band edges<sup>116,118</sup>. However, in the case of hematite, the material maintained its indirect bandgap ordering for all the strain cases studied. Our study provides valuable insights into the relationship between mechanical strain and the effective mass of free charge carriers in pure hematite, which has important implications for its potential applications in various fields, including photoelectrochemical water splitting.

**Table 1. The effective mass of charge carriers in pure hematite available in the literature**

Functional	DOS effective mass ( $m_0$ )		Band effective mass ( $m_0$ )	
	Electron effective mass	Hole effective mass	Electron effective mass	Hole effective mass
<b>PBE + U (this work) ( U(Fe) = 3.0 eV and U(O) = 7.0 eV) (this work)</b>	...	...	4.4	1.6
<b>PBE + U (this work) ( U(Fe) = 4.0 eV and U(O) = 6.5 eV) (this work)</b>	---	---	2.9	1.5
<b>PBE</b> [ <sup>109</sup> ]	14.4	7.9	7.7	1.6
<b>PBE + U ( U (Fe) = 4.3 eV)</b> [ <sup>109</sup> ]	14.4	9.7	4.0	1.5
<b>HSE06</b> [ <sup>109</sup> ]	13.6	9.0	4.6	1.5
<b>G0W0</b> [ <sup>109</sup> ]	16.0	8.7	5.8	1.5
<b>PBE + U (U(Fe) = 4.0 eV)</b> [ <sup>113</sup> ]	...	...	131.0 <sup>a</sup>	...
<b>PW91 + U (U(Fe) = 6 eV)</b> [ <sup>110</sup> ]	...	...	8.6 – 16.1 <sup>b</sup>	...
<b>PBE + U (U(Fe) = 4.0 eV)</b> [ <sup>100</sup> ]	1.6	2.2	...	...

<b>G<sub>0</sub>W<sub>0</sub> (U(Fe) = 3.0 eV) [<sup>112</sup>]</b>	1.5 <sup>c</sup>	2.1 <sup>c</sup>	...	...
<b>Experiment [<sup>114</sup>]</b>	...	...	9.5 <sup>d</sup>	...

(a) Authors assumed parabolic band structure and isotropic effective mass tensor.

(b) Values are in different crystallographic planes but still using a simple parabolic approximation.

(c) DOS approach weighted by a Boltzmann factor to account for anisotropy and non-parabolicity.

(d) Estimated from electric resistivity measurement at high temperature at 1000 K.

In addition to its effect on effective mass, mechanical strain can also have a significant impact on the mobility of charge carriers in a semiconductor material. Specifically, it is well-known that mobility is inversely related to effective mass<sup>114,119</sup>, meaning that as the effective mass of a charge carrier increases, its mobility decreases, and vice versa. In the case of biaxial compressive strain, the effective mass of electrons in a material tends to increase, leading to a corresponding decrease in their mobility. Conversely, the effective mass of holes tends to decrease under compressive strain, resulting in an increase in their mobility. This is particularly advantageous in the case of hematite, where slower hole mobility is a major challenge in photoelectrochemical water splitting applications<sup>120</sup>. By increasing the mobility of holes in hematite through the application of compressive strain, the material's conductivity can be improved, and its photocatalytic activities enhanced<sup>120</sup>. This is because slower-moving holes can act as recombination centers for electrons, hindering their movement and reducing the overall efficiency of the material. Therefore, the ability to control the mobility of charge carriers through mechanical strain is a valuable tool for optimizing the performance of semiconductor materials in a range of applications, including photoelectrochemical water splitting.

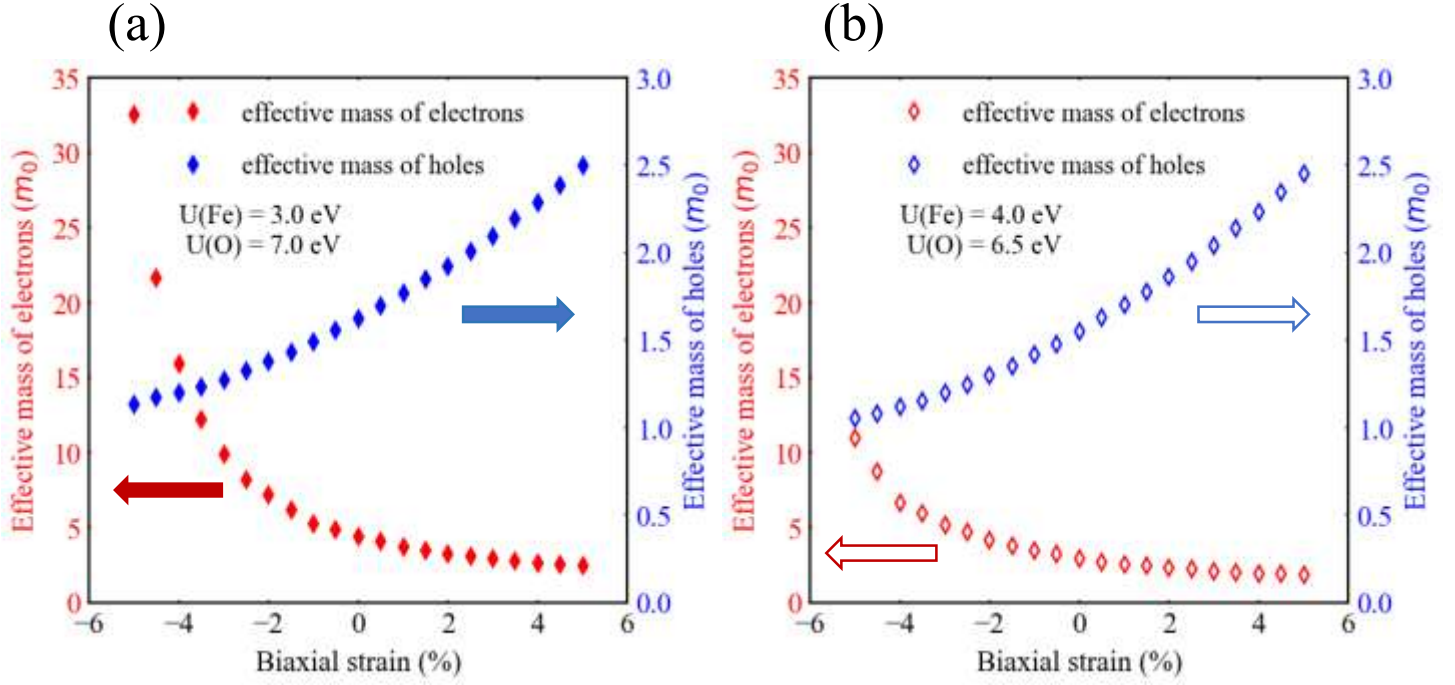


Figure 10. Effect of mechanical strain on the effective mass of charge carriers in hematite. (a) shows the effective mass of free electrons and holes using  $U(\text{Fe}) = 3.0 \text{ eV}$  and  $U(\text{O}) = 7.0 \text{ eV}$ . (b) represents the effective masses employing  $U(\text{Fe}) = 4.0 \text{ eV}$  and  $U(\text{O}) = 6.5 \text{ eV}$ . In both plots, the left vertical axis (in blue) represents the effective mass of electrons while the right vertical axis (in red) represents the hole effective masses as a function of strain. It is important to note that the effective masses are normalized to the mass of an electron,  $9.11 \times 10^{-31} \text{ kg}$ .

### 4.3 Polarons in hematite

The behavior of electrons in a perfect crystal is well-described by periodic wave functions, but in reality, natural crystals contain defects that disrupt this periodicity<sup>51</sup>. These defects give rise to localized states known as polarons, which are quasiparticles that arise from interactions between carriers and phonons. One of the key characteristics of polarons is that they have electrostatic forces that can cause them to alter the crystal structure of the material they are found in. For instance, if an electron is trapped in a polaron, it will attract ions with a net positive charge, leading to changes in the arrangement of atoms in the crystal. The same is true for polar semiconductors and transition metal oxides, including hematite, which are particularly favorable environments for the formation of localized states<sup>44</sup>. Understanding the behavior of polarons is crucial for a range

of applications, from developing new materials for electronics to improving our understanding of the properties of natural crystals.

The interaction between excess charge carriers and ions can be categorized as either weak or strong interactions, resulting in the formation of two types of polarons: large polarons (or free carriers) and small polarons<sup>54</sup>. Large polarons, also known as free carriers, are characterized by a delocalized wavefunction that spans a significant number of atoms. In contrast, small polarons have a localized wavefunction that is confined to a single atom. Experimental and theoretical investigations have confirmed the presence of both small and large polarons in hematite, with small polarons being ten times more significant in magnitude than large polarons<sup>24,48,55</sup>. These findings are illustrated in [Figure 11](#), where panels (c) and (d) demonstrate the delocalized wavefunction of large polarons, while panels (a) and (b) depict the localized wavefunction of small polarons. In the study of hematite, it has been observed that the formation of small polarons - both hole and electron - can result in the creation of deep-state energy levels within the bandgap of the material. These energy levels act as trapping sites for free charge carriers, leading to recombination<sup>44</sup>. The energy level in question is related to either the valence band maxima (VBM) or conduction band minima (CBM), depending on whether the small polaron is a hole or an electron.

In [Figure 12](#), we define a quantity,  $\Delta E$ , which is the energy difference between the center of the small polaron energy level in the bandgap to either CBM or VBM. This energy level describes the ionization energy required to fully ionize the polaron into the CBM or the VBM. Also, this energy level is of great interest in the optimization of a photoelectrochemical (PEC) process, as it provides insight into the effect of defect levels on the conversion process<sup>44,121</sup>. Understanding the behavior of small polarons and their associated energy levels can therefore be crucial in the development of more efficient and effective PEC systems.

Starting with zero strained hematite, when a small polaron electron localizes on the Fe (III) state, it reduces it to Fe (II) and causes a distortion<sup>122</sup> around the Fe carrying the polaron. This distortion results in a reduction of the Fe-O bond length from an initial length of 2.11 Å to 1.98 Å, which is consistent with literature<sup>121</sup>. On the other hand, when a small polaron hole localizes on the O (II) state, it reduces it to O (I) state. The localization of small polarons also creates an energy

level within the bandgap. In the case of the small polaron electron, this energy level, shown in [Figure 12 \(a\)](#), is approximately 0.5 eV below the CBM, which is in agreement with previous literature<sup>44,121</sup>. This energy level decreases the optical bandgap of the material, resulting in an effective bandgap of 1.9 eV. However, in the case of the small polaron hole, the energy level in [Figure 12 \(b\)](#) is about 2.0 eV relative to the VBM. This energy level is above the Fermi energy level in the material and is an empty state. As a result, it traps any moving photo-excited electron in the material, leading to the unwanted recombination of charge carriers in hematite. This is one of the major reasons why hematite exhibits low photo-conversion efficiency<sup>120</sup>.

Then, we determine the self-trapping energy ( $E_{self-trapping}$ ) using [equation 7](#)<sup>25,123</sup>. It's worth noting that the  $E_{self-trapping}$  represents the energy required to trap a charge carrier in a material, assuming that the volume remains constant. This energy also takes into account the electrostatic interaction between the charge carrier and the surrounding atoms, but it does not account for any changes in volume or pressure that may occur during the trapping process. Our calculations yielded a  $E_{self-trapping}$  of 0.11 eV and 0.24 eV for small electron polarons and small hole polarons, respectively. This is consistent with previous research published in literature<sup>24</sup>.

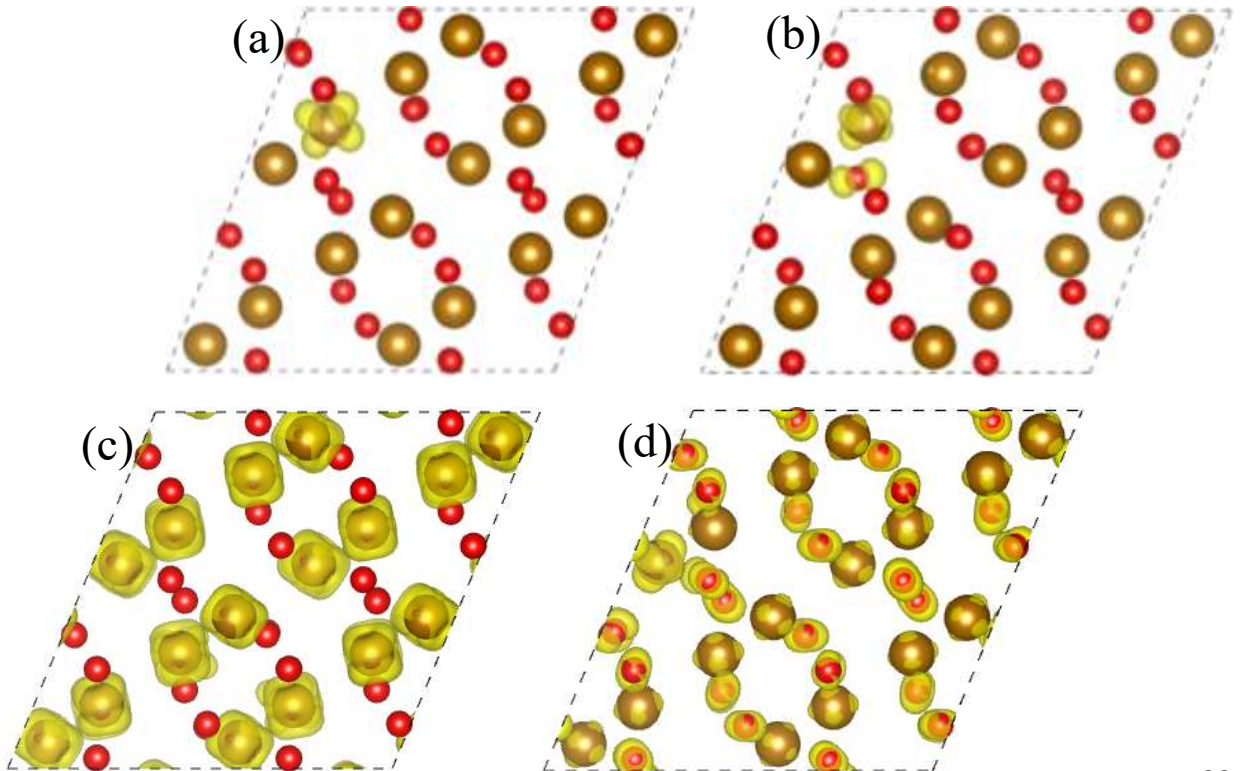




Figure 11. Visualization of Charge density isosurface shown in yellow (a) small polaron electron localizing on Fe atom, (b) small polaron hole localizing on O atoms, (c) large polaron electron (free electron) delocalized on Fe atoms, and (d) large polaron hole (free hole) delocalize on O atoms. The isosurface level for the small polarons was maintained at  $0.019 \text{ e}/\text{\AA}^3$ , while for the free carriers, the isosurface is maintained at  $0.02 \text{ e}/\text{\AA}^3$ . Gold (large) and red (small) represents Fe and O atoms, respectively. These images are generated using VESTA visualization software package

Next, we study the effect of biaxial mechanical strain on the  $E_{\text{self-trapping}}$ . In Figure 13, using the explanation on  $\text{SrTiO}_3$ <sup>25</sup>, we predict that the majority electronic defect under biaxial tensile strain is the small polaron electrons and holes. In the scenario of biaxial tensile strain, a small polaron cell can attain a positive net energy gain in the a and b directions without incurring any unfavorable energy outcomes that may arise from uncontrolled relaxation in the c-direction. This phenomenon facilitates the stabilization of the small polaron under biaxial tensile strain, thereby resulting in a reduction of the transition pressure.

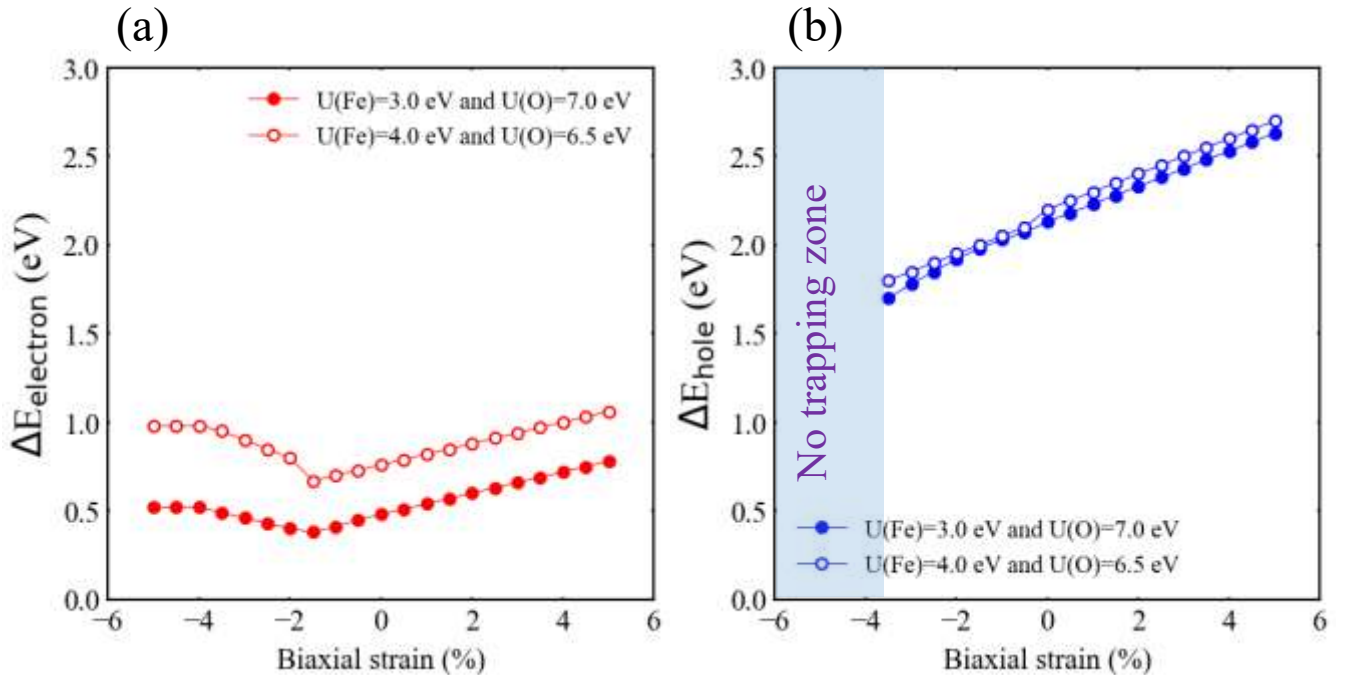


Figure 12. Small polarons energy level in the bandgap of hematite as a function of biaxial strain. It is worth noting that  $\Delta E$  in eV is the energy difference between the center of the polaron energy peak to the edge of either the valence band maximum (polaron hole) or conduction band minimum



(polaron electron). (a) small polaron electron energy level in eV as a function of biaxial strain (b) small polaron hole energy level in eV as a function of biaxial strain. In both plots, the energy levels increase in the tensile strain state favoring small polaron formation in the material.

In the compressive biaxial strain, the  $E_{self-trapping}$  shows a different pattern in the case of electron and hole polaron compared, as they exhibit an opposite trend. In Figure 13 (a), we observe that the mechanical strain does not favor the formation of large fast polaron electrons (or free electrons) in hematite. However, we observe from the total density of states (TDOS) plot presented in Appendix 5 that, when the compressive strain is increased from -2% to -5%, we observed a shift in the distortion<sup>122</sup> peak to forming an intra-bandgap peak in the valence band. In addition, we also observe, in Figure 12 (a), the polaron energy peak in the bandgap transitioning to higher energy values in relation to the CBM<sup>44,121</sup>. These findings suggest that while a mechanical strain is not sufficient to alter the energy landscape in favor of large fast polaron electrons (or free electrons), it can decrease the  $E_{self-trapping}$  of the small polaron electron. Therefore, the reduction in volume caused by mechanical compressive strain can facilitate the movement of small polaron electrons, but it does not favor the formation of large fast polaron electrons (or free carriers) in hematite.

According to Figure 13 (b), we have determined the value of  $E_{self-trapping}$  for the holes. Our calculations show that at compressive strains ranging from -0.5% to 2.5%, small polaron holes are the dominant charge carriers in the material. However, when the compressive strain exceeds -3.0%, the majority of charge carriers in hematite turn into large polaron holes (or free holes), consistent with the study conducted on electrons in SrTiO<sub>3</sub><sup>25</sup>. This suggests that when the biaxial strain reaches a certain magnitude, free holes become the primary charge carriers in hematite. It is noteworthy that hematite has a volumetric strain per biaxial strain of 1.2, as discussed in section 3.1. This information implies that the material is inclined to maintain its defective structure with small slow polarons. Therefore, it is not surprising that we need to apply a high magnitude of strain to alter the energy landscape in favor of large polaron holes in the material.

Notably, at a compressive strain of -3.5%, a trade-off exists between the abundance of free holes and free electrons in the material, which calls for an optimum biaxial compressive strain.

This phenomenon has been discussed in section 3.2, where it has been observed that compressive strain causes an increase in the effective mass of free electrons. This increase is particularly significant at -3.5% compressive strain. As a result, the mobility of free electrons in the material becomes lower since heavier particles are less mobile. On the other hand, the effective mass of free holes decreases at this strain, making them faster. However, this change in the effective mass of carriers may have an impact on the overall conductivity of the material, which is believed to depend on both electrons and holes.

To further investigate the effects of biaxial mechanical strain on the energy landscape of the material, we conducted a study where we change the magnitude of the Hubbard  $U$  value on Fe and O to 4.0 eV and 6.5 eV, respectively, based on the recommendations in reference<sup>23</sup>. We then calculate  $E_{self-trapping}$  as a function of the strain. It turns out that, even with the increased Hubbard  $U$  values on Fe, we did not observe a significant alteration of the energy landscape in favor of large polaron electrons (or free electrons), presented in [Figure 13 \(a\)](#). Nevertheless, we acknowledge that Hubbard  $U(Fe) = 4.0$  eV increases the localization of small polaron electrons in the material and the local distortions caused by the small polaron electrons localization. We also investigate the effects of Hubbard  $U(O) = 6.5$  eV on small polaron holes, as shown in [Figure 13 \(b\)](#), and observed the same trend as with  $U$  values of 7.0 eV on O. This implies that Hubbard  $U$  value on O does not change the response of the small polaron holes to the mechanical strain. Also, from these results, we confirm that altering the energy landscape in favor of large polarons (or free carriers) is not solely a function of the Hubbard  $U$  value but is also determined by the material's intrinsic properties.

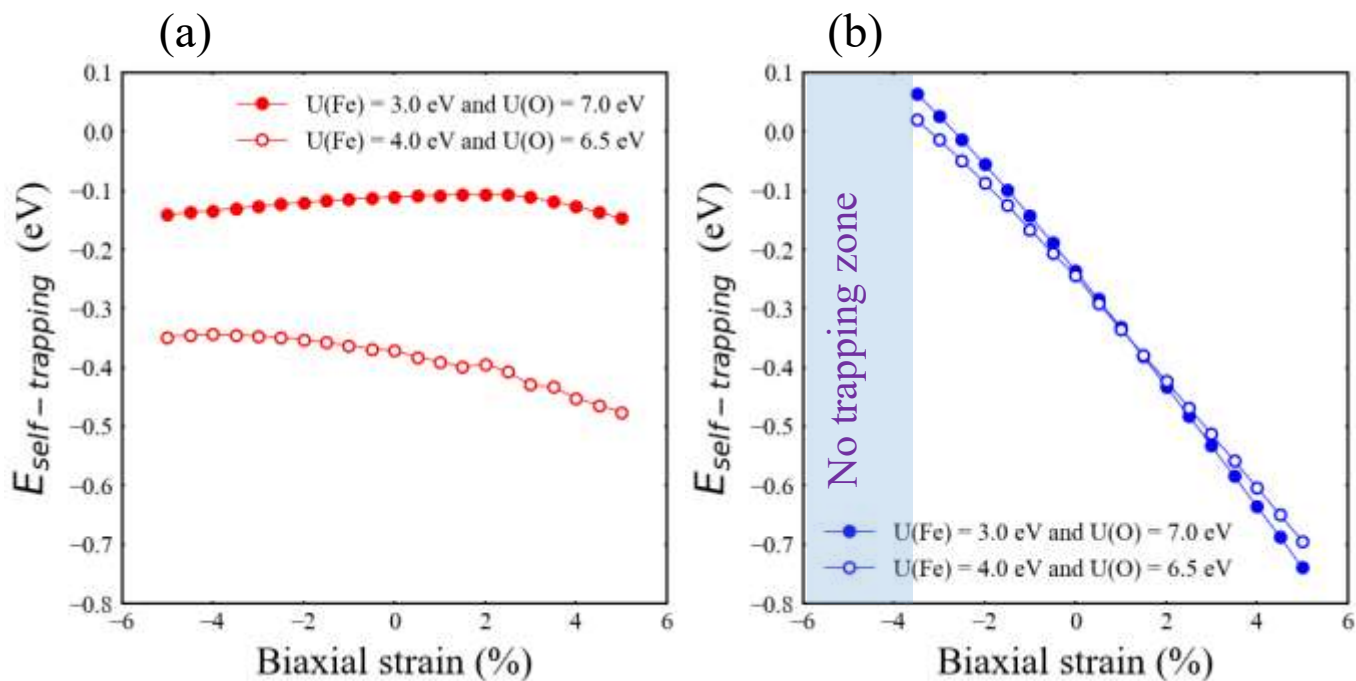


Figure 13. The predominance charge defect in hematite based on  $E_{\text{self-trapping}}$  as a function of the mechanical strain using (a) the  $E_{\text{self-trapping}}$  in eV indicating the predominant defects to be small polaron electrons for all strain conditions. The filled circles (in red) represent the case with  $U(\text{Fe}) = 3.0$  eV and  $U(\text{O}) = 7.0$  eV, while the unfilled circles (white color) represent the case of  $U(\text{Fe}) = 4.0$  eV and  $U(\text{O}) = 6.5$  eV (b) the  $E_{\text{self-trapping}}$  indicating the predominant defects to be free holes at strains above -3.5% compressive strain. The filled circles (green color) represent the case with  $U(\text{Fe}) = 3.0$  eV and  $U(\text{O}) = 7.0$  eV, while the unfilled circles (white color) represent the case of  $U(\text{Fe}) = 4.0$  eV and  $U(\text{O}) = 6.5$  eV.

#### 4.4 Implications to photoelectrochemical water splitting

Our research focuses on addressing key challenges in photocatalysis, specifically the generation, separation, and extraction of reactive charges in an efficient manner<sup>35</sup>. The effective management of these charges is crucial for driving chemical reactions and achieving desirable outcomes. In this context, our study investigates the influence of mechanical strain on the electronic conductivity of hematite, with significant implications for its application as a material for hydrogen generation in photoelectrochemical cells.

Firstly, our findings indicate that hematite, despite its comparatively low electronic conductivity compared to other photoanode materials, exhibits a promising response to bandgap

reduction, particularly under biaxial compressive strain. This reduction in bandgap holds the potential to enhance the performance of hematite as a photoanode material. Specifically, the reduction in the bandgap of hematite can have a significant effect on both the oxygen evolution reaction and the hydrogen evolution reaction<sup>124</sup>. The reduction in bandgap leads to a decreased energy requirement for electron-hole pair creation in the photoanode.<sup>124</sup> As a result, more energetic holes are available for the oxygen evolution reaction (OER), which is the process of oxidizing water to produce oxygen gas.<sup>124</sup> This means that the reduction in bandgap will typically results in more thermodynamically favorable condition for the OER.

Secondly, we have observed that hematite possesses a high poisson's ratio of 0.8 and volumetric strain per biaxial strain of 1.2, indicating no significant change in volume. These mechanical properties are advantageous for the design of photoelectrochemical cells, where the photoanode material must endure mechanical stress while maintaining flexibility.

Furthermore, our study reveals an intriguing trade-off between the abundance of free holes and free electrons within hematite at a compressive strain of  $-3.5\%$ . Notably, the energy landscape favors the presence of large polaron holes (or free holes) under this specific strain but does not have a similar effect on small polaron electrons. This highlights the importance of identifying an optimal magnitude of mechanical strain that promotes the presence of free carriers and small polarons in hematite since they both co-exist. Based on our findings, we propose a compressive strain of  $-2\%$  as the ideal magnitude. This specific biaxial strain magnitude enhances the mobility of free carriers while reducing the distortion energy of small polaron electrons, consequently increasing the material's activity.

Lastly, our research offers valuable insights into modulating the electronic conductivity of hematite beyond 0 K density functional theory calculations. This knowledge opens up possibilities for leveraging hematite as a photocatalyst for hydrogen production, effectively addressing the rising energy demand and mitigating the adverse impacts of climate change.

# Chapter 5

## Conclusion and Future Work

### 5.1 Conclusion

In this work, we did first principle calculations using density functional theory approximation to understand the effect of mechanical strain on controlling the electronic conductivity in pure and polaronic  $\alpha$ -Fe<sub>2</sub>O<sub>3</sub> (hematite). Our analysis revealed that the zero-strain state of hematite possesses an indirect electronic bandgap of approximately 2.4 eV, which is in line with previous literature<sup>24,32</sup>. We also observed a reduction in the bandgap under both tensile and compressive strain, with the compressive strain state resulting in a more significant reduction. Additionally, we determined that pure hematite has a poisson's ratio ( $\nu$ ) of 0.80, and a volumetric strain per biaxial strain of 1.2, indicating a non-significant overall volumetric changes under biaxial strain.

After investigating the impact of strain on the bandgap of pure hematite, we proceeded to study the effect of strain on the effective mass of free charge carriers, namely electrons, and holes. There are two methods for calculating the effective mass of these carriers: the density of states and band curvature approaches. For our purposes, we used the band curvature method to determine the effective mass of free electrons and holes in hematite. Since the effective mass of charges carriers in solid-state materials typically ranges from  $0.01 m_0$  to  $10.0 m_0$ ,<sup>110</sup> our calculations using the band curvature approach indicated that the CBM of hematite has an effective electron mass of  $4.4 m_0$  (where  $m_0$  represents the mass of an electron), while the VBM has an effective hole mass of around  $1.6 m_0$  at zero strain, using Hubbard  $U(\text{Fe}) = 3.0$  eV and  $U(\text{O}) = 7.0$  eV. For the second study, using Hubbard  $U$  values of  $U(\text{Fe}) = 4.0$  eV and  $U(\text{O}) = 6.5$  eV, we obtain an electron effective mass of  $2.93 m_0$  and hole effective mass of  $1.55 m_0$ . All our calculated values are consistent with the notion that electrons are heavier than holes in pure hematite<sup>109</sup>. Next, we examined the effect of the biaxial strain on the effective mass of free charge carriers, specifically free electrons and free holes. Our results showed that the effective mass of free electrons decreases under tensile strain and increases under compressive strain, while the effective mass of free holes exhibits the opposite trend under both tensile and compressive strain.

In our final investigation, we examined the impact of strain on the polarons in hematite, specifically small polarons for electrons and holes, as well as large polarons for free electrons and free holes. We calculated the self-trapping energy, which represents the energy difference between the structure with a localized state (small polarons) and the delocalized state (large polarons or free carriers). Our findings indicate that biaxial strain does not significantly alter the energy landscape in favor of large electron polarons (or free electrons) in hematite but can decrease the self-trapping energy of the small polaron electrons. However, we did observe that mechanical strain can influence the energy landscape to favor large hole polarons (or free holes) in the material, particularly at strains above -3.5% compressive strain, where large polaron holes (free holes) become the majority of charge carriers. We believe that the low photo-conversion efficiency in hematite is primarily due to small slow polaron holes. Therefore, modifying the energy landscape via mechanical strain to favor large polaron holes (or free holes) could enhance the material's activity and improve its efficiency as a photocatalyst. In addition to our investigation of the effect of mechanical strain on the electronic conductivity of hematite, we also tested the sensitivity of our findings to different Hubbard  $U$  values. Specifically, we used  $U(\text{Fe}) = 4.0$  eV and  $U(\text{O}) = 6.5$  eV, and found that these values did not significantly alter our results and in fact the qualitative trends remain unchanged. This indicates that our findings are robust and reliable.

In summary, our study provides valuable insights into modulating the electronic conductivity of hematite beyond 0 K density functional theory, which could facilitate its use as a photocatalyst for hydrogen production to address the growing energy demand and mitigate the impact of climate change.

## **5.2 Future Work**

The challenge in photocatalysis is to generate, separate, and extract reactive charges effectively. This requires the production of long-lived, energetically favorable charge carriers to drive chemical reactions. In the future, research on the effect of mechanical strain on hematite will focus on optimizing the material for use in photocatalytic applications. This will involve investigating the impact of mechanical strain on the activation barrier for hopping and the mobility of the small polarons. These efforts will serve as a guidance to experimental study and lead to the development of more efficient and sustainable photocatalytic systems that utilize strained hematite.

# References

- 1 Electricity Market Report - Jan 2022, 2022, 118.
- 2 S. Fawzy, A. I. Osman, J. Doran and D. W. Rooney, Strategies for mitigation of climate change: a review, *Environ. Chem. Lett.*, 2020, **18**, 2069–2094.
- 3 A. Qazi, F. Hussain, N. ABD. Rahim, G. Hardaker, D. Alghazzawi, K. Shaban and K. Haruna, Towards Sustainable Energy: A Systematic Review of Renewable Energy Sources, Technologies, and Public Opinions, *IEEE Access*, 2019, **7**, 63837–63851.
- 4 Light, water, hydrogen: the solar generation of hydrogen by water photoelectrolysis, *Choice Rev. Online*, 2008, **45**, 45-6194-45–6194.
- 5 L. Kaiwen, Y. Bin and Z. Tao, Economic analysis of hydrogen production from steam reforming process: A literature review, *Energy Sources Part B Econ. Plan. Policy*, 2018, **13**, 109–115.
- 6 S. Shiva Kumar and V. Himabindu, Hydrogen production by PEM water electrolysis – A review, *Mater. Sci. Energy Technol.*, 2019, **2**, 442–454.
- 7 I. S. Cho, C. H. Lee, Y. Feng, M. Logar, P. M. Rao, L. Cai, D. R. Kim, R. Sinclair and X. Zheng, Codoping titanium dioxide nanowires with tungsten and carbon for enhanced photoelectrochemical performance, *Nat. Commun.*, 2013, **4**, 1723.
- 8 H. S. Han, S. Shin, D. H. Kim, I. J. Park, J. S. Kim, P.-S. Huang, J.-K. Lee, I. S. Cho and X. Zheng, Boosting the solar water oxidation performance of a BiVO<sub>4</sub> photoanode by crystallographic orientation control, *Energy Environ. Sci.*, 2018, **11**, 1299–1306.
- 9 D. K. Lee and K.-S. Choi, Enhancing long-term photostability of BiVO<sub>4</sub> photoanodes for solar water splitting by tuning electrolyte composition, *Nat. Energy*, 2018, **3**, 53–60.
- 10 T. W. Kim, Y. Ping, G. A. Galli and K.-S. Choi, Simultaneous enhancements in photon absorption and charge transport of bismuth vanadate photoanodes for solar water splitting, *Nat. Commun.*, 2015, **6**, 8769.
- 11 Y. Xu, Q. Zhao, C. Du, C. Zhou, C. Zhou, H. Xue and S. Yang, in *Photoelectrochemical Solar Cells*, John Wiley & Sons, Ltd, 2018, pp. 121–157.
- 12 J. H. Kim, J.-W. Jang, Y. H. Jo, F. F. Abdi, Y. H. Lee, R. van de Krol and J. S. Lee, Hetero-type dual photoanodes for unbiased solar water splitting with extended light harvesting, *Nat. Commun.*, 2016, **7**, 13380.
- 13 Z. Najaf, D. L. T. Nguyen, S. Y. Chae, O.-S. Joo, A. U. H. A. Shah, D.-V. N. Vo, V.-H. Nguyen, Q. V. Le and G. Rahman, Recent trends in development of hematite ( $\alpha$ -Fe<sub>2</sub>O<sub>3</sub>) as an efficient photoanode for enhancement of photoelectrochemical hydrogen production by solar water splitting, *Int. J. Hydrog. Energy*, 2021, **46**, 23334–23357.
- 14 P. Sharma, J. Jang and J. S. Lee, Key Strategies to Advance the Photoelectrochemical Water Splitting Performance of  $\alpha$ -Fe<sub>2</sub>O<sub>3</sub> Photoanode, *ChemCatChem*, 2019, **11**, 157–179.
- 15 Z. Najaf, D. L. T. Nguyen, S. Y. Chae, O.-S. Joo, A. U. H. A. Shah, D.-V. N. Vo, V.-H. Nguyen, Q. V. Le and G. Rahman, Recent trends in development of hematite ( $\alpha$ -Fe<sub>2</sub>O<sub>3</sub>) as an efficient photoanode for enhancement of photoelectrochemical hydrogen production by solar water splitting, *Int. J. Hydrog. Energy*, 2021, **46**, 23334–23357.
- 16 K. Sivula, F. Le Formal and M. Grätzel, Solar Water Splitting: Progress Using Hematite ( $\alpha$ -Fe<sub>2</sub>O<sub>3</sub>) Photoelectrodes, *ChemSusChem*, 2011, **4**, 432–449.
- 17 K. Maabong, A. G. J. Machatine, B. S. Mwankemwa, A. Braun, D. K. Bora, R. Toth and M. Diale, Nanostructured hematite thin films for photoelectrochemical water splitting, *Phys. B Condens. Matter*, 2018, **535**, 67–71.

- 18 K. Maabong, A. G. J. Machatine, B. S. Mwankemwa, A. Braun, D. K. Bora, R. Toth and M. Diale, Nanostructured hematite thin films for photoelectrochemical water splitting, *Phys. B Condens. Matter*, 2018, **535**, 67–71.
- 19 M. Li, Y. Yang, Y. Ling, W. Qiu, F. Wang, T. Liu, Y. Song, X. Liu, P. Fang, Y. Tong and Y. Li, Morphology and Doping Engineering of Sn-Doped Hematite Nanowire Photoanodes, *Nano Lett.*, 2017, **17**, 2490–2495.
- 20 M. Allieta, M. Marelli, F. Malara, C. L. Bianchi, S. Santangelo, C. Triolo, S. Patane, A. M. Ferretti, Š. Kment, A. Ponti and A. Naldoni, Shaped-controlled silicon-doped hematite nanostructures for enhanced PEC water splitting, *Catal. Today*, 2019, **328**, 43–49.
- 21 K.-H. Ye, Z. Wang, H. Li, Y. Yuan, Y. Huang and W. Mai, A novel CoOOH/(Ti, C)-Fe<sub>2</sub>O<sub>3</sub> nanorod photoanode for photoelectrochemical water splitting, *Sci. China Mater.*, 2018, **61**, 887–894.
- 22 K. Sivula, F. Le Formal and M. Grätzel, Solar Water Splitting: Progress Using Hematite ( $\alpha$ -Fe<sub>2</sub>O<sub>3</sub>) Photoelectrodes, *ChemSusChem*, 2011, **4**, 432–449.
- 23 S. Shousha, S. Khalil and M. Youssef, A complete *ab initio* thermodynamic and kinetic catalogue of the defect chemistry of hematite  $\alpha$ -Fe<sub>2</sub>O<sub>3</sub>, its cation diffusion, and sample donor dopants, *Phys. Chem. Chem. Phys.*, 2021, **23**, 25518–25532.
- 24 S. Shousha, S. Khalil and M. Youssef, A complete *ab initio* thermodynamic and kinetic catalogue of the defect chemistry of hematite  $\alpha$ -Fe<sub>2</sub>O<sub>3</sub>, its cation diffusion, and sample donor dopants, *Phys. Chem. Chem. Phys.*, 2021, **23**, 25518–25532.
- 25 Y.-T. Chi, M. Youssef, L. Sun, K. J. Van Vliet and B. Yildiz, Accessible switching of electronic defect type in SrTiO<sub>3</sub> via biaxial strain, *Phys. Rev. Mater.*, 2018, **2**, 055801.
- 26 P. Wu, X. Ma, Y. Li, C.-B. Eom, D. G. Schlom, V. Gopalan and L.-Q. Chen, Influence of interfacial coherency on ferroelectric switching of superlattice BaTiO<sub>3</sub>/SrTiO<sub>3</sub>, *Appl. Phys. Lett.*, 2015, **107**, 122906.
- 27 N. A. Pertsev, A. K. Tagantsev and N. Setter, Phase transitions and strain-induced ferroelectricity in  $\{\mathrm{SrTiO}\}_3$  epitaxial thin films, *Phys. Rev. B*, 2000, **61**, R825–R829.
- 28 J. H. Haeni, P. Irvin, W. Chang, R. Uecker, P. Reiche, Y. L. Li, S. Choudhury, W. Tian, M. E. Hawley, B. Craigo, A. K. Tagantsev, X. Q. Pan, S. K. Streiffer, L. Q. Chen, S. W. Kirchoefer, J. Levy and D. G. Schlom, Room-temperature ferroelectricity in strained SrTiO<sub>3</sub>, *Nature*, 2004, **430**, 758–761.
- 29 S. Akbulatov, Y. Tian and R. Boulatov, Force–Reactivity Property of a Single Monomer Is Sufficient To Predict the Micromechanical Behavior of Its Polymer, *J. Am. Chem. Soc.*, 2012, **134**, 7620–7623.
- 30 S. L. Craig, A tour of force, *Nature*, 2012, **487**, 176–177.
- 31 Z. D. Pozun and G. Henkelman, Hybrid density functional theory band structure engineering in hematite, *J. Chem. Phys.*, 2011, **134**, 224706.
- 32 H. El-Gibally, S. Shousha, N. K. Allam and M. Youssef, Maximizing the electronic charge carriers in donor-doped hematite under oxygen-rich conditions via doping and co-doping strategies revealed by density functional theory calculations, *J. Appl. Phys.*, 2022, **131**, 155705.
- 33 A. J. Bosman and H. J. van Daal, Small-polaron versus band conduction in some transition-metal oxides, *Adv. Phys.*, 1970, **19**, 1–117.
- 34 N. Adelstein, J. B. Neaton, M. Asta and L. C. De Jonghe, Density functional theory based calculation of small-polaron mobility in hematite, *Phys. Rev. B*, 2014, **89**, 245115.



- 35 Z. Najaf, D. L. T. Nguyen, S. Y. Chae, O.-S. Joo, A. U. H. A. Shah, D.-V. N. Vo, V.-H. Nguyen, Q. V. Le and G. Rahman, Recent trends in development of hematite ( $\alpha$ -Fe<sub>2</sub>O<sub>3</sub>) as an efficient photoanode for enhancement of photoelectrochemical hydrogen production by solar water splitting, *Int. J. Hydrog. Energy*, 2021, **46**, 23334–23357.
- 36 B. Iandolo, B. Wickman, I. Zorić and A. Hellman, The rise of hematite: origin and strategies to reduce the high onset potential for the oxygen evolution reaction, *J. Mater. Chem. A*, 2015, **3**, 16896–16912.
- 37 A. G. Tamirat, J. Rick, A. A. Dubale, W.-N. Su and B.-J. Hwang, Using hematite for photoelectrochemical water splitting: A review of current progress and challenges, *Nanoscale Horiz.*, 2016, **1**, 243–267.
- 38 V. R. Satsangi, S. Kumari, A. P. Singh, R. Shrivastav and S. Dass, Nanostructured hematite for photoelectrochemical generation of hydrogen, *Int. J. Hydrog. Energy*, 2008, **33**, 312–318.
- 39 D. K. Zhong, J. Sun, H. Inumaru and D. R. Gamelin, Solar Water Oxidation by Composite Catalyst/ $\alpha$ -Fe<sub>2</sub>O<sub>3</sub> Photoanodes, *J. Am. Chem. Soc.*, 2009, **131**, 6086–6087.
- 40 K. Momma and F. Izumi, VESTA 3 for three-dimensional visualization of crystal, volumetric and morphology data, *J. Appl. Crystallogr.*, 2011, **44**, 1272–1276.
- 41 T. Arima, Y. Tokura and J. B. Torrance, Variation of optical gaps in perovskite-type 3d transition-metal oxides, *Phys. Rev. B*, 1993, **48**, 17006–17009.
- 42 F. M. F. de Groot, M. Grioni, J. C. Fuggle, J. Ghijsen, G. A. Sawatzky and H. Petersen, Oxygen 1s x-ray-absorption edges of transition-metal oxides, *Phys. Rev. B*, 1989, **40**, 5715–5723.
- 43 A. J. Freeman, *The Actinides: Electronic Structure and Related Properties*, Elsevier, 2012.
- 44 E. Pastor, M. Sachs, S. Selim, J. R. Durrant, A. A. Bakulin and A. Walsh, Electronic defects in metal oxide photocatalysts, *Nat. Rev. Mater.*, 2022, **7**, 503–521.
- 45 A. Grimaud, K. J. May, C. E. Carlton, Y.-L. Lee, M. Risch, W. T. Hong, J. Zhou and Y. Shao-Horn, Double perovskites as a family of highly active catalysts for oxygen evolution in alkaline solution, *Nat. Commun.*, 2013, **4**, 2439.
- 46 J. Hwang, R. R. Rao, L. Giordano, Y. Katayama, Y. Yu and Y. Shao-Horn, Perovskites in catalysis and electrocatalysis, *Science*, 2017, **358**, 751–756.
- 47 H. El-Gibally, S. Shousha, N. K. Allam and M. Youssef, Maximizing the electronic charge carriers in donor-doped hematite under oxygen-rich conditions via doping and co-doping strategies revealed by density functional theory calculations, *J. Appl. Phys.*, 2022, **131**, 155705.
- 48 T. J. Smart, M. Chen, A. C. Grieder, V. Urena Baltazar, F. Bridges, Y. Li and Y. Ping, The critical role of synthesis conditions on small polaron carrier concentrations in hematite—A first-principles study, *J. Appl. Phys.*, 2021, **130**, 245705.
- 49 Z. Xiong, L. Zhong, H. Wang and X. Li, Structural Defects, Mechanical Behaviors, and Properties of Two-Dimensional Materials, *Materials*, 2021, **14**, 1192.
- 50 J. Husek, A. Cirri, S. Biswas and L. Robert Baker, Surface electron dynamics in hematite ( $\alpha$ -Fe<sub>2</sub>O<sub>3</sub>): correlation between ultrafast surface electron trapping and small polaron formation, *Chem. Sci.*, 2017, **8**, 8170–8178.
- 51 R. Amri, S. Sahel, D. Gamra, M. Lejeune, M. Clin, K. Zellama and H. Bouchriha, Photonic band gap and defect mode of one-dimensional photonic crystal coated from a mixture of (HMDSO, N<sub>2</sub>) layers deposited by PECVD, *Superlattices Microstruct.*, 2017, **104**, 298–307.
- 52 T. Holstein, Studies of polaron motion: Part I. The molecular-crystal model, *Ann. Phys.*, 1959, **8**, 325–342.

- 53 T. Holstein, Studies of polaron motion: Part II. The “small” polaron, *Ann. Phys.*, 1959, **8**, 343–389.
- 54 C. Franchini, M. Reticcioli, M. Setvin and U. Diebold, Polarons in materials, *Nat. Rev. Mater.*, 2021, **6**, 560–586.
- 55 C. Cheng, Y. Zhu, Z. Zhou, R. Long and W.-H. Fang, Photoinduced small electron polarons generation and recombination in hematite, *Npj Comput. Mater.*, 2022, **8**, 1–8.
- 56 H. Ishii, K. Honma, N. Kobayashi and K. Hirose, Wave-packet approach to transport properties of carrier coupled with intermolecular and intramolecular vibrations of organic semiconductors, *Phys. Rev. B*, 2012, **85**, 245206.
- 57 O. F. Schirmer, M. Imlau and C. Merschjann, Bulk photovoltaic effect of  $\text{LiNbO}_3\text{:Fe}$  and its small-polaron-based microscopic interpretation, *Phys. Rev. B*, 2011, **83**, 165106.
- 58 O. Gerbig, R. Merkle and J. Maier, Electron and Ion Transport In  $\text{Li}_2\text{O}_2$ , *Adv. Mater.*, 2013, **25**, 3129–3133.
- 59 T. Maxisch, F. Zhou and G. Ceder, Ab initio study of the migration of small polarons in olivine  $\text{Li}_x\text{FePO}_4$  and their association with lithium ions and vacancies, *Phys. Rev. B*, 2006, **73**, 104301.
- 60 P. Liao and E. A. Carter, New concepts and modeling strategies to design and evaluate photo-electro- catalysts based on transition metal oxides, *Chem. Soc. Rev.*, 2013, **42**, 2401–2422.
- 61 E. Thimsen, F. Le Formal, M. Grätzel and S. C. Warren, Influence of Plasmonic Au Nanoparticles on the Photoactivity of  $\text{Fe}_2\text{O}_3$  Electrodes for Water Splitting, *Nano Lett.*, 2011, **11**, 35–43.
- 62 A. Yildiz, S. B. Lisesivdin, M. Kasap and D. Mardare, Non-adiabatic small polaron hopping conduction in Nb-doped  $\text{TiO}_2$  thin film, *Phys. B Condens. Matter*, 2009, **404**, 1423–1426.
- 63 H. Kakemoto, Y. Makita, Y. Kino, S. Sakuragi and T. Tsukamoto, Small polaron of  $\beta\text{-FeSi}_2$  obtained from optical measurements, *Thin Solid Films*, 2001, **381**, 251–255.
- 64 S.-F. Wang, Y.-F. Hsu, H.-C. Lu, C.-C. Huang and C.-T. Yeh,  $\text{Sr}_{1-x}\text{Pr}_x\text{Co}_{0.95}\text{Sn}_{0.05}\text{O}_{3-\delta}$  ceramic as a cathode material for intermediate-temperature solid oxide fuel cells, *Int. J. Hydrog. Energy*, 2012, **37**, 12548–12556.
- 65 I. G. Austin and N. F. Mott, Polarons in crystalline and non-crystalline materials, *Adv. Phys.*, 1969, **18**, 41–102.
- 66 R. A. Marcus, On the Theory of Oxidation-Reduction Reactions Involving Electron Transfer. I, *J. Chem. Phys.*, 1956, **24**, 966–978.
- 67 L. P. Kadanoff, Boltzmann Equation for Polarons, *Phys. Rev.*, 1963, **130**, 1364–1369.
- 68 C. Motta and S. Sanvito, Electron–Phonon Coupling and Polaron Mobility in Hybrid Perovskites from First Principles, *J. Phys. Chem. C*, 2018, **122**, 1361–1366.
- 69 E. T. Wefring, M.-A. Einarsrud and T. Grande, Electrical conductivity and thermopower of  $(1-x)\text{BiFeO}_3-x\text{Bi}_{0.5}\text{K}_{0.5}\text{TiO}_3$  ( $x = 0.1, 0.2$ ) ceramics near the ferroelectric to paraelectric phase transition, *Phys. Chem. Chem. Phys.*, 2015, **17**, 9420–9428.
- 70 T. J. Smart and Y. Ping, Effect of defects on the small polaron formation and transport properties of hematite from first-principles calculations, *J. Phys. Condens. Matter*, 2017, **29**, 394006.
- 71 Y. Ling, G. Wang, D. A. Wheeler, J. Z. Zhang and Y. Li, Sn-Doped Hematite Nanostructures for Photoelectrochemical Water Splitting, *Nano Lett.*, 2011, **11**, 2119–2125.

- 72 A. Kay, I. Cesar and M. Grätzel, New Benchmark for Water Photooxidation by Nanostructured  $\alpha$ -Fe<sub>2</sub>O<sub>3</sub> Films, *J. Am. Chem. Soc.*, 2006, **128**, 15714–15721.
- 73 B. Zhao, T. C. Kaspar, T. C. Droubay, J. McCloy, M. E. Bowden, V. Shutthanandan, S. M. Heald and S. A. Chambers, Electrical transport properties of Ti-doped Fe<sub>1-x</sub>O<sub>2</sub> (0001) epitaxial films, *Phys. Rev. B*, 2011, **84**, 245325.
- 74 J. Liu, Y. Y. Cai, Z. F. Tian, G. S. Ruan, Y. X. Ye, C. H. Liang and G. S. Shao, Highly oriented Ge-doped hematite nanosheet arrays for photoelectrochemical water oxidation, *Nano Energy*, 2014, **9**, 282–290.
- 75 Z. Zhou, R. Long and O. V. Prezhdo, Why Silicon Doping Accelerates Electron Polaron Diffusion in Hematite, *J. Am. Chem. Soc.*, 2019, **141**, 20222–20233.
- 76 K. Uchida, R. Zednik, Ching-Huang Lu, H. Jagannathan, J. McVittie, P. C. McIntyre and Y. Nishi, in *IEDM Technical Digest. IEEE International Electron Devices Meeting, 2004.*, IEEE, San Francisco, CA, USA, 2004, pp. 229–232.
- 77 A. Janotti, D. Steiauf and C. G. Van de Walle, Strain effects on the electronic structure of SrTiO<sub>3</sub>: Toward high electron mobilities, *Phys. Rev. B*, 2011, **84**, 201304.
- 78 N. Kelaidis, A. Kordatos, S.-R. G. Christopoulos and A. Chroneos, A roadmap of strain in doped anatase TiO<sub>2</sub>, *Sci. Rep.*, 2018, **8**, 12790.
- 79 Y. Wang, R. Sui, M. Bi, W. Tang and S. Ma, Strain sensitivity of band structure and electron mobility in perovskite BaSnO<sub>3</sub>: first-principles calculation, *RSC Adv.*, 2019, **9**, 14072–14077.
- 80 W. S. Choi and H. N. Lee, Strain tuning of electronic structure in Bi<sub>4</sub>Ti<sub>3</sub>O<sub>12</sub>–LaCoO<sub>3</sub> epitaxial thin films, *Phys. Rev. B*, 2015, **91**, 174101.
- 81 L. Chen, C. Shi, X. Li, Z. Mi, D. Wang, H. Liu and L. Qiao, Strain Effect on Electronic Structure and Work Function in  $\alpha$ -Fe<sub>2</sub>O<sub>3</sub> Films, *Materials*, 2017, **10**, 273.
- 82 J. P. Perdew, K. Burke and M. Ernzerhof, Generalized Gradient Approximation Made Simple, *Phys. Rev. Lett.*, 1996, **77**, 3865–3868.
- 83 A. Dal Corso, Pseudopotentials periodic table: From H to Pu, *Comput. Mater. Sci.*, 2014, **95**, 337–350.
- 84 D. Vanderbilt, Soft self-consistent pseudopotentials in a generalized eigenvalue formalism, *Phys. Rev. B*, 1990, **41**, 7892–7895.
- 85 G. Prandini, A. Marrazzo, I. E. Castelli, N. Mounet and N. Marzari, Precision and efficiency in solid-state pseudopotential calculations, *Npj Comput. Mater.*, 2018, **4**, 1–13.
- 86 K. Lejaeghere, G. Bihlmayer, T. Björkman, P. Blaha, S. Blügel, V. Blum, D. Caliste, I. E. Castelli, S. J. Clark, A. Dal Corso, S. de Gironcoli, T. Deutsch, J. K. Dewhurst, I. Di Marco, C. Draxl, M. Dułak, O. Eriksson, J. A. Flores-Livas, K. F. Garrity, L. Genovese, P. Giannozzi, M. Giantomassi, S. Goedecker, X. Gonze, O. Grånäs, E. K. U. Gross, A. Gulans, F. Gygi, D. R. Hamann, P. J. Hasnip, N. A. W. Holzwarth, D. Iușan, D. B. Jochym, F. Jollet, D. Jones, G. Kresse, K. Koepnick, E. Küçükbenli, Y. O. Kvashnin, I. L. M. Locht, S. Lubeck, M. Marsman, N. Marzari, U. Nitzsche, L. Nordström, T. Ozaki, L. Paulatto, C. J. Pickard, W. Poelmans, M. I. J. Probert, K. Refson, M. Richter, G.-M. Rignanese, S. Saha, M. Scheffler, M. Schlipf, K. Schwarz, S. Sharma, F. Tavazza, P. Thunström, A. Tkatchenko, M. Torrent, D. Vanderbilt, M. J. van Setten, V. Van Speybroeck, J. M. Wills, J. R. Yates, G.-X. Zhang and S. Cottenier, Reproducibility in density functional theory calculations of solids, *Science*, 2016, **351**, aad3000.
- 87 P. Giannozzi, O. Andreussi, T. Brumme, O. Bunau, M. B. Nardelli, M. Calandra, R. Car, C. Cavazzoni, D. Ceresoli, M. Cococcioni, N. Colonna, I. Carnimeo, A. D. Corso, S. de

- Gironcoli, P. Delugas, R. A. DiStasio, A. Ferretti, A. Floris, G. Fratesi, G. Fugallo, R. Gebauer, U. Gerstmann, F. Giustino, T. Gorni, J. Jia, M. Kawamura, H.-Y. Ko, A. Kokalj, E. Küçükbenli, M. Lazzeri, M. Marsili, N. Marzari, F. Mauri, N. L. Nguyen, H.-V. Nguyen, A. Otero-de-la-Roza, L. Paulatto, S. Poncé, D. Rocca, R. Sabatini, B. Santra, M. Schlipf, A. P. Seitsonen, A. Smogunov, I. Timrov, T. Thonhauser, P. Umari, N. Vast, X. Wu and S. Baroni, Advanced capabilities for materials modelling with Quantum ESPRESSO, *J. Phys. Condens. Matter*, 2017, **29**, 465901.
- 88 P. Giannozzi, S. Baroni, N. Bonini, M. Calandra, R. Car, C. Cavazzoni, D. Ceresoli, G. L. Chiarotti, M. Cococcioni, I. Dabo, A. D. Corso, S. de Gironcoli, S. Fabris, G. Fratesi, R. Gebauer, U. Gerstmann, C. Gougoussis, A. Kokalj, M. Lazzeri, L. Martin-Samos, N. Marzari, F. Mauri, R. Mazzarello, S. Paolini, A. Pasquarello, L. Paulatto, C. Sbraccia, S. Scandolo, G. Sclauzero, A. P. Seitsonen, A. Smogunov, P. Umari and R. M. Wentzcovitch, QUANTUM ESPRESSO: a modular and open-source software project for quantum simulations of materials, *J. Phys. Condens. Matter*, 2009, **21**, 395502.
- 89 J. P. Perdew, R. G. Parr, M. Levy and J. L. Balduz, Density-Functional Theory for Fractional Particle Number: Derivative Discontinuities of the Energy, *Phys. Rev. Lett.*, 1982, **49**, 1691–1694.
- 90 W. Wunderlich, H. Ohta and K. Koumoto, Enhanced effective mass in doped SrTiO<sub>3</sub> and related perovskites, *Phys. B Condens. Matter*, 2009, **404**, 2202–2212.
- 91 H. Peng and S. Lany, Semiconducting transition-metal oxides based on  $d^5$  cations: Theory for MnO and FeO, *Phys. Rev. B*, 2012, **85**, 201202.
- 92 O. Neufeld and M. Caspary Toroker, Play the heavy: An effective mass study for  $\alpha$ -Fe<sub>2</sub>O<sub>3</sub> and corundum oxides, *J. Chem. Phys.*, 2016, **144**, 164704.
- 93 C. Kittel and P. McEuen, *Introduction to solid state physics*, John Wiley & Sons, 2018.
- 94 B. Van Zeghbroeck, Principles of semiconductor devices, 2004, *Colo. Univ. Ed.*
- 95 C. Xia, Y. Jia, M. Tao and Q. Zhang, Tuning the band gap of hematite  $\alpha$ -Fe<sub>2</sub>O<sub>3</sub> by sulfur doping, *Phys. Lett. A*, 2013, **377**, 1943–1947.
- 96 X. Meng, G. Qin, W. A. I. Goddard, S. Li, H. Pan, X. Wen, Y. Qin and L. Zuo, Theoretical Understanding of Enhanced Photoelectrochemical Catalytic Activity of Sn-Doped Hematite: Anisotropic Catalysis and Effects of Morin Transition and Sn Doping, *J. Phys. Chem. C*, 2013, **117**, 3779–3784.
- 97 S. Yip, *Handbook of Materials Modeling*, Springer Science & Business Media, 2007.
- 98 L. Chen, C. Shi, X. Li, Z. Mi, D. Wang, H. Liu and L. Qiao, Strain Effect on Electronic Structure and Work Function in  $\alpha$ -Fe<sub>2</sub>O<sub>3</sub> Films, *Materials*, 2017, **10**, 273.
- 99 H. Pan, X. Meng, D. Liu, S. Li and G. Qin, (Ti/Zr,N) codoped hematite for enhancing the photoelectrochemical activity of water splitting, *Phys. Chem. Chem. Phys.*, 2015, **17**, 22179–22186.
- 100 C. Xia, Y. Jia, M. Tao and Q. Zhang, Tuning the band gap of hematite  $\alpha$ -Fe<sub>2</sub>O<sub>3</sub> by sulfur doping, *Phys. Lett. A*, 2013, **377**, 1943–1947.
- 101 Q. Deng, R. Huang, L. Shao, A. V. Mumyatov, P. A. Troshin, C. An, S. Wu, L. Gao, B. Yang and N. Hu, Atomic understanding of the strain-induced electrocatalysis from DFT calculation: progress and perspective, *Phys. Chem. Chem. Phys.*, 2023, **25**, 12565–12586.
- 102 T. C. T. Ting and T. Chen, Poisson's ratio for anisotropic elastic materials can have no bounds, *Q. J. Mech. Appl. Math.*, 2005, **58**, 73–82.
- 103 D. Chicot, J. Mendoza, A. Zaoui, G. Louis, V. Lepingale, R. Francine and J. Lesage, Mechanical properties of magnetite (Fe<sub>3</sub>O<sub>4</sub>), hematite ( $\alpha$ -Fe<sub>2</sub>O<sub>3</sub>) and goethite ( $\alpha$ -FeO·OH)

- by instrumented indentation and molecular dynamics analysis, *Mater. Chem. Phys.*, 2011, **129**, 862–870.
- 104 C. Zhang, L. Li, Z. Yuan, X. Xu, Z. Song and Y. R. Zhang, Mechanical properties of siderite and hematite from DFT calculation, *Miner. Eng.*, 2020, **146**, 106107.
- 105 Y. Hinuma, G. Pizzi, Y. Kumagai, F. Oba and I. Tanaka, Band structure diagram paths based on crystallography, *Comput. Mater. Sci.*, 2017, **128**, 140–184.
- 106 D. Radziuk and H. Möhwald, Ultrasonically treated liquid interfaces for progress in cleaning and separation processes, *Phys. Chem. Chem. Phys.*, 2016, **18**, 21–46.
- 107 E. Voloshina, in *Encyclopedia of Interfacial Chemistry*, ed. K. Wandelt, Elsevier, Oxford, 2018, pp. 115–121.
- 108 D. Radziuk and H. Möhwald, Ultrasonically treated liquid interfaces for progress in cleaning and separation processes, *Phys. Chem. Chem. Phys.*, 2016, **18**, 21–46.
- 109 O. Neufeld and M. Caspary Toroker, Play the heavy: An effective mass study for  $\alpha$ -Fe<sub>2</sub>O<sub>3</sub> and corundum oxides, *J. Chem. Phys.*, 2016, **144**, 164704.
- 110 X. Meng, G. Qin, W. A. Goddard, S. Li, H. Pan, X. Wen, Y. Qin and L. Zuo, Theoretical Understanding of Enhanced Photoelectrochemical Catalytic Activity of Sn-Doped Hematite: Anisotropic Catalysis and Effects of Morin Transition and Sn Doping, *J. Phys. Chem. C*, 2013, **117**, 3779–3784.
- 111 O. Bengone, M. Alouani, P. Blöchl and J. Hugel, Implementation of the projector augmented-wave LDA+U method: Application to the electronic structure of NiO, *Phys. Rev. B*, 2000, **62**, 16392–16401.
- 112 H. Peng and S. Lany, Semiconducting transition-metal oxides based on  $d^5$  cations: Theory for MnO and FeO, *Phys. Rev. B*, 2012, **85**, 201202.
- 113 Y. Zhang, S. Jiang, W. Song, P. Zhou, H. Ji, W. Ma, W. Hao, C. Chen and J. Zhao, Nonmetal P-doped hematite photoanode with enhanced electron mobility and high water oxidation activity, *Energy Environ. Sci.*, 2015, **8**, 1231–1236.
- 114 A. J. Bosman and H. J. Van Daal, Small-polaron versus band conduction in some transition-metal oxides, *Adv. Phys.*, 1970, **19**, 1–117.
- 115 D. Yu, Y. Zhang and F. Liu, First-principles study of electronic properties of biaxially strained silicon: Effects on charge carrier mobility, *Phys. Rev. B*, 2008, **78**, 245204.
- 116 A. Janotti, D. Steiauf and C. G. Van De Walle, Strain effects on the electronic structure of SrTiO<sub>3</sub>: Toward high electron mobilities, *Phys. Rev. B*, 2011, **84**, 201304.
- 117 M. W. Terban and S. J. L. Billinge, Structural Analysis of Molecular Materials Using the Pair Distribution Function, *Chem. Rev.*, 2022, **122**, 1208–1272.
- 118 D. Çakır, H. Sahin and F. M. Peeters, Tuning of the electronic and optical properties of single-layer black phosphorus by strain, *Phys. Rev. B*, 2014, **90**, 205421.
- 119 K. Navamani, G. Saranya, P. Kolandaivel and K. Senthilkumar, Effect of structural fluctuations on charge carrier mobility in thiophene, thiazole and thiazolothiazole based oligomers, *Phys. Chem. Chem. Phys.*, 2013, **15**, 17947–17961.
- 120 K. Sivula, F. Le Formal and M. Grätzel, Solar Water Splitting: Progress Using Hematite ( $\alpha$ -Fe<sub>2</sub>O<sub>3</sub>) Photoelectrodes, *ChemSusChem*, 2011, **4**, 432–449.
- 121 E. Pastor, J.-S. Park, L. Steier, S. Kim, M. Grätzel, J. R. Durrant, A. Walsh and A. A. Bakulin, In situ observation of picosecond polaron self-localisation in  $\alpha$ -Fe<sub>2</sub>O<sub>3</sub> photoelectrochemical cells, *Nat. Commun.*, 2019, **10**, 3962.

- 122 G. Corradi, I. M. Zaritskii, A. Hofstaetter, K. Polgár and L. G. Rakitina, Ti <sup>3+</sup> on Nb site: A paramagnetic Jahn-Teller center in vacuum-reduced LiNbO<sub>3</sub>: Mg: Ti single crystals, *Phys. Rev. B*, 1998, **58**, 8329–8337.
- 123 M. Youssef, B. Yildiz and K. J. Van Vliet, Thermomechanical stabilization of electron small polarons in  $\mathrm{SrTiO}_3$  assessed by the quasiharmonic approximation, *Phys. Rev. B*, 2017, **95**, 161110.
- 124 P. Sharma, J. Jang and J. S. Lee, Key Strategies to Advance the Photoelectrochemical Water Splitting Performance of  $\alpha\text{-Fe}_2\text{O}_3$  Photoanode, *ChemCatChem*, 2019, **11**, 157–179.

# Appendix

## 1. Quantum Espresso Sample Input files

### A. small polaron calculations

&CONTROL

```
calculation = 'relax' ,  
verbosity = 'high' ,  
restart_mode = 'from_scratch' ,  
prefix='fe2o3' ,  
outdir='.' ,  
pseudo_dir = './' ,  
tstress = .true. ,  
tprnfor= .true. ,  
nstep = 2000 ,  
etot_conv_thr = 7.7D-6 ,  
forc_conv_thr = 4.0D-5 ,  
/  

```

&SYSTEM

```
ibrav = 0 ,  
nat = 80 ,  
ntyp = 4 ,  
nbnd = 480 ,  
ecutwfc = 90 ,  
ecutrho = 1080 ,
```

```

occupations = 'smearing',
smearing = 'gaussian',
nspin = 2 ,
degauss = 0.004 ,! In Ry
starting_magnetization(1)=0.3,
starting_magnetization(2)=-0.3,
nosym = .TRUE. ,
lda_plus_u = .TRUE. ,
Hubbard_U(1) = 4.0 ,
Hubbard_U(2) = 4.0 ,
Hubbard_U(3) = 6.5 ,
tot_charge = 1.0 ,
/
&ELECTRONS
    diagonalization='david',
    mixing_mode = 'plain' ,
    mixing_beta = 0.3,
    startingwfc = 'random',
    conv_thr = 1.0d-8 ,
    electron_maxstep= 250,
    scf_must_converge = .false.,
/
&ions

```



```

ion_dynamics='bfgs'

/

&CELL

cell_dynamics = 'bfgs' ,

cell_dofree = 'all',

press_conv_thr = 0.5 , ! This is the default

/
CELL_PARAMETERS  angstrom
10.9078826904      0.0000000000      0.0000000000
6.1982832762       8.9756999291      0.0000000000
6.1982844157       3.2522741273      8.3657581185

ATOMIC_SPECIES

Fe1    55.845 Fe.pbe-spn-rrkjus_psl.0.2.1.UPF

Fe2    55.845 Fe.pbe-spn-rrkjus_psl.0.2.1.UPF

O      15.999 O.pbe-n-rrkjus_psl.0.1.UPF

Cl     35.453 Cl_pbe_v1.4.uspp.F.UPF

ATOMIC_POSITIONS crystal

Fe1    0.072655238      0.072655469      0.072655506
Fe1    0.072655238      0.072655469      0.572655499
Fe1    0.072655238      0.572655439      0.072655506
Fe1    0.072655238      0.572655439      0.572655499
Fe1    0.572655261      0.072655469      0.072655506
Fe1    0.572655261      0.072655469      0.572655499
Fe1    0.572655261      0.572655439      0.072655506
Fe1    0.572655261      0.572655439      0.572655499
Fe1    0.427344322      0.427344590      0.427344739
Fe1    0.427344322      0.427344590      0.927344739
Fe1    0.427344322      0.927344561      0.427344739
Fe1    0.427344322      0.927344561      0.927344739
Fe1    0.927344322      0.427344590      0.427344739
Fe1    0.927344322      0.427344590      0.927344739
Fe1    0.927344322      0.927344561      0.427344739

```

Fe1	0.927344322	0.927344561	0.927344739
Fe2	0.177344710	0.177344665	0.177344412
Fe2	0.177344710	0.177344665	0.677344441
Fe2	0.177344710	0.677344680	0.177344412
Fe2	0.177344710	0.677344680	0.677344441
Fe2	0.677344680	0.177344665	0.177344412
Fe2	0.677344680	0.177344665	0.677344441
Fe2	0.677344680	0.677344680	0.177344412
Fe2	0.677344680	0.677344680	0.677344441
Fe2	0.322655380	0.322655290	0.322655141
Fe2	0.322655380	0.322655290	0.822655141
Fe2	0.322655380	0.822655320	0.322655141
Fe2	0.322655380	0.822655320	0.822655141
Fe2	0.822655380	0.322655290	0.322655141
Fe2	0.822655380	0.322655290	0.822655141
Fe2	0.822655380	0.822655320	0.322655141
Fe2	0.822655380	0.822655320	0.822655141
O	0.375000000	0.222671553	0.027328292
O	0.375000000	0.222671553	0.527328312
O	0.375000000	0.722671568	0.027328292
O	0.375000000	0.722671568	0.527328312
O	0.875000000	0.222671553	0.027328292
O	0.875000000	0.222671553	0.527328312
O	0.875000000	0.722671568	0.027328292
O	0.875000000	0.722671568	0.527328312
O	0.472671509	0.124999851	0.277328521
O	0.472671509	0.124999851	0.777328491
O	0.472671509	0.624999881	0.277328521
O	0.472671509	0.624999881	0.777328491
O	0.972671509	0.124999851	0.277328521
O	0.972671509	0.124999851	0.777328491
O	0.972671509	0.624999881	0.277328521
O	0.972671509	0.624999881	0.777328491
O	0.222671539	0.027328350	0.374999911
O	0.222671539	0.027328350	0.874999881
O	0.222671539	0.527328372	0.374999911
O	0.222671539	0.527328372	0.874999881
O	0.722671509	0.027328350	0.374999911
O	0.722671509	0.027328350	0.874999881
O	0.722671509	0.527328372	0.374999911
O	0.722671509	0.527328372	0.874999881
Cl	0.722671509	0.527328372	0.874999881
O	0.124999948	0.277328312	0.472671568
O	0.124999948	0.277328312	0.972671568
O	0.124999948	0.777328312	0.472671568
O	0.124999948	0.777328312	0.972671568
O	0.624999940	0.277328312	0.472671568

O	0.624999940	0.277328312	0.972671568
O	0.624999940	0.777328312	0.472671568
O	0.624999940	0.777328312	0.972671568
O	0.027328448	0.374999940	0.222671479
O	0.027328448	0.374999940	0.722671509
O	0.027328448	0.874999940	0.222671479
O	0.027328448	0.874999940	0.722671509
O	0.527328432	0.374999940	0.222671479
O	0.527328432	0.374999940	0.722671509
O	0.527328432	0.874999940	0.222671479
O	0.527328432	0.874999940	0.722671509
O	0.277328402	0.472671449	0.125000030
O	0.277328402	0.472671449	0.625000000
O	0.277328402	0.972671449	0.125000030
O	0.277328402	0.972671449	0.625000000
O	0.777328372	0.472671449	0.125000030
O	0.777328372	0.472671449	0.625000000
O	0.777328372	0.972671449	0.125000030
O	0.777328372	0.972671449	0.625000000

K\_POINTS automatic

2 2 2 0 0 0

## 2. DFT Energies

### A. Hubbard U values of U(Fe) = 3.0 eV and U(O) = 7.0 eV

Electrons		
Strain (%)	Small polaron electron (Ry)	Large polaron electron (Ry)
-5.000	-9747.40773250	-9747.39733840
-4.500	-9747.49659216	-9747.48651503
-4.000	-9747.57641539	-9747.56655737
-3.500	-9747.64715529	-9747.63755889
-3.000	-9747.70899549	-9747.69967847
-2.500	-9747.76216007	-9747.75307705
-2.000	-9747.80679740	-9747.79793665
-1.500	-9747.83736888	-9747.83430941
-1.000	-9747.87086019	-9747.86241569
-0.500	-9747.88626285	-9747.88241739
0.000	-9747.90251186	-9747.89437281
0.500	-9747.90642946	-9747.89839077
1.000	-9747.90270359	-9747.89477002
1.500	-9747.89146209	-9747.88358624
2.000	-9747.87281251	-9747.86493933

2.500	-9747.84690900	-9747.83904073
3.000	-9747.81423087	-9747.80602150
3.500	-9747.77474633	-9747.76600847
4.000	-9747.72857050	-9747.71919430
4.500	-9747.67575179	-9747.66570168
5.000	-9747.61646458	-9747.60563176

Holes		
Strain (%)	Small polaron electron (Ry)	Large polaron electron (Ry)
-5.000	-9749.07342603	-9749.06471245
-4.500	-9749.14599768	-9749.13700686
-4.000	-9749.20964213	-9749.20026022
-3.500	-9749.24985370	-9749.25454694
-3.000	-9749.29813088	-9749.30006758
-2.500	-9749.33795670	-9749.33694703
-2.000	-9749.36942596	-9749.36533903
-1.500	-9749.39263430	-9749.38540394
-1.000	-9749.40771435	-9749.39718899
-0.500	-9749.41481555	-9749.40091159
0.000	-9749.41408952	-9749.39675204
0.500	-9749.40563316	-9749.38477849
1.000	-9749.38953274	-9749.36511250
1.500	-9749.36600039	-9749.33795650
2.000	-9749.33514978	-9749.30340171
2.500	-9749.29703961	-9749.26160907
3.000	-9749.25189248	-9749.21272480
3.500	-9749.19985050	-9749.15691292
4.000	-9749.14096170	-9749.09424372
4.500	-9749.07540069	-9749.02491160
5.000	-9749.00353093	-9748.94924019

**B. Hubbard U values of  $U(\text{Fe}) = 4.0$  eV and  $U(\text{O}) = 6.5$  eV**

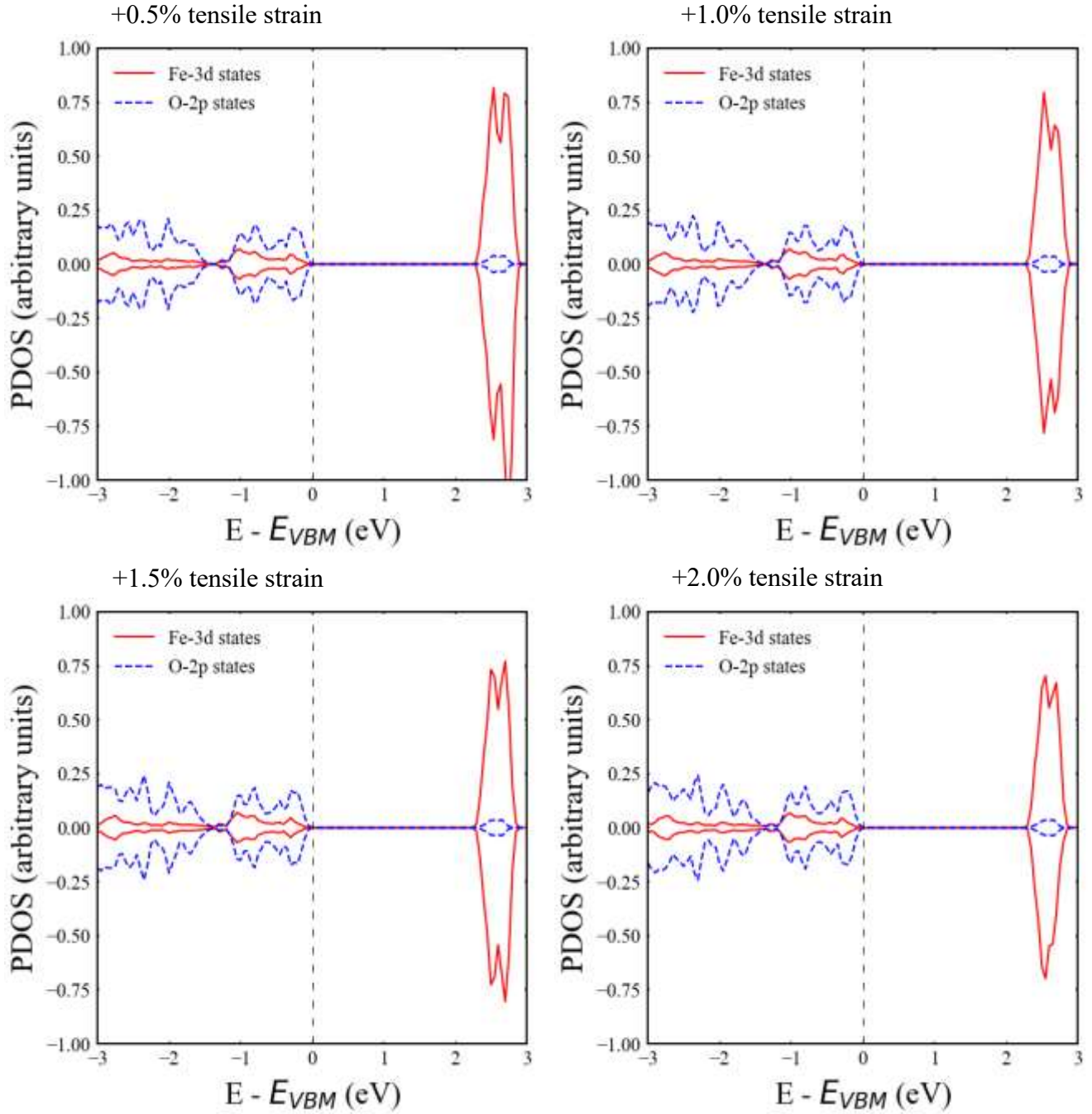
Electrons		
Strain (%)	Small polaron electron (Ry)	Large polaron electron (Ry)
-5.000	-9746.69823971	-9746.67263534
-4.500	-9746.79373988	-9746.76840974
-4.000	-9746.88021809	-9746.85491877
-3.500	-9746.95771901	-9746.93239719
-3.000	-9747.02639971	-9747.00093375
-2.500	-9747.08642100	-9747.06073933

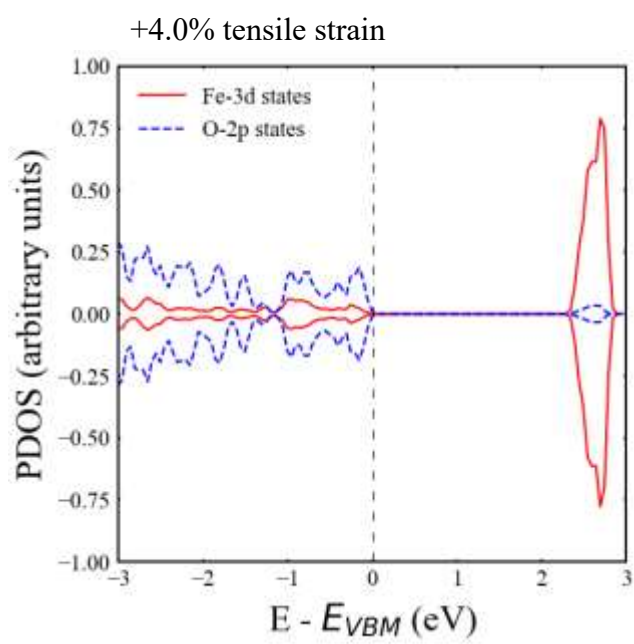
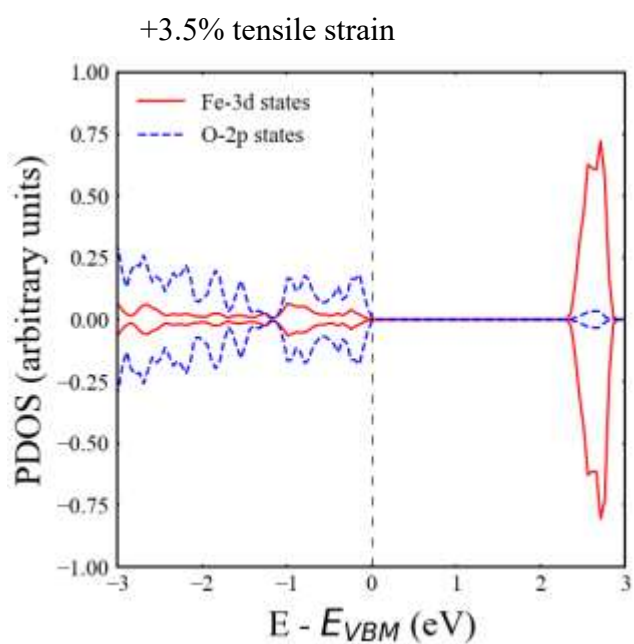
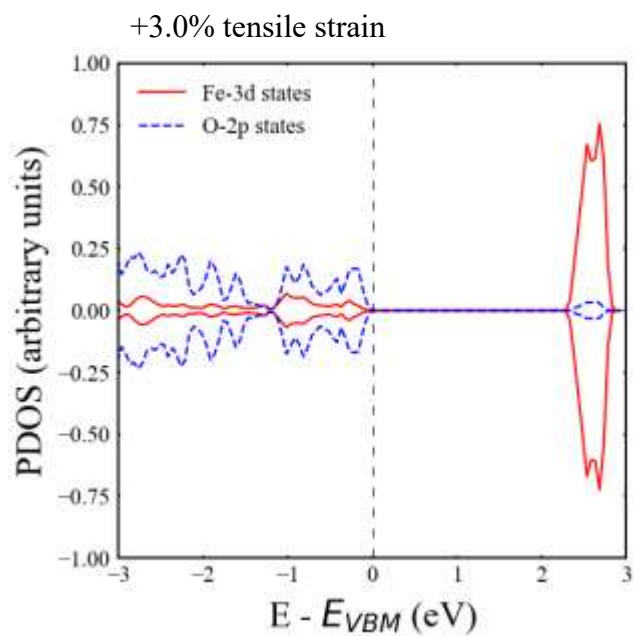
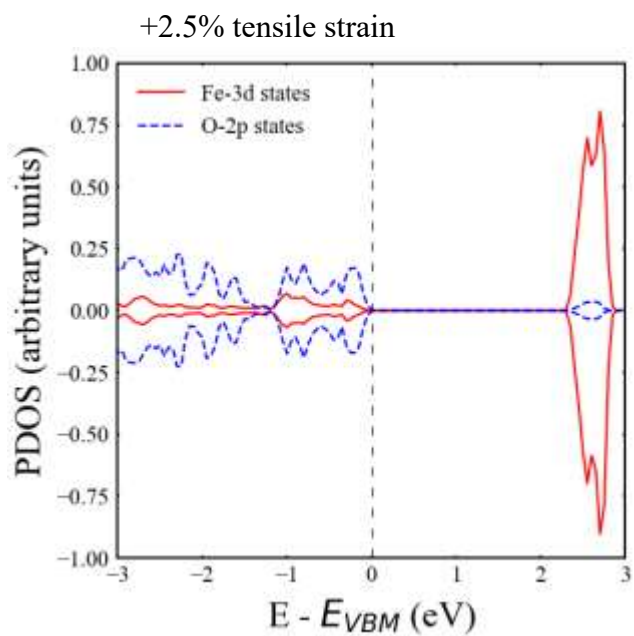
-2.000	-9747.13793586	-9747.11198093
-1.500	-9747.18099469	-9747.15470279
-1.000	-9747.21571120	-9747.18903294
-0.500	-9747.24249988	-9747.21538302
0.000	-9747.26152460	-9747.24262405
0.500	-9747.27208440	-9747.24398856
1.000	-9747.27523048	-9747.24654560
1.500	-9747.27093773	-9747.24160258
2.000	-9747.25826225	-9747.22925495
2.500	-9747.23955068	-9747.20961097
3.000	-9747.21443278	-9747.18285700
3.500	-9747.18098375	-9747.14911495
4.000	-9747.14179244	-9747.10856651
4.500	-9747.09541689	-9747.06132453
5.000	-9747.04256857	-9747.00758283

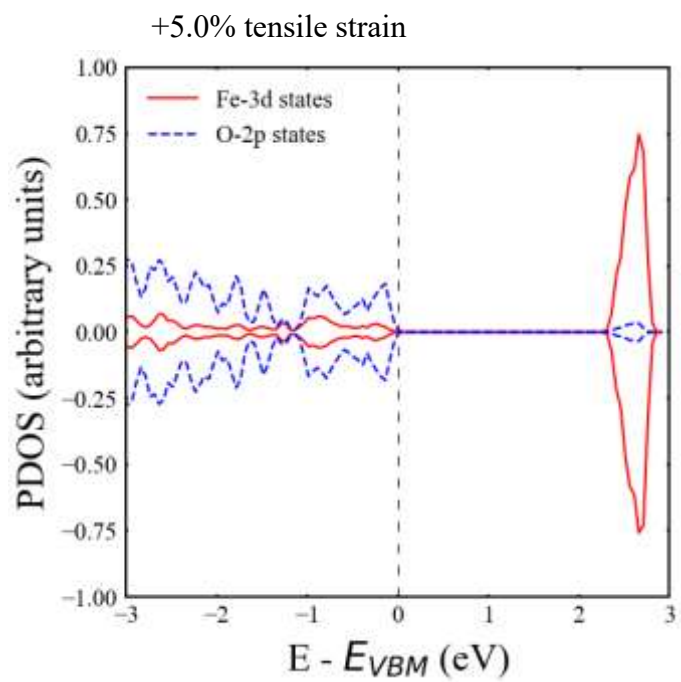
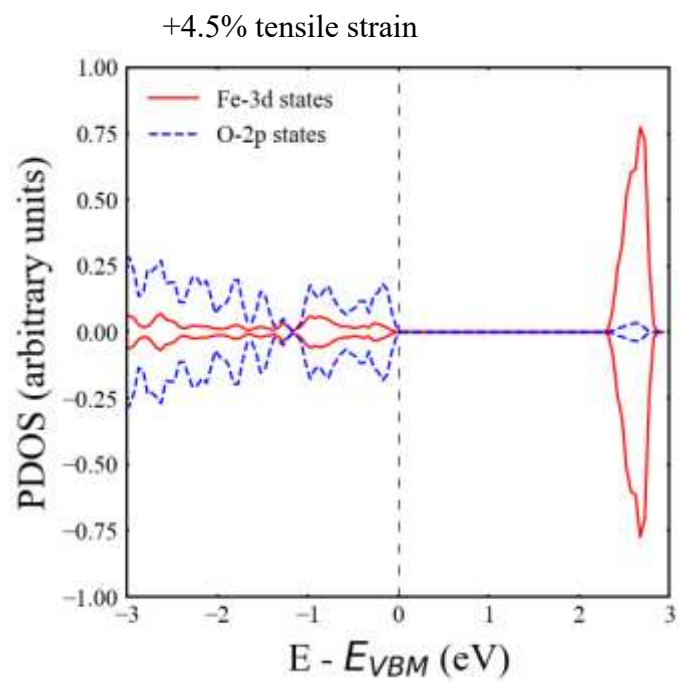
Holes		
Strain (%)	Small polaron electron (Ry)	Large polaron electron (Ry)
-5.000	-9748.35430772	-9748.34724043
-4.500	-9748.43376785	-9748.42640679
-4.000	-9748.50417088	-9748.49643561
-3.500	-9748.55608246	-9748.55752114
-3.000	-9748.61080748	-9748.60978523
-2.500	-9748.65702937	-9748.65339003
-2.000	-9748.69486284	-9748.68848633
-1.500	-9748.72440382	-9748.71517034
-1.000	-9748.74585163	-9748.73367452
-0.500	-9748.75928612	-9748.74407695
0.000	-9748.76368466	-9748.74287538
0.500	-9748.76269576	-9748.74129560
1.000	-9748.75293858	-9748.72834876
1.500	-9748.73573404	-9748.70790415
2.000	-9748.71117796	-9748.68007798
2.500	-9748.67940294	-9748.64503527
3.000	-9748.64057527	-9748.60286235
3.500	-9748.59480406	-9748.55377167
4.000	-9748.54217908	-9748.49782554
4.500	-9748.48297769	-9748.43528003
5.000	-9748.41730663	-9748.36626153

### 3. Projected density of states (PDOS) plots

#### A. Biaxial tensile strain



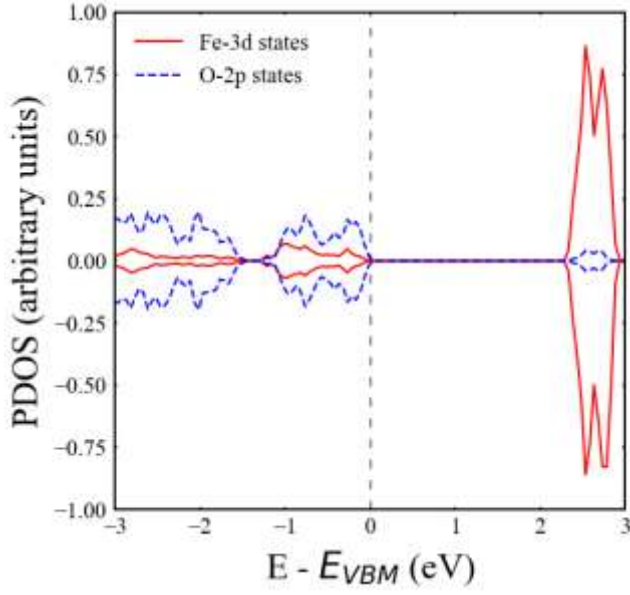




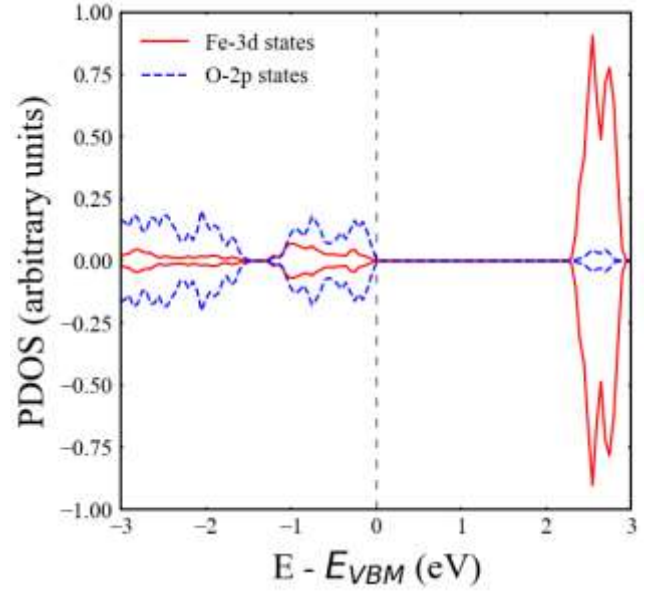


## B. Biaxial compressive strain

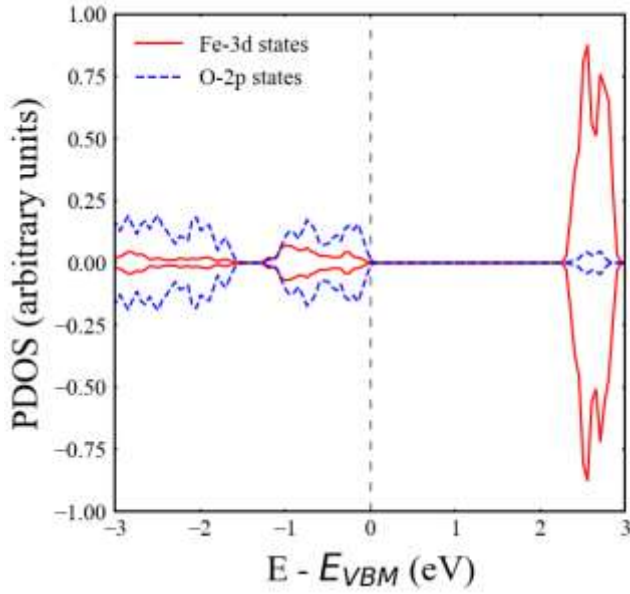
-0.5% compressive strain



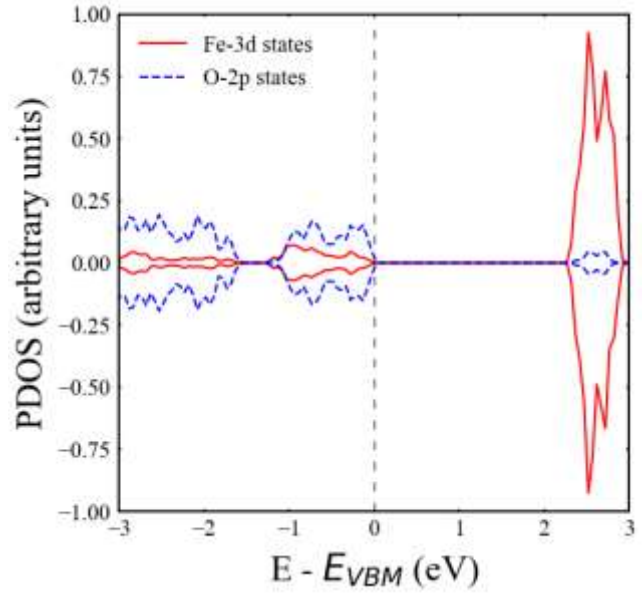
-1.0% compressive strain



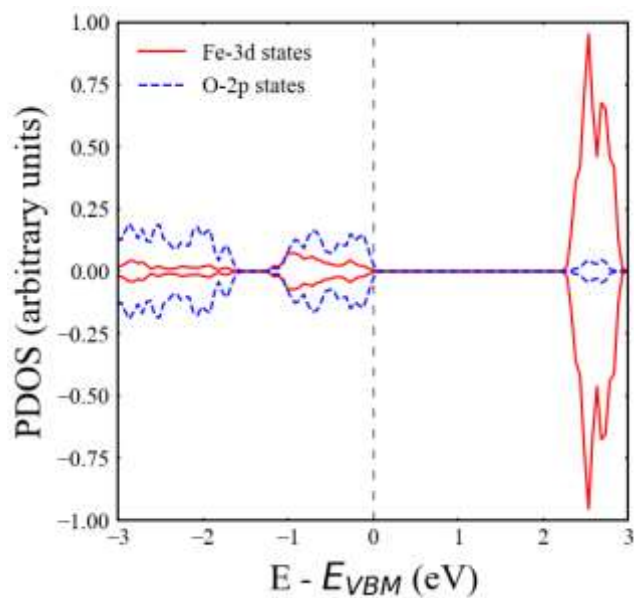
-1.5% compressive strain



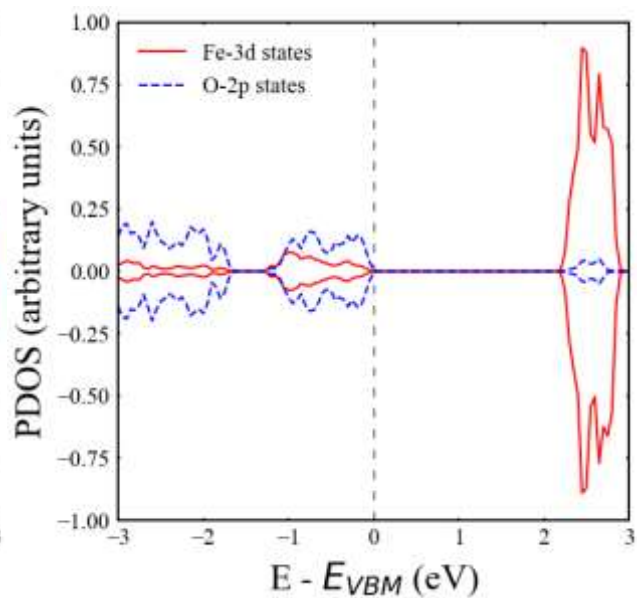
-2.0% compressive strain



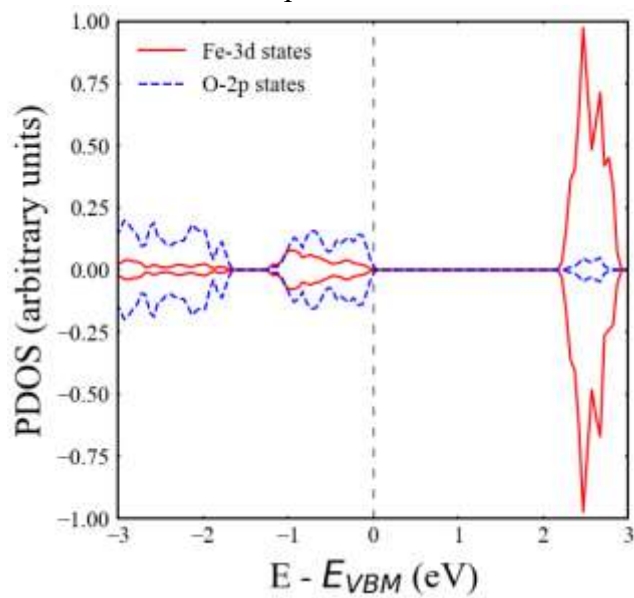
-2.5% compressive strain



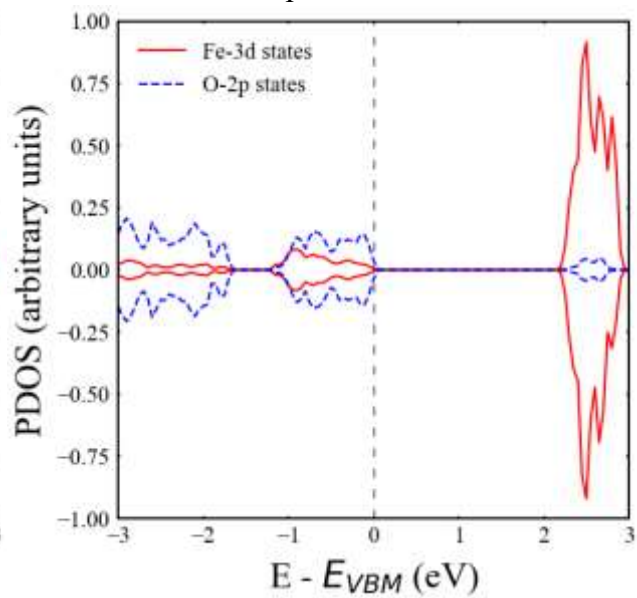
-3.0% compressive strain

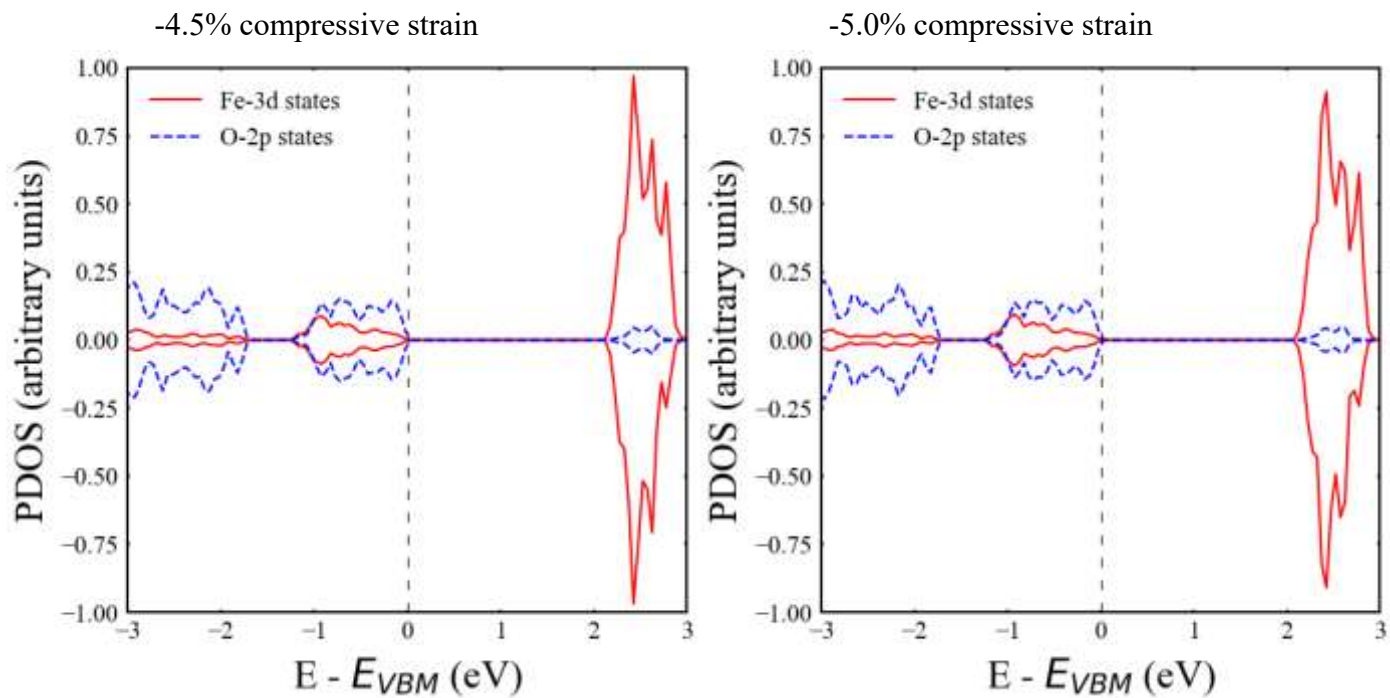


-3.5% compressive strain



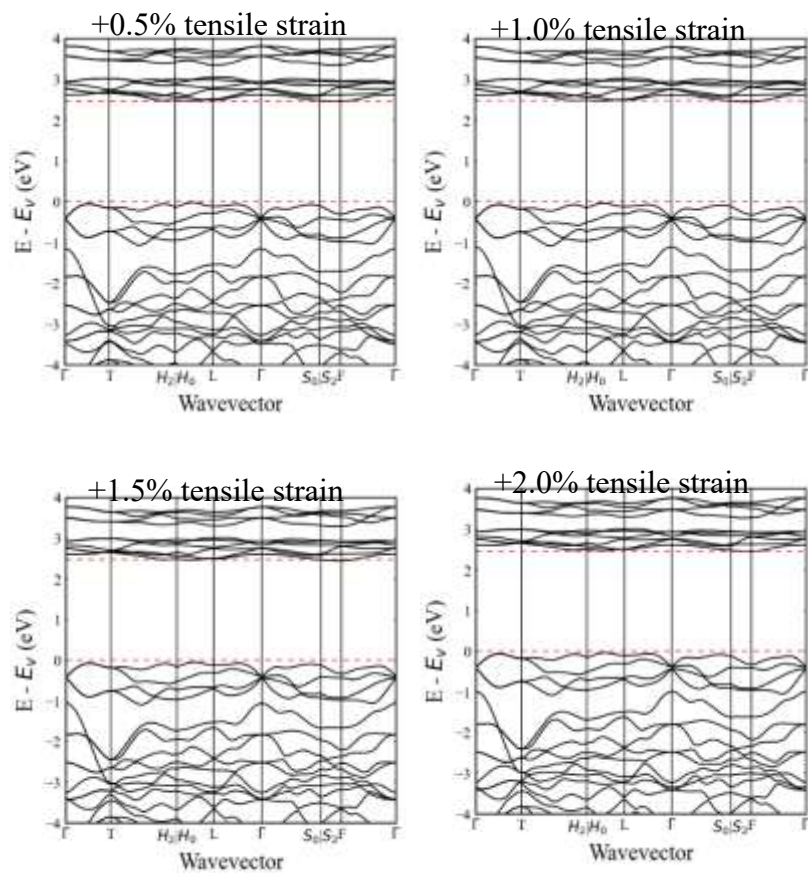
-4.0% compressive strain

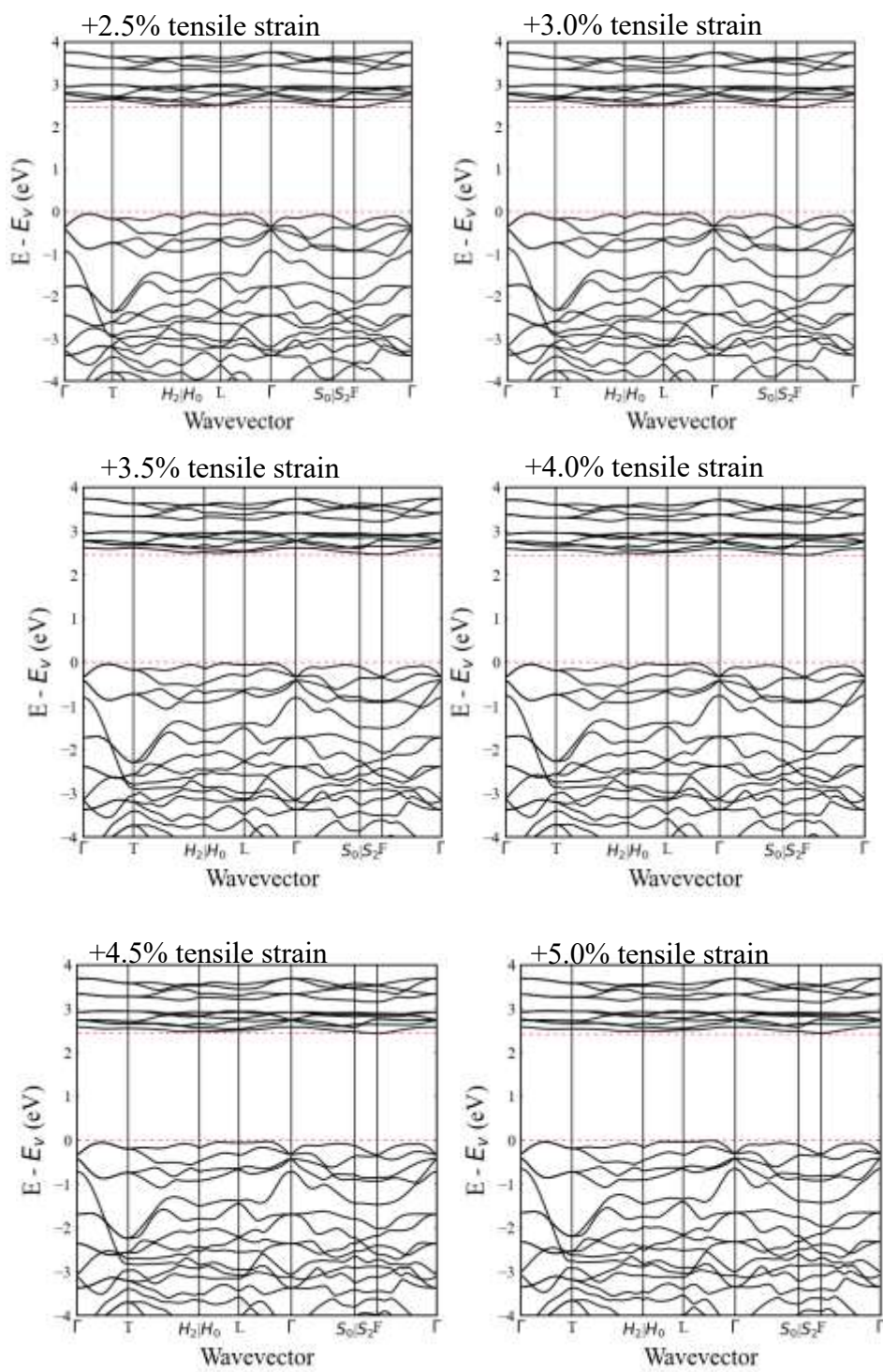




## 4. Band structures

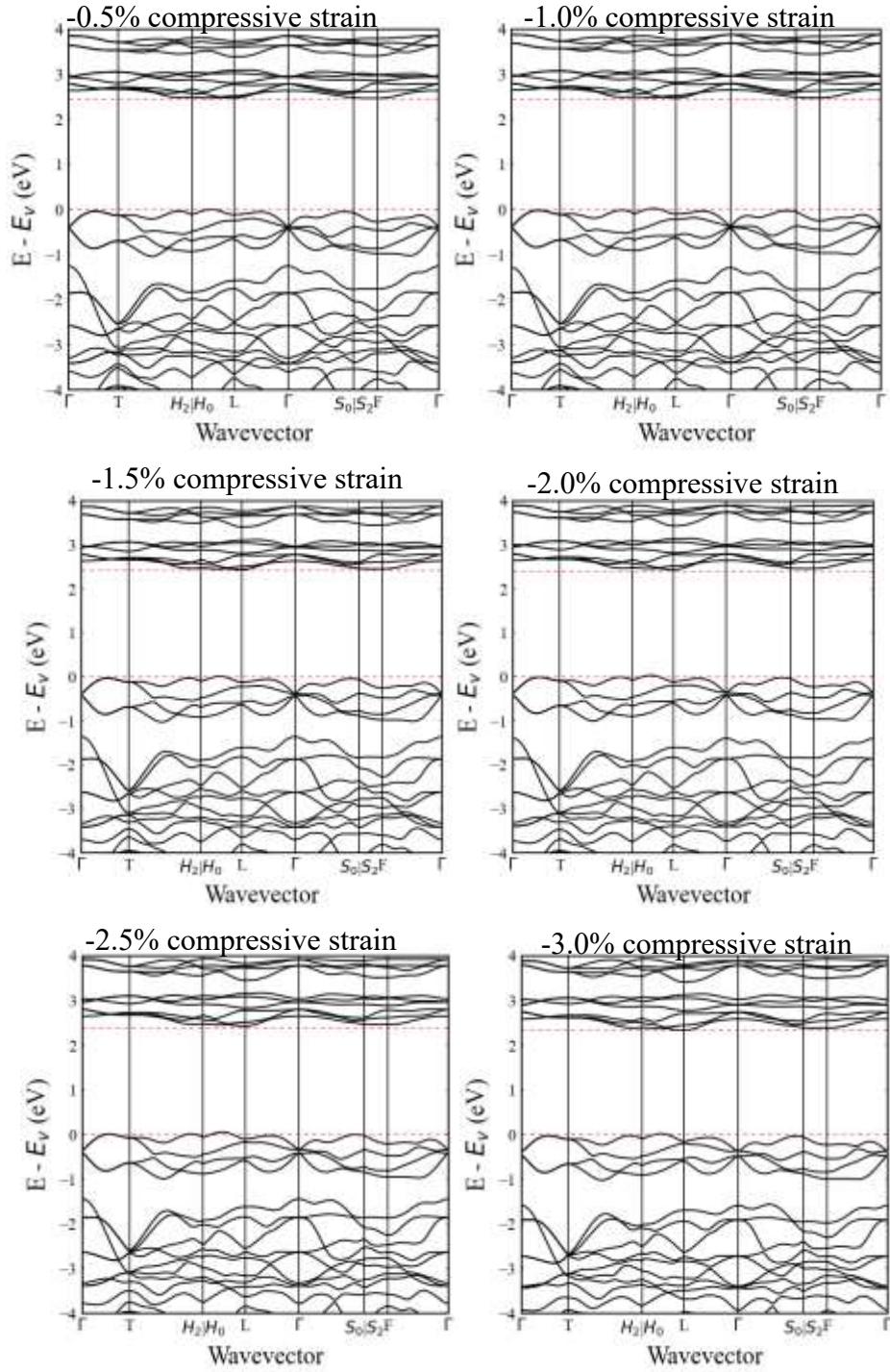
### A. Biaxial tensile strain

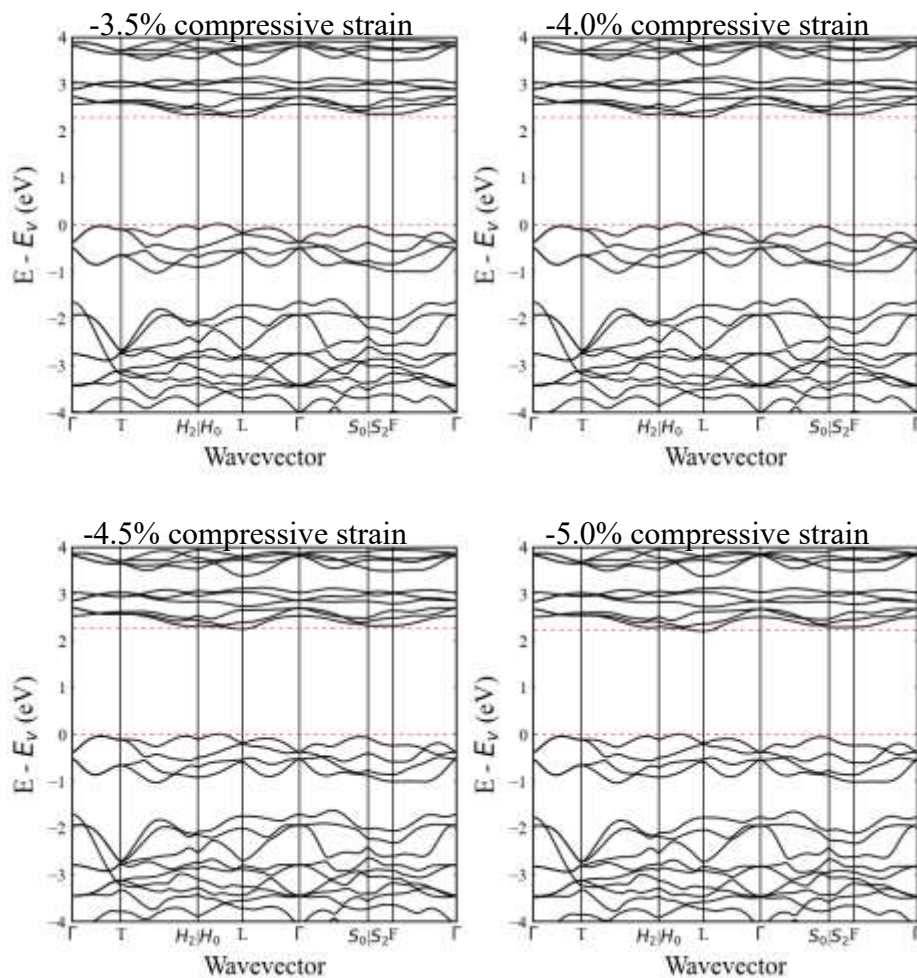






## B. Biaxial compressive strain

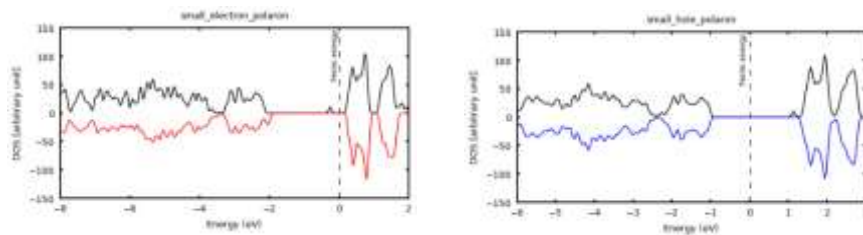




## 5. Total Density of states (TDOS)

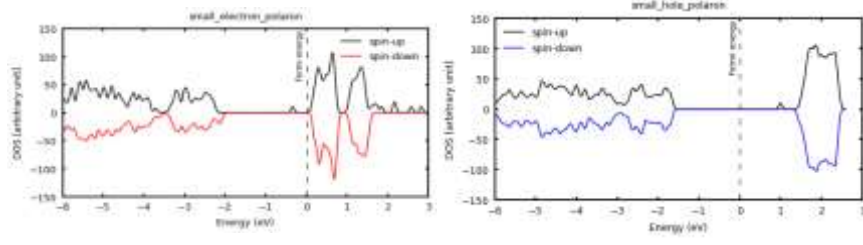
### A. Hubbard U values of $U(\text{Fe}) = 3.0$ eV and $U(\text{O}) = 7.0$ eV

0% strain

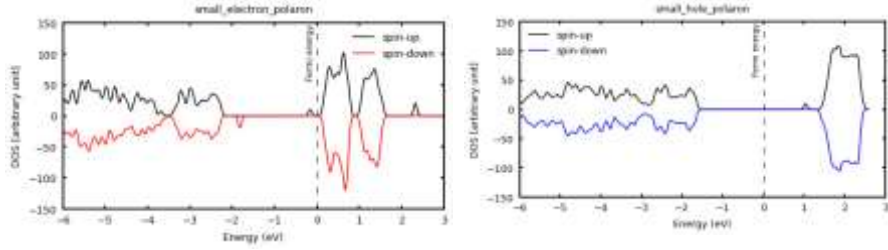


## I. Biaxial tensile strain

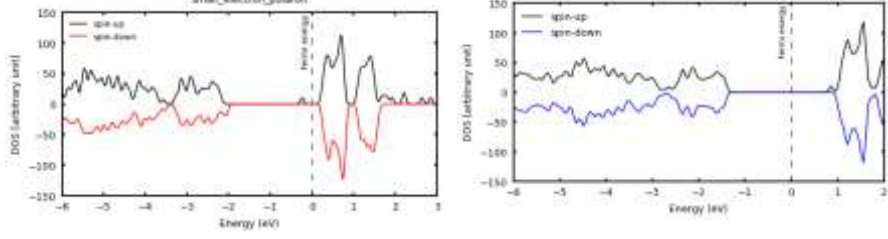
+0.5% tensile strain



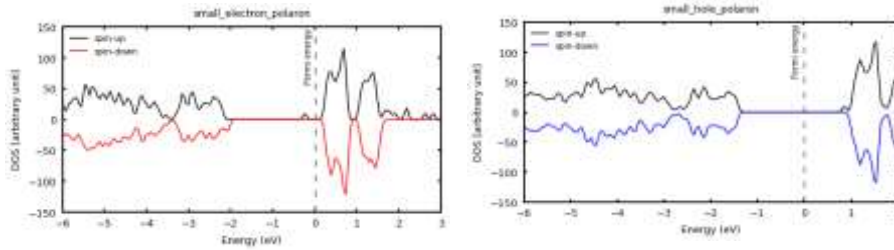
+1.0% tensile strain



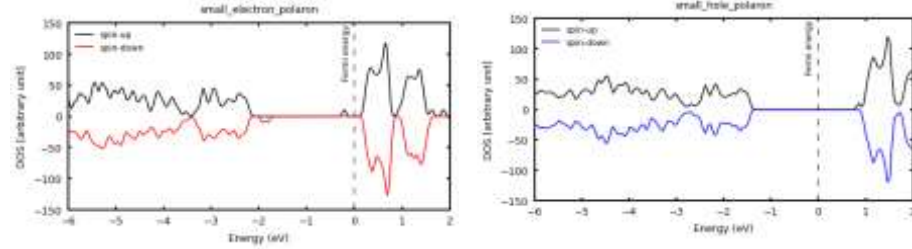
+1.5% tensile strain



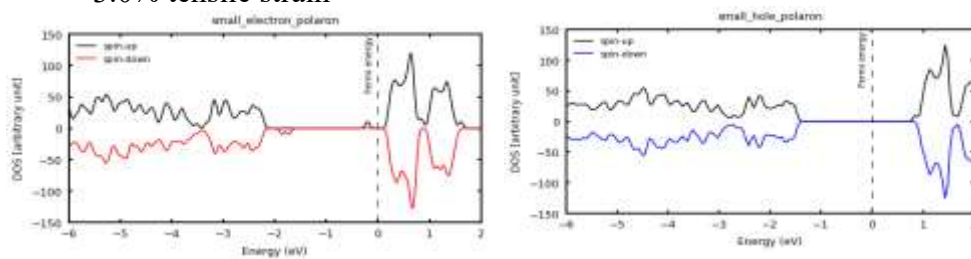
+2.0% tensile strain



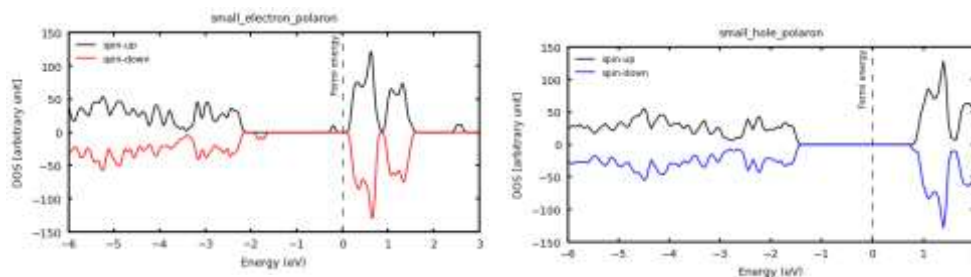
+2.5% tensile strain



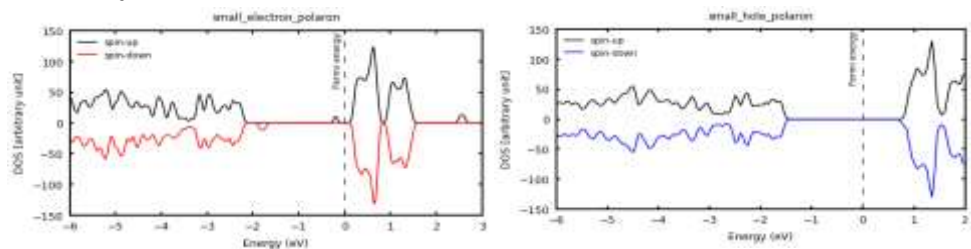
+3.0% tensile strain



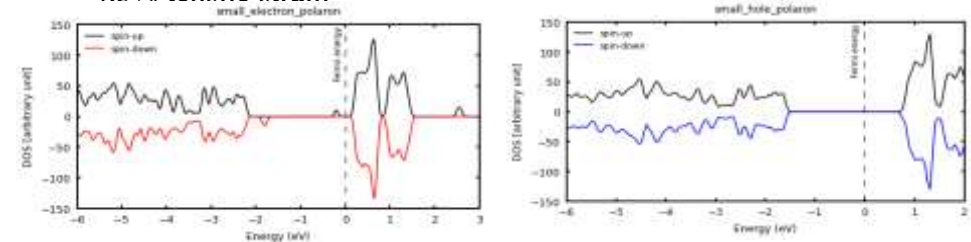
+3.5% tensile strain



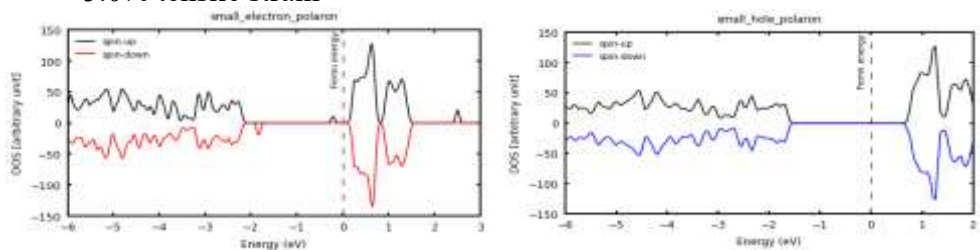
+4.0% tensile strain



+4.5% tensile strain



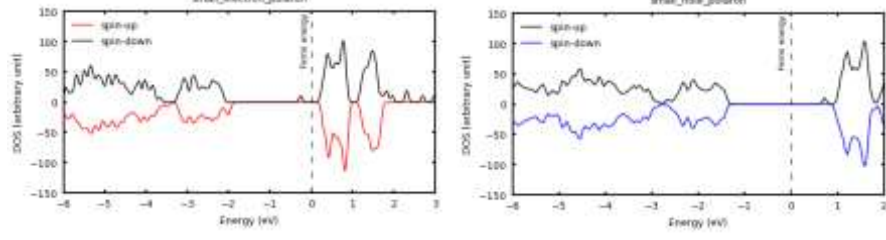
+5.0% tensile strain



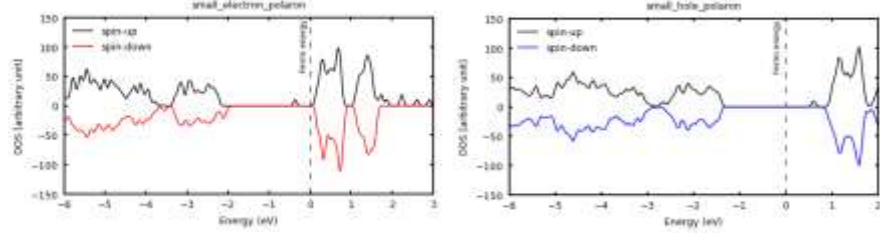


## II. Biaxial compressive strain

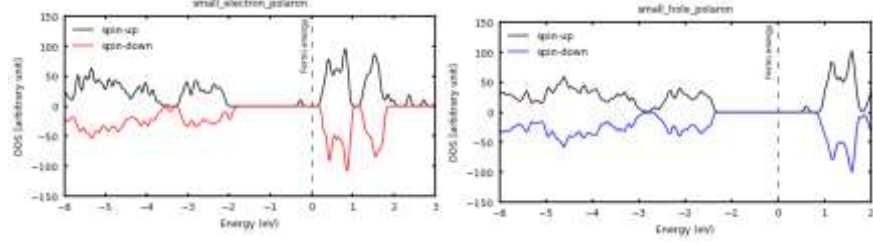
-0.5% compressive strain



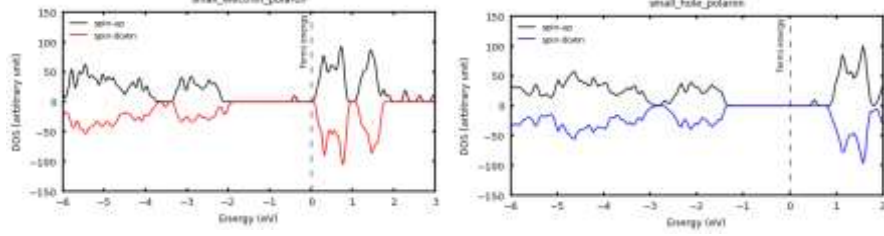
-1.0% compressive strain



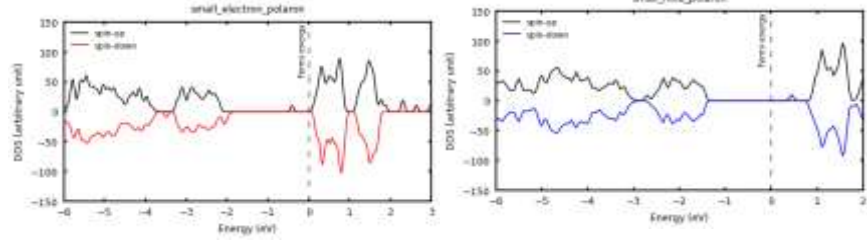
-1.5% compressive strain



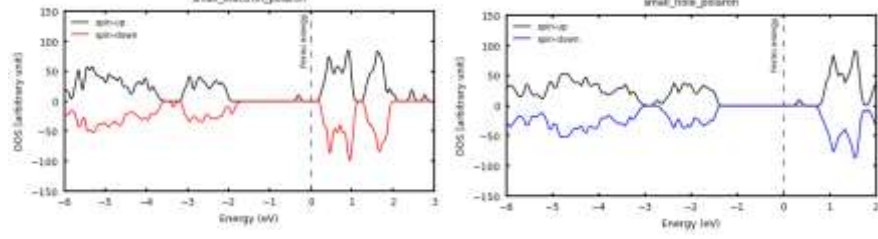
-2.0% compressive strain



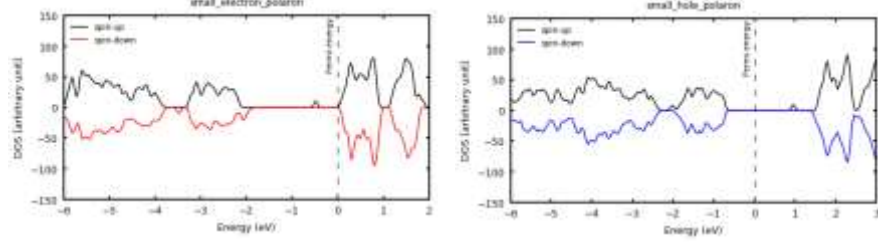
-2.5% compressive strain



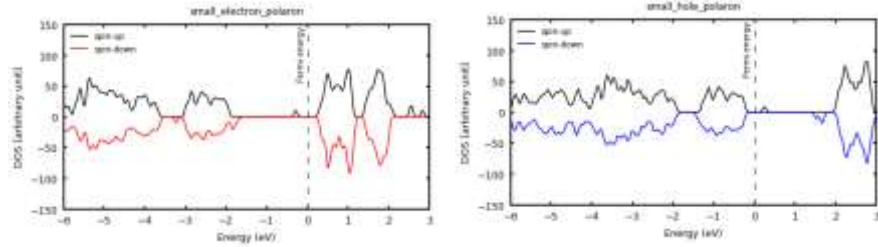
-3.0% compressive strain



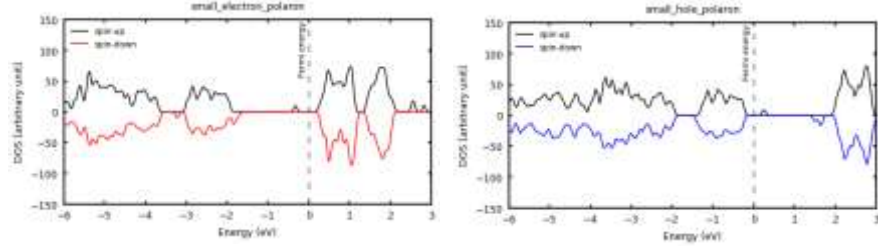
-3.5% compressive strain



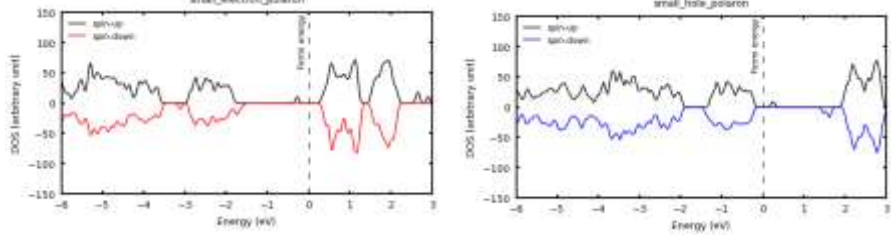
-4.0% compressive strain



-4.5% compressive strain

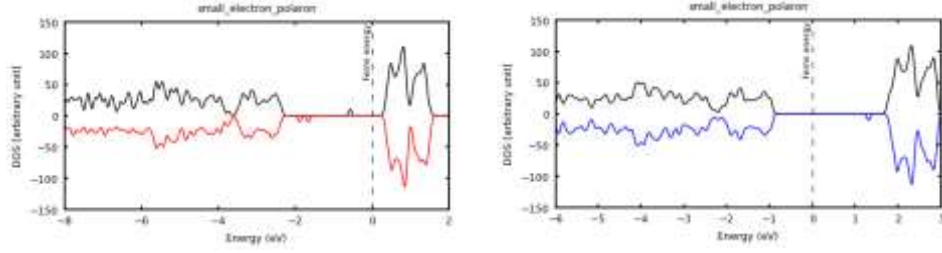


-5.0% compressive strain



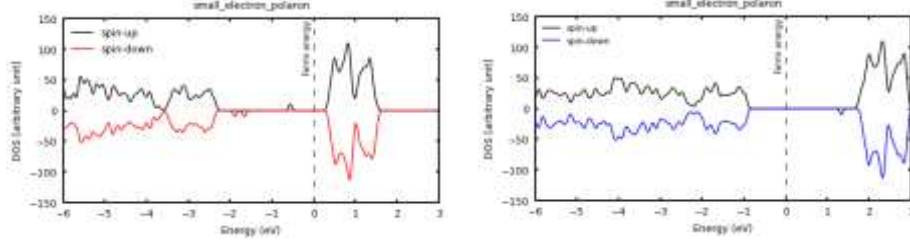
## B. Hubbard U values of $U(\text{Fe}) = 4.0 \text{ eV}$ and $U(\text{O}) = 6.5 \text{ eV}$

0% strain

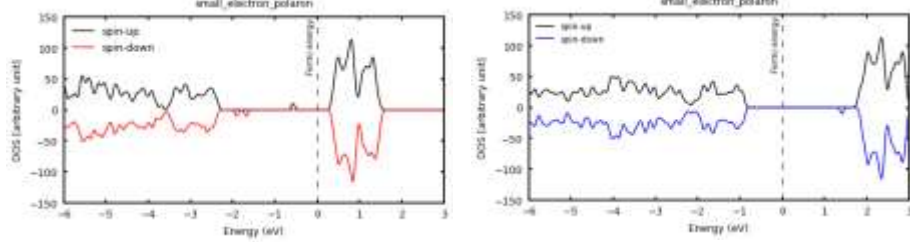


## I. Biaxial tensile strain

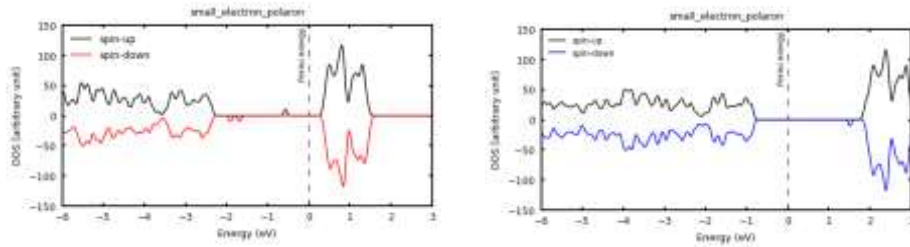
0.5% tensile strain



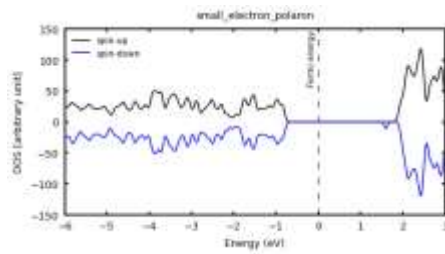
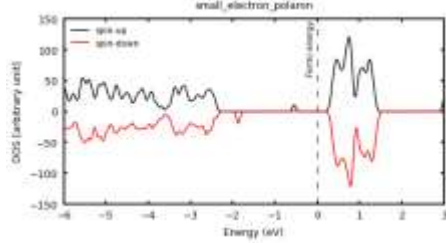
1.0% tensile strain



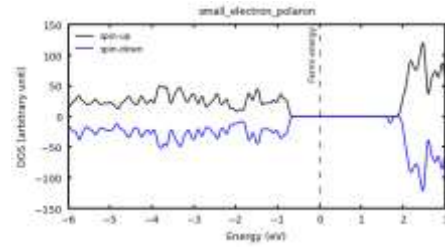
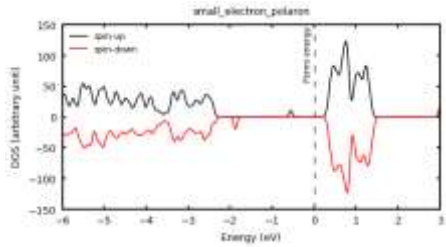
1.5% tensile strain



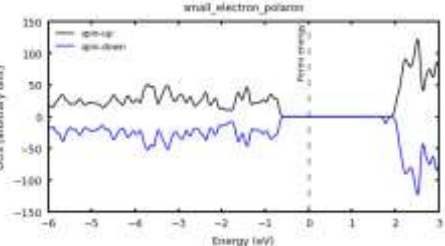
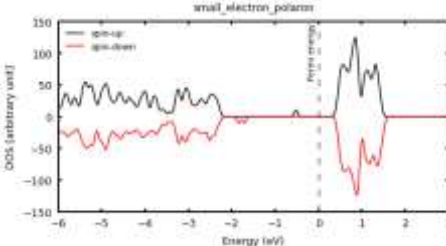
2.0% tensile strain



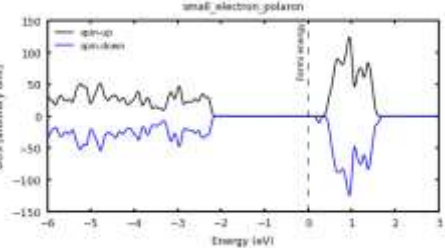
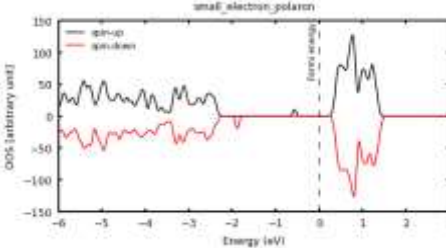
2.5% tensile strain



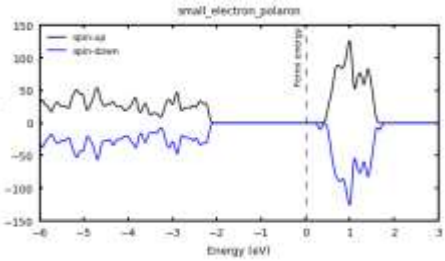
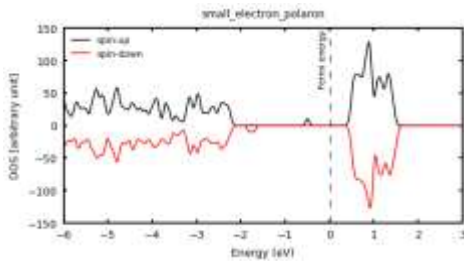
3.0% tensile strain



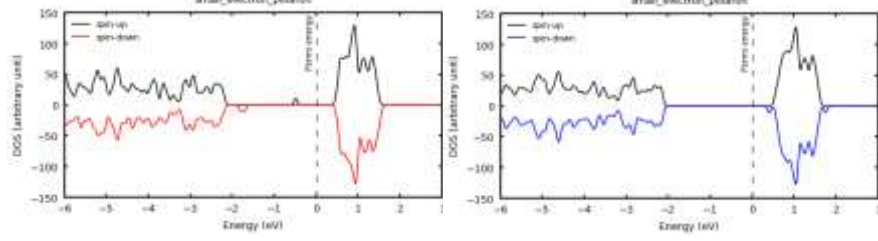
3.5% tensile strain



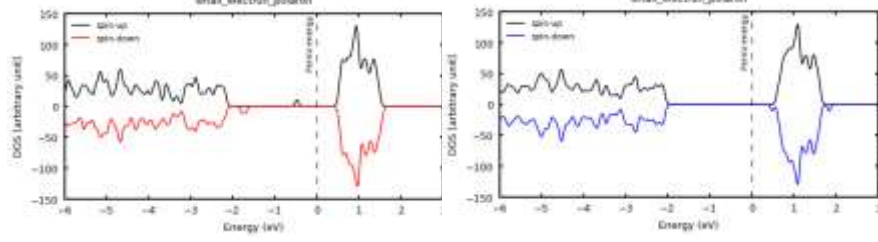
4.0% tensile strain



### 4.5% tensile strain

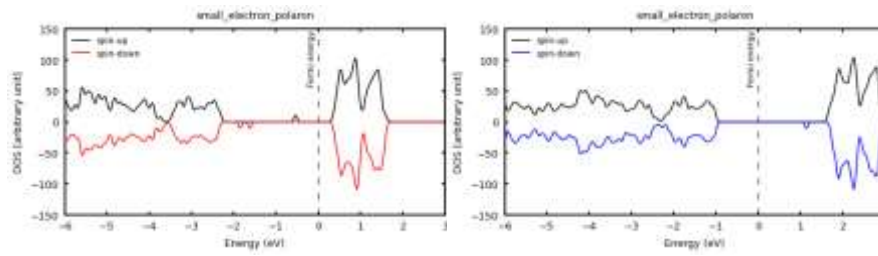


### 5.0% tensile strain

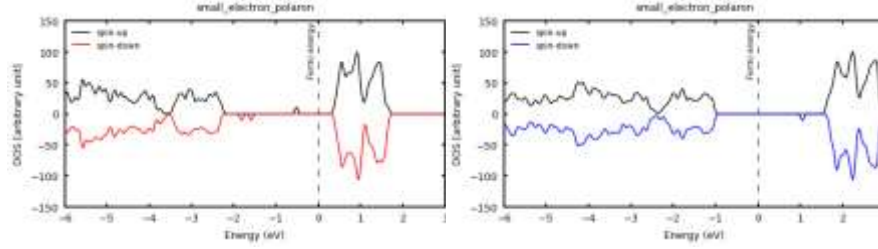


## II. Biaxial compressive strain

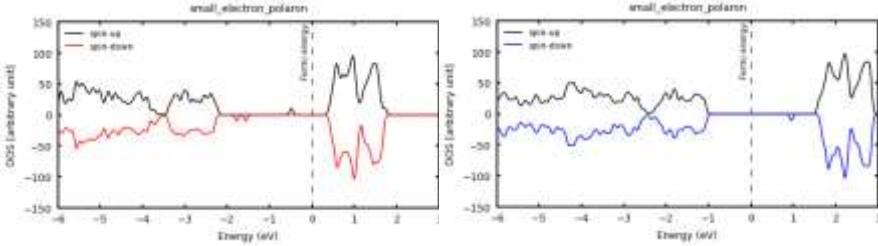
### 0.5% compressive strain



### 1.0% compressive strain

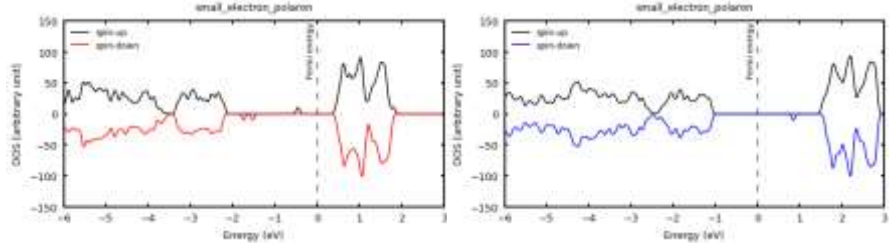


### 1.5% compressive strain

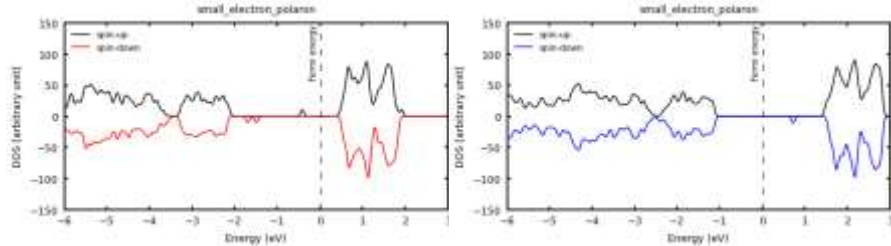




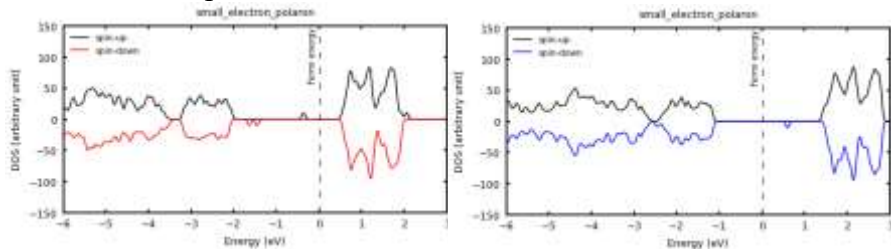
## 2.0% compressive strain



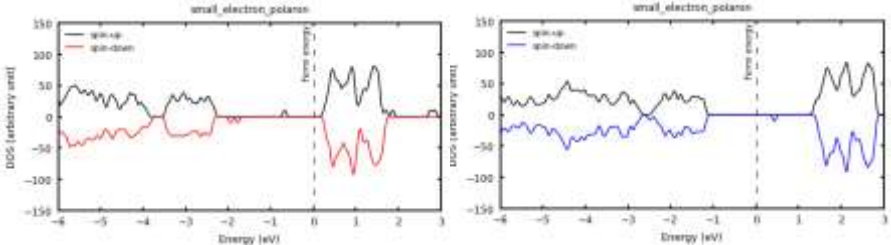
## 2.5% compressive strain



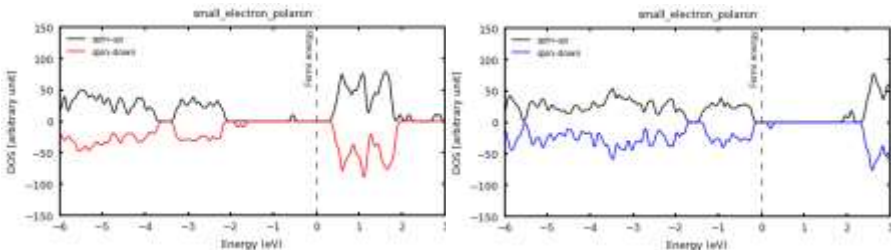
## 3.0% compressive strain



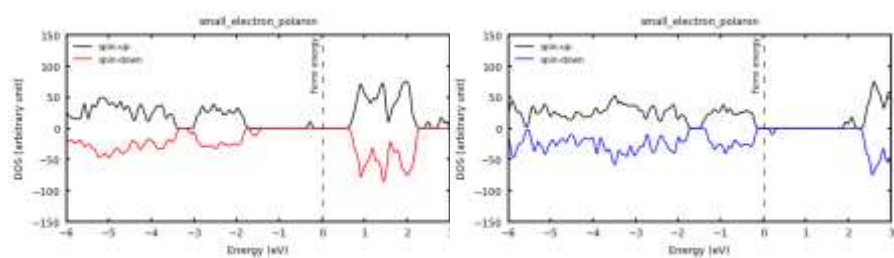
## 3.5% compressive strain



## 4.0% compressive strain



4.5% compressive strain



5.0% compressive strain

